Title

Trend analysis reveals distinct challenges in NOx emission controls and ozone pollution in California and a megacity in China

Author

Wang, Yurun

Publication Date

2023

Peer reviewed|Thesis/dissertation

Trend analysis reveals distinct challenges in NO_x emission controls and ozone pollution in California and a megacity in China

By

YURUN WANG

THESIS

Submitted in partial satisfaction of the requirements for the degree of

MASTER OF SCIENCE

in

Atmospheric Science

in the

OFFICE OF GRADUATE STUDIES

of the

UNIVERSITY OF CALIFORNIA

DAVIS

Approved:

Ian C. Faloona, Chair

Christopher D. Cappa

Michael Kleeman

Committee in Charge

2023

Table of Contents

Abstract

Nitrogen dioxide (NO_2) is a central air pollutant that is a precursor to the secondary pollutants ozone (O_3) and particulate matter (PM), which together inflict significant damage to human health, agricultural productivity, biodiversity and impact the Earth's climate. In California, a strict set of regulations targeting nitrogen oxide emissions, which go beyond national standards, have helped to achieve substantial air quality improvement in past five decades. However, these gains have been stalling suggesting the growing importance of less understood sources. In chapter 1, we present summertime (June–September) spatio-temporal patterns of NO_2 concentrations using satellite and ground observations across California during 2009–2020, quantifying the differences in NO_2 trends for 5 distinct land cover classes: urban, forests, croplands, scrublands (shrublands, savannas, and grasslands), and barren (minimally vegetated) lands. Over urban environments NO_2 columns exhibited continued but weakening downward trends ($–3.7 \pm 0.3\%a^{–1}$), which agree fairly well with contemporaneous trends estimated from the surface air quality network ($–4.5 \pm 0.5\%a^{–1}$). In rural (non-urban) parts of the state, however, secular trends are insignificant (0.0 to $0.4 \pm 0.4\%a^{–1}$) or in the case of remote forests are on the rise ($+4.2 \pm 1.2\%a^{–1}$). Sorting the NO_2 satellite data by air temperature and soil moisture reveals relationships that are commensurate with extant parameterizations but do indicate a stronger temperature dependence. We further find that rising temperature and decreasing precipitation in response to climate change is acting to increase soil NO_x emissions, explaining about one-third of the observed NO_2 rise in non-urban regions across California. These trends, or their absence, can be attributed predominantly to the alarming rise in wildfire frequency, especially since the turn of the 21st century.

Unlike more than 50-years extensive anthropogenic emission reductions in the US, many regions in the East Asia start to implement emission control strategies from the past decade, and the

evolution of O_3 pollution in these regions follow a distinct track due to its nonlinear responses to precursor emissions. In chapter 2, we identified O_3 variations and inferred trends in precursor emissions in a typical megacity (Chengdu) in southwestern China over 2013–2020 based on ambient measurements, emission inventory, and satellite data. Numerical models were used to investigate the changes in meteorological variability and biogenic emissions. Trends of O_3 in urban areas show deterioration (+14.0%a^{-1}) between 2013 and 2016 followed by a slight decrease over 2017–2020, while O_3 levels in rural areas generally show a downward trend (–2.9%a^{-1}) during 2014–2020. Both emission inventory (–3.7%a^{-1}) and OMI satellite columns (–4.5%a^{-1}) depict strong decline trends in NO_x emissions, while satellite HCHO columns exhibit a flattened downward trend of VOC emissions (–1.8%a^{-1}), which caused rural areas shifted from VOCs-limited to transitional or NO_x-limited regime since 2016. Considering metropolitan Chengdu remains VOCs-limited regime over time, the existing regulatory framework involving simultaneous NO_x and VOCs control would result in evident O_3 improvements in the near future. Despite benefits from anthropogenic emission reductions, we demonstrate that meteorological conditions and enhanced biogenic emissions over the warm season could partially or even fully offset effects attributed to emission changes, making the net effects obscure. This chapter informs effective O_3 mitigation policies for megacities in East Asia which undergo similar emission pathways in Chengdu.

Chapter 1: Satellite NO_2 trends reveal pervasive impacts of wildfire and soil emissions across California landscapes

1. Introduction

Nitrogen oxides (NO_x = NO + NO_2) serve as important precursors to tropospheric ozone (O_3) and fine particulate matter ($PM_{2.5}$) with consequent adverse effects including premature death (Caiazzo et al., 2013), cardiovascular mortality (Cohen et al., 2017), respiratory diseases (Meng et al., 2010), and agricultural productivity losses (Sampedro et al., 2020). The primary sources of NO_x involve the thermogenic release during high-temperature combustion in air from vehicles (Tan et al., 2019) and power plants (de Foy et al., 2015), lightning (Schumann and Huntrieser, 2007), biomass burning (Campbell et al., 2022), and also microbial emissions from soils (Oikawa et al., 2015). A recent modeling study by Silvern et al. (2019) for the continental US (CONUS) estimates the proportion of total emissions from anthropogenic fossil fuel combustion to be only 42% in 2017 and falling. Nitrogen dioxide (NO_2) is a reactive gas with a daytime lifetime of a few hours with respect to its reaction with the hydroxyl radical (OH) (Laughner and Cohen, 2019), and can be observed from space due to its unique absorption spectrum (Vandaele et al., 1998). A number of satellites have been deployed to monitor the tropospheric NO_2 vertical column densities (NO_2 VCD) with several semi-overlapping missions dating back to the 1990s (Burrows et al., 1999; Bovensmann et al., 1999; Callies et al., 2000; Levelt et al., 2006; Veefkind et al., 2012). In particular, The Ozone Monitoring Instrument (OMI) (Levelt et al., 2006, 2018) aboard the National Aeronautics and Space Administration (NASA) Aura satellite provides a daily global record of NO_2 columns since 2004, which has been used extensively to infer the trends and sources of NO_x emissions from regional to global scales (Vinken et al., 2014; Silvern et al., 2019).

Since the 1970s, the U.S. Environmental Protection Agency (EPA) has prioritized policies and technologies to reduce NO_x emissions from the combustion of fossil fuels, resulting in an array of benefits for the nation's air quality (US EPA, 2016). In California, a number of techniques, including OMI satellite retrievals, have been used to examine the efficacy of statewide NO_x emission controls, although non-uniformly across the state (Russell et al., 2010). The California Air Resources Board (CARB) reported a ~42% reduction in anthropogenic NO_x emissions over the period of 2009 to 2019 ($–4.2\%a^{–1}$) and proposed focusing most on diesel regulations to further accelerate NO_x reductions in order to comply with federal air quality standards in the future. Based on ambient measurements and OMI satellite, Lamsal et al. (2015) estimated comparable reductions from 2005 to 2013 in Southern California ($–5.2\%a^{–1}$) and the Central Valley ($–4.4\%a^{–1}$). Similarly, Russell et al. (2012) estimated reductions of NO_2 ranging from –4.6 to $–5.7\%a^{–1}$ in California urban regions in the period from 2005–2011. These and other satellite studies across the US (Lu et al., 2015; Jiang et al., 2018; Silvern et al., 2019; Qu et al., 2021; Wang et al., 2021) have found a marked discontinuity in linear diminution rates some time around 2009, reporting summertime trends in remote regions that flatten ($\sim 0\ \%a^{–1}$) (Silvern et al., 2019) or even rise ($+2.0\ \%a^{–1}$) (Russell et al., 2012). Most have proposed reasons for these recent trends to be related to the growing relative importance of "natural" or uncontrolled NO_x sources like soil, lightning, and possibly wildfires. While many have assumed the abrupt change had to do with the economic downturn around 2009, Wang et al. (2021) use multivariate trend analysis to argue that just by meteorological chance the trends in the combined emissions from soils and lightning changed from $–4\ \%a^{–1}$ to $+0.6\ \%a^{–1}$ after 2009.

Despite long-term progress non-attainment of national air quality standards persists throughout California's Central Valley and other inland areas (Parrish et al., 2017; Buysse et al.,

2018). de Foy et al. (2020) reported that O_3 concentrations in the San Joaquin Valley (SJV) exceeded the National Ambient Air Quality Standards (NAAQS) for ground-level O_3 (70 ppb) on 71 days in 2017 and 43 days in 2018. Similarly, Burley et al. (2016) found that the Sierra Nevada Mountains also routinely experience O_3 exceedances during the summer months. As substantial reductions in anthropogenic NO_x emissions have been achieved, recent work has demonstrated that the O_3 formation regime has shifted to NO_x-limited in these non-attainment inland areas since the 2010s (de Foy et al., 2020), and the O_3 formation becomes more sensitive to the perturbations of free tropospheric NO_x background attributed to biogenic emissions (Silvern et al., 2019; Geddes et al., 2022). For example, Sha et al. (2021) estimated that soil emissions account for ~40% of California's total NO_x emissions (for the month of July 2018), which significantly increase the surface NO_2 and O_3 (+23%) concentrations in rural California. This finding is in accordance with other work that has identified soil NO_x emissions as an important component of the overall budget (Oikawa et al., 2015; Almaraz et al., 2018; Y. Wang et al., 2021). Moreover, Pan and Faloona (2022) reported that O_3 levels are enhanced, on average, by 10% in California's Central Valley during wildfire-influenced periods, which were identified 1 in 5 days during June-September from 2016–2020. Although lightning is much less of an influence in California than in most of the rest of the US (Schumann and Huntrieser, 2007), existing studies have clearly identified the distinct role of both persistent and fugitive NO_x emissions over croplands and associated with wildfire smoke in the degradation of air quality in California's inland rural communities (Ninneman and Jaffe, 2021; Parrish et al., 2017, 2022). However, historical trend analyses of soil- and wildfire-sourced NO_x emissions in California have been largely neglected, especially in the last decade when the surface temperature and biomass burning have risen so dramatically (Williams et al., 2019; Li and Banerjee, 2021).

Here we use satellite NO_2 columns from the Ozone Monitoring Instrument (OMI) and the surface monitoring network to examine the temporal trends of NO_2 across California during the summer months (June–September) from 2009 to 2020. To investigate different sources to the NO_2 trends, we explore how they vary across 5 different land cover types. For the non-urban regions where the soil and wildfire emissions could be dominant NO_x sources, multiple gridded climate data sets along with a monthly burned area data set are used to explore the influence of meteorological conditions and wildfires on the NO_2 levels and make crude estimates of their growing importance by mid-century. Our study highlights the remarkable rise in wildfire and soil NO_x emissions in inland California over the past decade and may provide guidance for understanding future air quality in California.

2. Materials and Methods

2.1. California Land Cover Classification

We use the Terra and Aqua combined Moderate Resolution Imaging Spectroradiometer (MODIS) Land Cover Type (MCD12Q1) Version 6 data product with a spatial resolution of 500m to classify the land cover types across California (Friedl et al., 2019). In our trend analysis, we merged the MODIS land covers into 5 distinct types: urban, forests, croplands, scrublands, and barren based on the land cover distributions (Fig. A1a). The subordinate types have the same NO_2 levels (difference < 0.16×10^{15} molec/cm^2), comparable annual NO_2 trends (difference < 1.8%a^{-1}), and similar responses to the temperature and soil moisture (Fig. A1b-d, Table A1). The distribution of simplified land covers is shown in Fig. 1.1a. Overall, California's land cover is primarily made up of scrublands (48.4%), forests (22.8%), and barren lands (15.3%). Agriculture is also an important land use in California, with the Central Valley being one of the most productive

agricultural regions in the world, where nitrogen-rich fertilizers are applied to the vast cropland areas (9.5%) (Almaraz et al., 2018). Urban areas account for a relatively small part (4.0%), mainly located in the state's coastal regions.

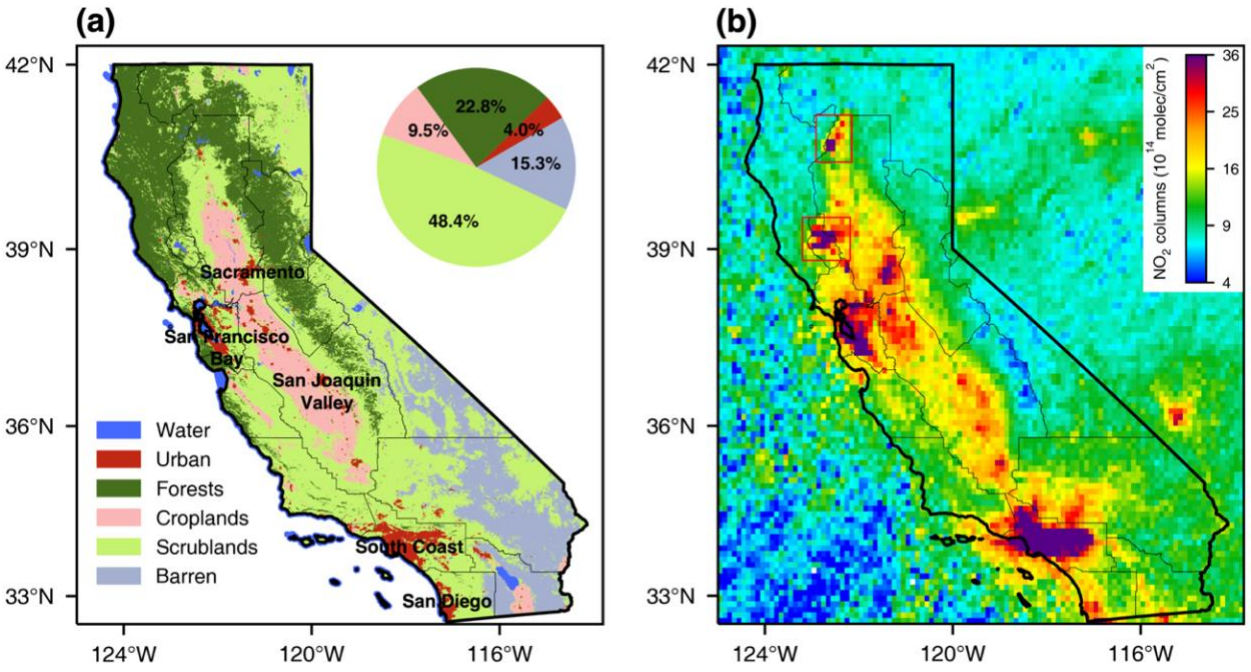

Figure 1.1. ***(a)*** *Map of the MODIS land cover types across California.* ***(b)*** *June–September average TROPOMI NO_2 columns over California in 2018. The wildfire NO_2 hotspots are outlined in red rectangles.*

2.2. NO_2 Column Retrievals

The Ozone Monitoring Instrument (OMI) measures backscattered solar radiation from the earth in the ultraviolet and visible wavelength range from 270 to 500 nm (Levelt et al., 2006). It provides daily global measurements of various trace gases, including NO_2 with a 2600 km wide swath and a spatial resolution of 13×24 km^2 for nadir pixels. We use three versions of OMI NO_2 column retrievals: the NASA NO_2 column retrieval (Krotkov et al., 2012), the Berkeley High-Resolution (BEHR) retrieval (Russell et al., 2011), and the Quality Assurance for Essential Climate Variables (QA4ECV) retrieval (Boersma et al., 2017, 2018). The area-weighted average algorithm described by Jin et al. (2020) is used to grid the daily Level-2 swaths to the monthly

mean NO_2 columns over California with a spatial resolution of 0.1°×0.1°. To ensure the quality and stability of the satellite data, we select observations with cloud fraction <0.3, solar zenith angle <80°, surface albedo <0.3, and no "row anomaly (RA)" data (Schenkeveld et al., 2017). The pixels at the swath edge (first and last five rows) are also removed for QA4ECV and NASA retrievals.

The TROPOspheric Monitoring Instrument (TROPOMI) was launched by the European Space Agency (ESA) for the European Union's Copernicus Sentinel-5 Precursor (S5p) satellite mission in October 2017 (Veefkind et al., 2012). TROPOMI samples daily at 13:30 local overpass time with an unprecedented horizontal resolution as fine as 3.5×5.5 km in nadir (3.5×7 km before August 2019). In order to compare with the OMI NO_2 columns, the daily TROPOMI Level-2 NO_2 columns during 2018–2020 are sampled to 0.1°×0.1° with cloud fraction <0.3, solar zenith angle <80°, surface albedo <0.3, and the quality assurance value (qa) >0.75.

2.3. Surface NO_2 Measurements

The surface NO_2 measurements during summer (June–September) from 2009 to 2020 are collected from the California Air Resource Board (CARB). The hourly data are averaged over the afternoon hours (12:00–16:00) to temporally match with the OMI measurements. There are 68 CARB NO_2 sites with continuous records between 2009 and 2020 that are selected to compare with the satellite data over 4 urban areas (South Coast, San Francisco Bay, San Diego County, and Sacramento County) and other regions by sampling the OMI NO_2 columns at the grid cells of the NO_2 monitoring network. The distribution of measurement sites is shown in Fig. 1.2a.

2.4. Meteorological Datasets

To explore the effects of meteorology on the trends of NO_2 levels, the potential variables considered in this study include temperature, soil moisture, precipitation, planetary boundary layer

height, horizontal wind speed, downward shortwave radiation, and cloud cover are derived from the fifth-generation European Centre for Medium-Range Weather Forecasts (ECMWF) reanalysis (ERA5, ERA5-Land) (Hersbach et al., 2020; Muñoz-Sabater et al., 2021), Parameter-elevation Relationships on Independent Slopes Model (PRISM) climate group (Daly et al., 2008), and the NCEP North American Regional Reanalysis (NARR) (Mesinger et al., 2004). The meteorological datasets used in this study are summarized in Table A2.

2.5. Wildfire Records

The California statewide database of fire history is obtained from the Fire and Resource Assessment Program (FRAP), which compiles fire perimeters from CAL FIRE, the United States Forest Service Region 5, the Bureau of Land Management, and the National Park Service. This data includes the California fire events that occurred since 1950 along with fire alarm dates, containment dates, area burned and the causes of ignition. This work focused on the wildfire events that happened during the summer months (June–September) from 2009 to 2020, covering a total burned area of ~7.8 million acres across 3,117 separate fires.

2.6. Temperature/Soil Moisture Dependence

For these non-urban regions where the soils have been identified as a major source of NO_x emissions (Oikawa et al., 2015), the parameterization of soil NO_x emissions (BDSNP) (Hudman et al., 2012), which is commonly used in chemistry transport models (CTMs), is adopted to capture the relationship between meteorological variables and NO_2 columns. In the BDSNP scheme, soil NO_x emissions increase exponentially with temperature in the temperature-sensitive regime (0–30 °C) and remain constant when the temperature is above 30 °C (Steinkamp and Lawrence, 2011;

Hudman et al., 2012). Similarly, an exponential function is fitted to the relationship between NO_2 columns and temperature in this study:

$$[NO_2](T) = \begin{cases} a \cdot exp(b \cdot T) + c & T < T_0 \\ a \cdot exp(b \cdot T_0) + c & T \geq T_0 \end{cases} \quad (1)$$

Where [NO_2] represents the NO_2 columns, T is the temperature (in degrees Celsius), T_0 is the upper limit of the temperature-sensitive regime, and the constant *b* is obtained by fitting the data over all non-urban regions (the sum of forests, croplands, scrublands, and barren) (Fig. A3). This *b* value is then applied to the fittings over all subordinate land types in California.

The non-linear relationship between soil NO_x emissions and soil moisture is typically described by a Poisson function, with the lowest emissions at both extremely dry and wet conditions (van Dijk, 2002; Hudman et al., 2012). The equation of a Poisson distribution to fit the relationship between NO_2 columns and soil moisture is shown in Eq. (2). Where [NO_2] represents the NO_2 columns, θ is the volumetric soil moisture.

$$[NO_2](\theta) = a \cdot \theta \cdot exp(-b \cdot \theta^2) + c \quad (2)$$

3. Results and Discussion

3.1. Spatially Heterogeneous NO_2 Trends

Fig. 1.2-1.3, Tables 1.1 and Table A1 show the trends of summertime NO_2 concentrations during 2009–2020 in California from the Quality Assurance for Essential Climate Variables (QA4ECV) OMI retrievals (Boersma et al., 2017) and ground measurements. We present here the summertime (June through September) trends, because they are most relevant to persistant O_3 issues and were found to be the greatest, and begin our analysis in 2009 to avoid the discontinuity in trends found before that time. Comparisons with trends detected using the NASA standard

product, Berkeley High-Resolution (BEHR) (Russell et al., 2011), and Tropospheric Monitoring Instrument (TROPOMI) (van Geffen et al., 2019) retrievals (Fig. A2) show excellent agreement. Continued, significant NO_2 reductions are observed in California's urban areas from 2009-2020 at a rate of $–3.7 \pm 0.3\%a^{–1}$, which is slightly smaller than the range ($–3.9$ to $–5.7\%a^{–1}$) of diminution reported in previous studies (Table 1.1), but this difference is likely attributable to slower rates of change in the years subsequent to 2009 (Jiang et al., 2018). We further compared the NO_2 vertical column density trends to those derived from the CARB surface air quality network. The afternoon (12:00–16:00) surface NO_2 concentrations are closely correlated ($R^2 = 0.70$, $N = 816$) with the NO_2 columns across the state (Fig 1.2a). At the air basin scale, both the satellite ($–4.5 \pm 0.5\%a^{–1}$) and ground measurements ($–4.6 \pm 0.4\%a^{–1}$) demonstrate a coherent decline in NO_2 ($p < 0.05$) over the South Coast (Fig. 1.3). Shallower rates of NO_2 declines were found by satellite in the San Francisco Bay ($–2.7 \pm 0.4\%a^{–1}$), San Diego County ($–2.5 \pm 0.4\%a^{–1}$), and Sacramento County ($–2.1 \pm 0.5\%a^{–1}$), although the surface measurements in these urban regions decreased at rates similar to the South Coast ($–4.4$ to $–4.9\%a^{–1}$). There are two alternatives for this discrepancy: (i) the OMI instrument with its relatively coarse resolution ($13×24$ km^2) tends to horizontally dilute the small-scale anthropogenic signal detected by local sensor measurements (Cooper et al., 2020) with more slowly diminishing surrounding air, or (ii) the satellite measurements are more influenced by a non-decreasing tropospheric background NO_2. Either of these could potentially be less apparent in the sprawling, higher-NO_x environment of the Los Angeles (South Coast) air basin.

By contrast, atmospheric NO_2 concentrations outside of California's urban centers show either non-significant (unchanging) or positive trends from 2009 to 2020 (Fig. 1.2). In particular forested areas, which have been much more frequently affected by wildfires over the past two decades (Li and Banerjee, 2021), exhibit a strong increasing NO_2 trend ($+4.2 \pm 1.2\%a^{–1}$). Much more muted

trends are seen in scrublands (+0.4 ± 0.4%a^{-1}), and statistically non-significant changes are found in barren (+0.2 ± 0.4%a^{-1}) and cropland regions (0.0 ± 0.4%a^{-1}).

Table 1.1. *Comparison of NO_2 trends (%a^{-1}) in California urban areas with previous studies.*

Years	Regions	NO_2 trends	Method	Sources
2005–2011	Statewide	–4.6 ~ –5.7	Satellite	Russell et al. (2012)
2005–2012	Los Angeles	–5.7	Satellite	Tong et al. (2015)
2005–2013	South CA.	–5.2	Satellite	Lamsal et al. (2015)
2005–2015	Statewide	–3.9 ~ –4.1	Field measurement	Jiang et al. (2018)
2009–2019	Statewide	–4.2	Emission inventory	CARB
2009–2020	Statewide	–3.7	Satellite	This study

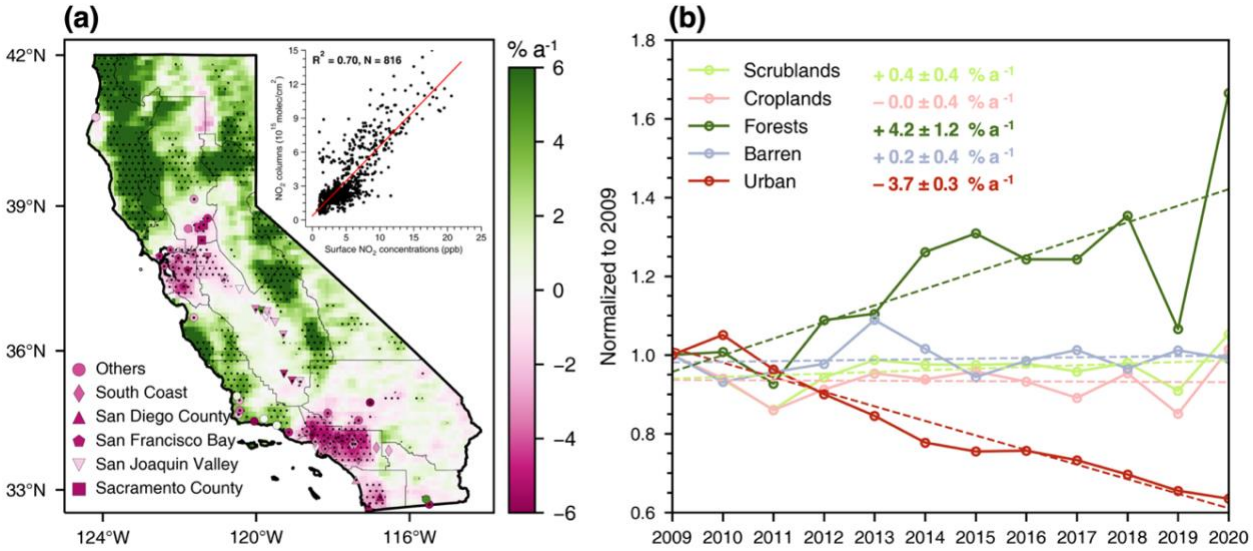

Figure 1.2. *Trends in June–September average NO_2 levels over California during 2009–2020.* ***(a)*** *Spatial distributions of the trends from QA4ECV OMI NO_2 columns and CARB ambient monitoring network with continuous annual records for 2009–2020. Statistically significant trends with p-values < 0.05 are marked with black dots. The insert shows the surface NO_2 concentrations compared to the NO_2 columns. R^2 represents the coefficient of determination and N is the number of data points in the scatter plot.* ***(b)*** *The NO_2 column trends are separated into urban, forests, croplands, scrublands, and barren lands defined by the land covers in Fig. 1.1a. Ordinate values are ratios relative to 2009. The mean ± standard deviation annual percent change is shown in inset.*

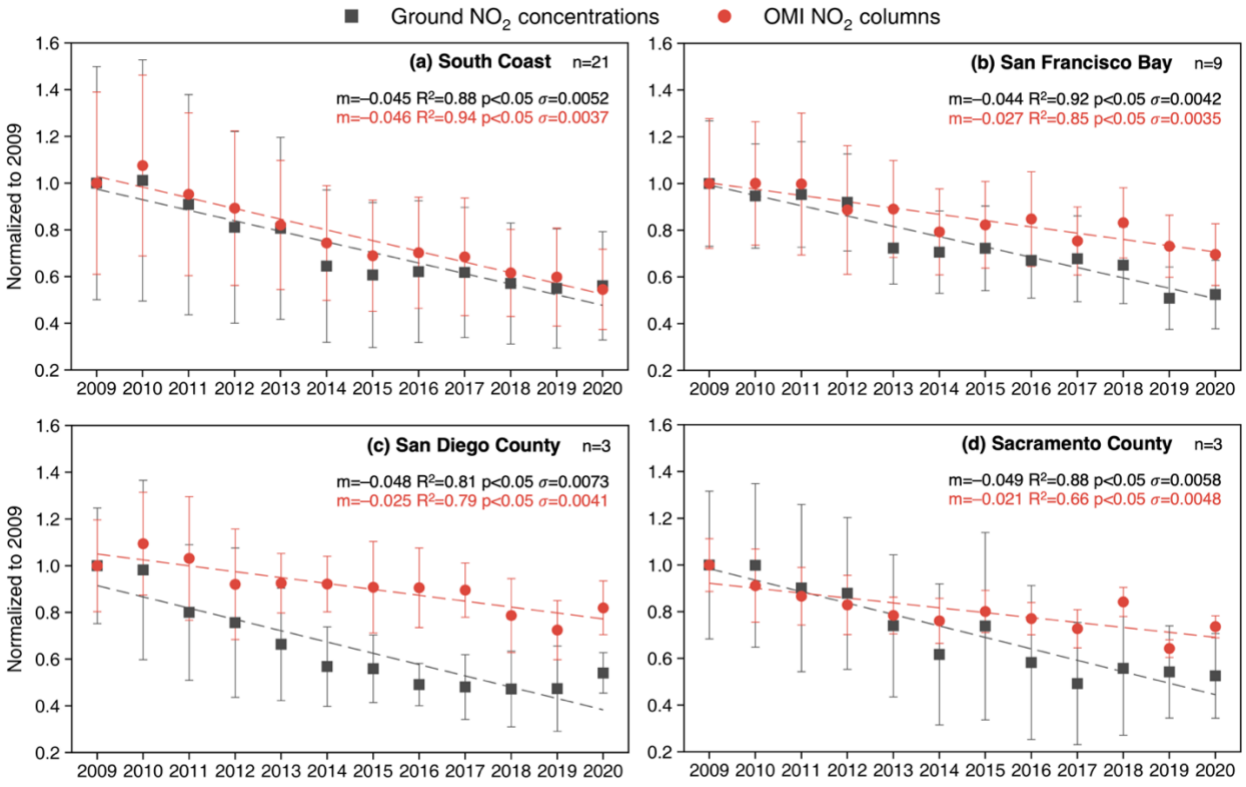

Figure 1.3. *June–September average NO_2 levels in urban areas during 2009–2020 from QA4ECV OMI NO_2 columns and ambient monitoring network. The trends are normalized to a value of 1 in 2009. n represents the number of sites, m is the slope of the linear regression, R^2 is the coefficient of determination, σ is the standard error. The p less than 0.05 represent the trends are statistically significant. The locations of the monitoring sites are presented in Fig. 1.2a.*

3.2. Anthropogenic Effects

Given the shorter NO_x lifetime during summer (Beirle et al., 2011), we infer that regulations targeting fossil fuel combustion within and near urban areas would have a more limited impact on NO_2 levels in more remote regions during the summer months. To examine this hypothesis, we compare the NO_2 weekly cycle between different land types (Fig. 1.4). This analysis reveals that NO_2 on weekends (Sundays) is on average 42% (-1.8×10^{15} molec/cm^2) lower than on weekdays (Tuesdays–Fridays) in urban areas because of the well-documented pattern of human activities (de Foy et al., 2020; Goldberg et al., 2021), consistent with the hypothesis. Non-urban areas do not

present significant declines, with only small, detectable decreases found in croplands (-0.3×10^{15} molec/cm^2) and scrublands (-0.2×10^{15} molec/cm^2). It is important to note that the observed NO_2 cycles are not influenced by the wildfires and soil emissions because the weekend-weekday variations in burned area and temperature are less than 0.2% (Table A3). Since the weekend-weekday effects on the NO_2 trends are minimal in the forests and barren lands, which tend to be the farthest from urban centers (Fig. 1.1), we assume that fossil fuel sources affect these two land types negligibly.

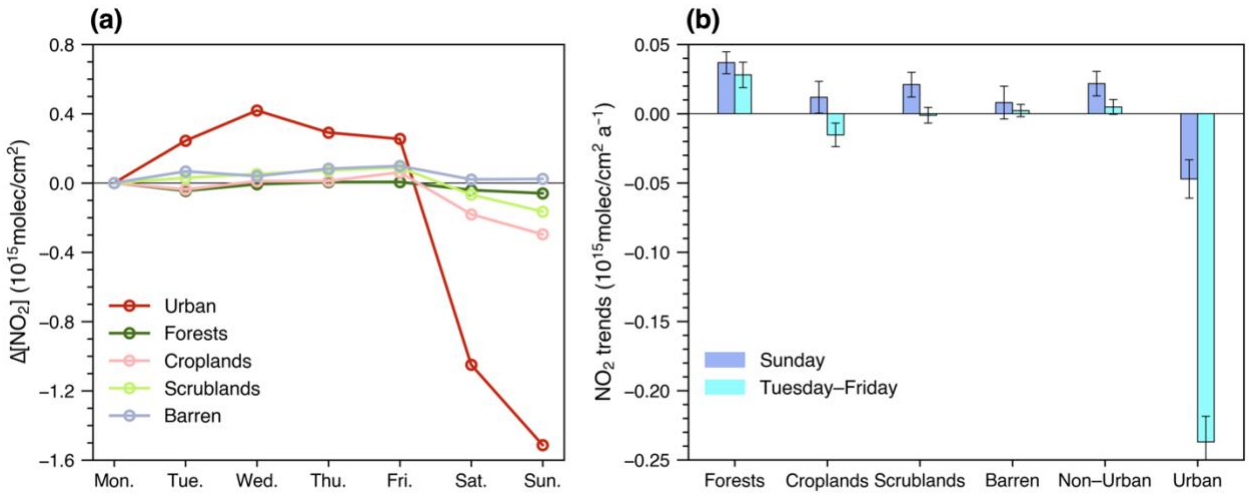

Figure 1.4. ***(a)*** *The weekly cycle of QA4ECV OMI NO_2 columns across urban, forests, croplands, scrublands, and barren areas of California.* ***(b)*** *Trends of Sunday and Tuesday–Friday average QA4ECV OMI NO_2 columns across forests, croplands, scrublands, barren, non-urban, and urban areas of California. The error bars are the standard deviation of the trends.*

3.3. Soil Emissions Effects

Soil emissions, modulated by soil microbes, weather conditions, and reactive nitrogen (N) amounts, have been identified as a significant source of NO_x in California, particularly in warm agricultural regions (croplands) with high fertilizer applications (Almaraz et al., 2018; Byrnes et al., 2020; Oikawa et al., 2015). Fig. 1.5a shows temporal correlations between NO_2 columns and a set of potential drivers over non-urban areas in California. The temperature (r = 0.81) and soil

moisture (r = –0.70), which are two major factors driving soil emissions, are highly correlated with the NO_2 columns, though the correlations vary regionally (Fig. 1.5f-g). For example, Northern California, dominated by forests and scrublands, has the strongest positive correlations with temperature (r > 0.8) and is inversely correlated with soil moisture (r < –0.6), while opposite relationships are found in the southeastern barren areas. This deviation highlights the variability of NO_2 dependencies upon soil conditions, and a finer-scale analysis is critical for accurately quantifying the impacts of soil emission on long-term NO_2 trends in California.

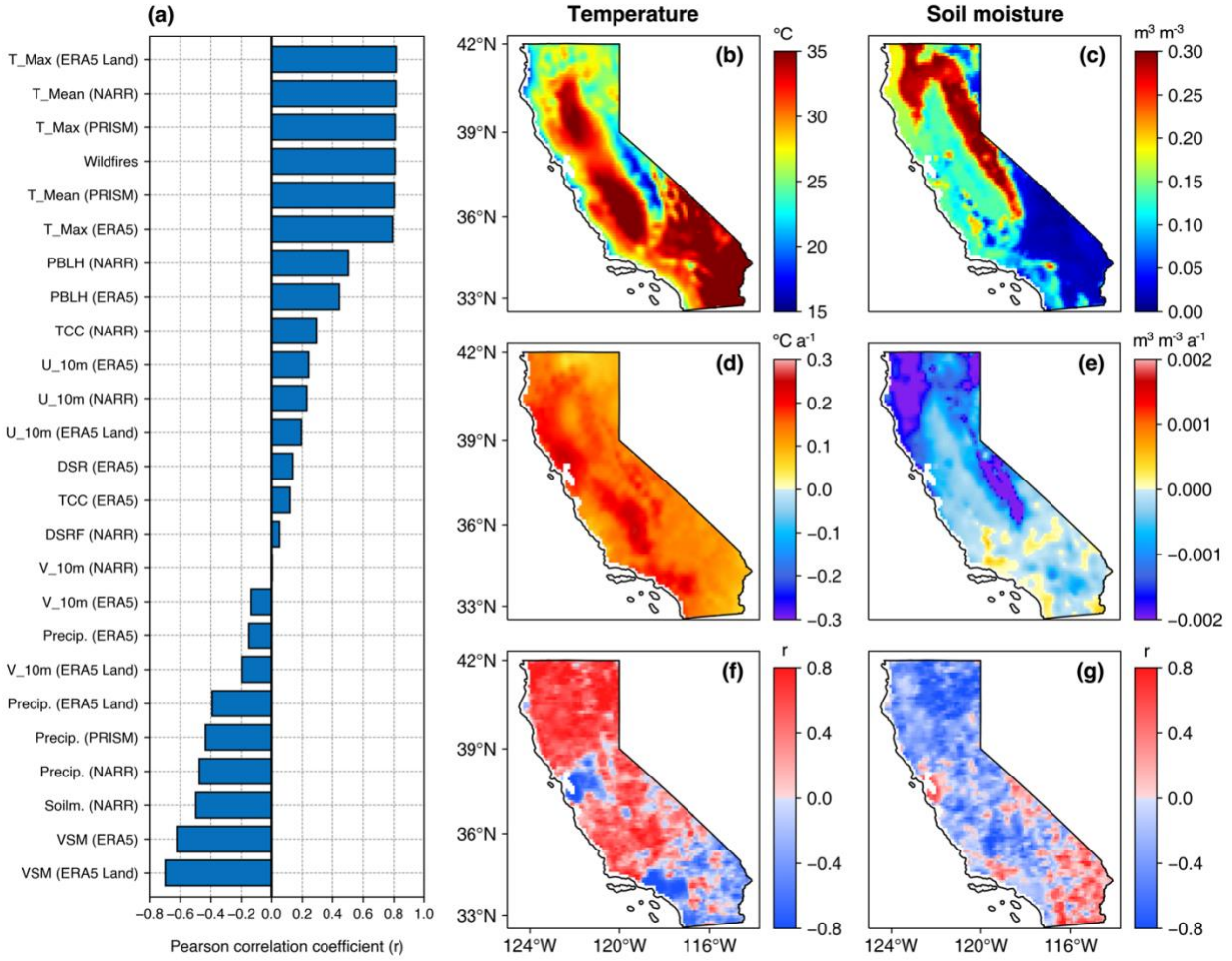

Figure 1.5. (a) *The correlation coefficients between QA4ECV OMI NO_2 columns and meteorological variables and wildfire-burned areas in non-urban areas. The variables from ERA5 and ERA5 Land are the average between 12:00 and 16:00 LT to match the OMI overpass time.* ***(top row)*** *Average distributions and*

*the trends **(middle row)** of ERA5 Land daily maximum temperature, and soil moisture over California from 2009 to 2020 during June–September. **(bottom row)** Maps of the correlation coefficient between daily maximum temperature, soil moisture and the QA4ECV OMI NO_2 columns.*

Following the Berkeley-Dalhousie soil NO_x parameterizations (BDSNP) (Hudman et al., 2012), we apply an exponential function (Eq. 1) and a Poisson function (Eq. 2) to depict the non-linear responses of NO_2 columns to temperature and volumetric soil moisture (VSM) (Fig. 1.6a and Fig. A3). High-fire months in the top 75th percentile of burned area (Fig. 1.7) and the highest 5% of NO_2 columns in each non-urban land type are excluded to eliminate the wildfire effects and remove any elevated NO_2 concentrations transported from urban centers (Lu et al., 2015) on rare occasions. The exponential function performed well in capturing the temperature dependence of NO_2 columns (Fig. 1.6a, $R^2 > 0.95$), consistent with responses of soil NO_x emissions reported in previous studies (Hudman et al., 2012; Steinkamp and Lawrence, 2011; Yienger and Levy, 1995). We find that in croplands and scrublands, our results agree with the BDSNP parameterization assuming a soil NO_x emission that increases exponentially followed by a plateau at 30 °C; however, in forests and barren lands we observe NO_2 columns reach their maxima at air temperatures closer to ~33 °C. This is possibly due to the difference in air vs. soil temperatures, but that effect would most likely work in differing directions during midday in summer over forests (cooler soils) than over non-vegetated lands (warmer soils). Another possibility for the difference could be microbial adaptions to high temperatures or the importance of deep, cooler soil layers to total NO_x emissions (Oikawa et al., 2015).

An encouraging feature of the temperature curve fits is that all land types tend to yield a very similar offset of ~$6.6 \pm 0.6 \times 10^{14}$ molec/cm^2, which is comparable to the values consistently observed well offshore in TROPOMI (Fig. 1b) (Goldberg et al., 2021) and OMI retrievals (~$5.5 \pm 0.6 \times 10^{14}$ molec/cm^2) with no significant trend during 2009–2020 (Fig. A4) (de Foy et al., 2016).

Another realistic aspect of the temperature fits presented in Fig. 1.6a is that the pre-exponential factors are related in magnitude in a manner consistent with the "wet" emission factors outlined in the original Yienger and Levy (1995) parameterization with croplands being the largest (due to the higher available reactive N), scrublands (including open and closed shrublands, savannahs, and grasslands) are similar but smaller, and forests (including deciduous, evergreen, and mixed) an approximate order of magnitude smaller. On the other hand, the larger temperature coefficients in our exponential fits indicate a much stronger temperature dependence than those of Yienger and Levy (1995) and the other common parameterizations since (Hudman et al., 2012; Sha et al., 2021) across all landscapes. After removing the offsets, the ratio of soil emissions for our data between 30 °C and 20 °C is a factor of 6.9 larger, whereas the traditional parameterizations predict an increase by a factor of 2.8. A recent study focusing on high-temperature agricultural soils (Y. Wang et al., 2021) proposed a stronger soil temperature dependence between 20–30 °C and a higher threshold temperature at which emissions plateau (40 °C) relative to prevailing parameterizations. Both of these characteristics are qualitatively supported by our results across all landscapes in California illustrated in Fig. 6a.

By controlling the ratio of oxygen to water in the soil pore space, soil moisture is another important factor regulating soil NO_x emissions (Pilegaard, 2013). Distinctly different VSM dependences of NO_2 columns are observed for the four non-urban land types (Fig. 1.6b), although they have similar patterns to the typical dependence of soil emission parameterizations (Hudman et al., 2012; Pilegaard, 2013). That is, the NO_2 columns are low in both extremely dry and wet conditions with the highest NO_2 columns observed at moderate VSM between 0.03–0.14, which can be accurately represented by the fit Poisson function ($R^2 > 0.73$). Most VSM parameterizations fix their peak emissions at around 0.2 to 0.3, but because soil moisture tends to have established

strong vertical gradients in the top 10–20 cm, from whence most NO emissions originate (Peirce and Aneja, 2000), it is not easy to make direct comparisons with the values obtained from the reanalysis data sets.

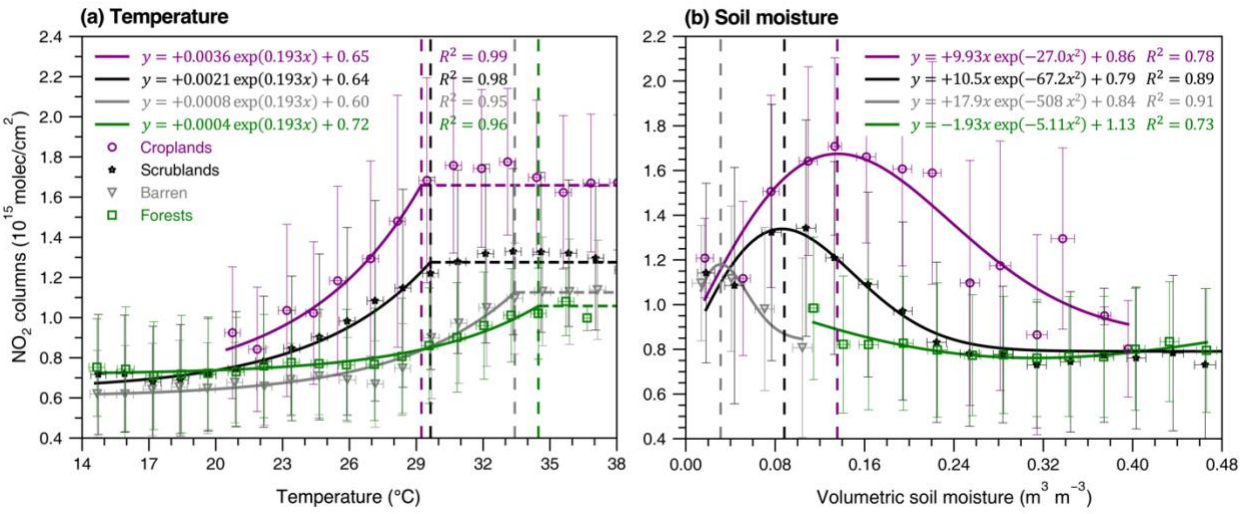

Figure 1.6. (a) *Relationship between QA4ECV OMI NO_2 columns and daily maximum temperature under different land covers. The solid lines are fitted exponential curves (Eq. 1), and the vertical dashed lines represent the end of the temperature-sensitive regimes.* ***(b)*** *Relationship between NO_2 columns and soil moisture. The solid lines are fitted Poisson curves (Eq. 2). The vertical dashed lines indicate the maximum of the fitted curves. The scatter plots are binned by meteorological variables with standard deviation shown on each bin. R^2 represents the coefficient of determination.*

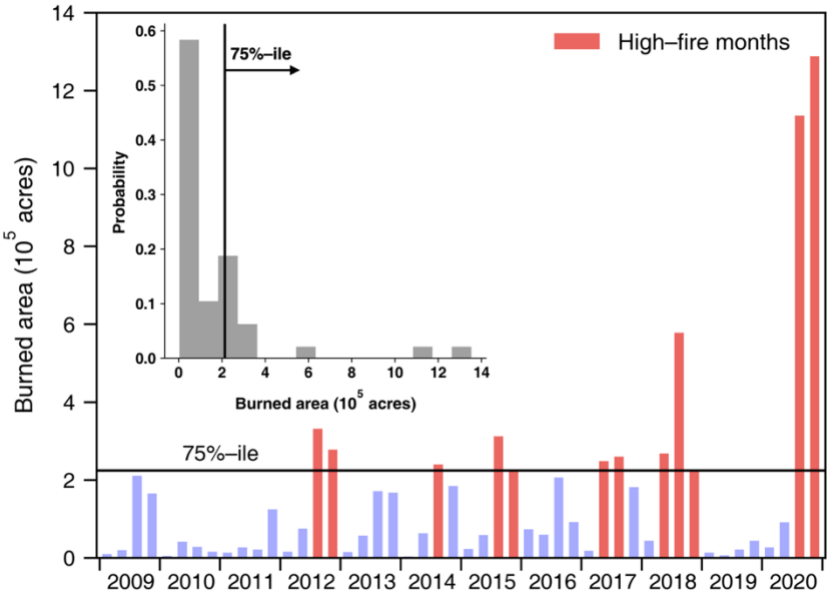

Figure 1.7. *June–September monthly wildfires burned areas from 2009 to 2020 in California. The insert shows the probability distribution of the monthly burned areas. The months with the top 75th percentile of burned areas are defined as the "High-fire months".*

Using the empirically fit relationships shown in Fig. 1.6, we calculate the trends of NO_2 columns that are driven by temperature and VSM changes to estimate how much of the observed trends can be ascribed to soil NO_x emissions (Fig. 1.8). We use the sum of temperature and VSM-driven NO_2 column changes to represent the soil emissions. The results reveal that soil emissions can explain about one-third of the OMI NO_2 trends over all non-urban areas but this ranges from nearly all in scrublands to less than 10% of observed change in forested regions. This important environmental soil NO_x enhancement is dominated by the temperature-driven response, rather than the VSM-driven response, mostly because temperature has a more significant trend (~1.2 °C decade^{-1}) than soil moisture (~1% decade^{-1}) over the study period (Fig. 1.5d-e). In particular, scrublands show the largest increase (0.48×10^{13} molec/cm^2 a^{-1}), followed by forests (0.28×10^{13} molec/cm^2 a^{-1}), and then croplands (0.17×10^{13} molec/cm^2 a^{-1}), with barren areas indicating no net change from changing soil conditions. It is worth noting that although the temperature dependence of NO_2 columns is strongest in croplands in the temperature range between 20 – 30 °C, the predicted soil emission change is small because of the plateau above ~30 °C. This is because only 6.6% of the summertime temperatures over croplands fall below the threshold in the temperature-sensitive regime during OMI overpass time (~13:30 LT) (Fig. A5a), thereby muting the climate warming effects. Nearly half of all scrublands, on the other hand, appear to be at temperatures below its plateau temperature making their overall emissions much more susceptible to rising temperatures (Fig. A5b). Because of their higher average temperature plateau threshold and elevations, forest soils are mostly all susceptible to increasing temperatures even though their emissions are relatively smaller than those in croplands and scrublands. The TEMPO air pollution monitoring instrument is planned to launch on an upcoming geostationary satellite (Zoogman et

al., 2017) in 2023, and will greatly help to better quantify the changing climatic effects of soil NO_x emissions.

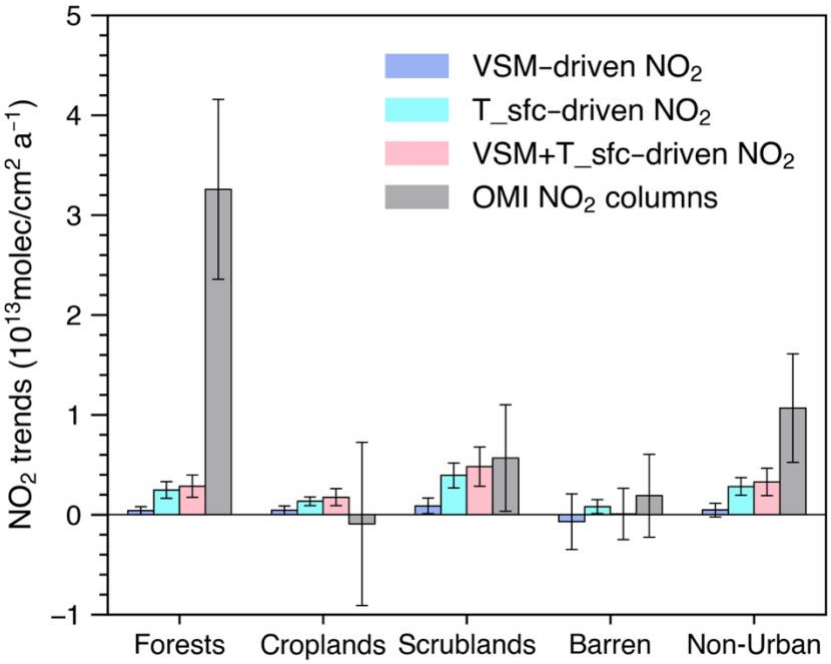

Figure 1.8. *Trends of June–September average QA4ECV OMI NO_2 columns and the components driven by temperature and soil moisture changes across forests, croplands, scrublands, barren, and total non-urban areas of California during 2009–2020.*

3.4. Wildfire Effects

A recent study of the background NO_2 in the US revealed that soil emissions, lightning, and meteorological changes simulated by the GEOS-Chem model could not fully explain the observed decadal rise in remote NO_2 during summer (Qu et al., 2021) and further suggested that deficiencies in the model's treatment of wildfire NO_x could be the culprit. Another study by Wang et al. (2021) suggested that the abrupt deceleration in NO_x reductions observed in 2009 was due to a coincident change in the soil and lightning emissions at that time, conceding that wildfire emissions while rising rapidly (~6.5 $\%a^{-1}$) were still too small of a source to influence total NO_x trends accounting for only 1.9% of the US inventory in the period from 2005-2019. Although this work and a number of other studies have demonstrated an underestimation of soil NO_x emissions (Oikawa et al., 2015; Almaraz et al., 2018; Sha et al., 2021; Y. Wang et al., 2021) in current models, we further infer

that the dramatically increasing biomass burning activity over the past two decades (Li and Banerjee, 2021) is another critical factor contributing to a dramatic shift in background NO_2 trends. Fig. 1.9a shows the differences in NO_2 trends after removing the upper 75th percentile wildfire-impacted months as measured by statewide area burned (Fig. 1.7). This upper quartile threshold was selected because there were months in this range across most of the study period from 2012 onward. Statistically significant decreased rates are observed in all urban ($–2.1\times10^{13}$ molec/cm^2 a$^{–1}$ reducing the trend from –4.2 to –3.7 %a^{-1}) and non-urban land cover types (Fig. 1.9a), with the most pronounced declines found in forests ($–1.8\times10^{13}$ molec/cm^2 a$^{–1}$), followed by croplands ($–1.6\times10^{13}$ molec/cm^2 a$^{–1}$) and scrublands ($–1.4\times10^{13}$ molec/cm^2 a$^{–1}$), and a relatively minor impact in barren regions ($–0.7\times10^{13}$ molec/cm^2 a$^{–1}$), while our result reveals the offshore background NO_2 trends are not affected by wildfires (Fig. A4). Considering that the warmer and drier conditions during high-fire months may also enhance the soil NO_x emissions, we further compare the predicted temperature and VSM-driven NO_2 changes with the OMI NO_2 columns to isolate the influences from wildfires and soil emissions (Fig. 1.9b). Our results reveal that these two factors have comparable influences on the NO_2 concentrations across the entirety of non-urban regions, although their contributions varied significantly in different land covers. For example, the NO_2 columns in croplands and scrublands show similar enhancements, with wildfires being the major contributors (84%) in croplands, while soil emissions have a greater impact on scrublands (63%). Recall from Fig. 1.4 that the fossil fuel effects are minimal in the remote forest and barren regions, and so we calculate the effects of wildfires on the NO_2 trends in these two surface types by subtracting the influence of temperature and soil moisture from the OMI NO_2 columns. The results further show that the substantial rise in summertime NO_2 concentrations in forest habitats is mostly driven by increasing wildfire emissions, accounting for 91% of the OMI NO_2 trend. This

hypothesis is further supported by the fact that the NO_2 columns in forest regions show a much weaker trend ($0.4 \pm 0.8\times10^{13}$ molec/cm^2 a^{-1}) during the winter months (December–March) when the NO_2 columns are not significantly affected by the wildfires (Fig. A6). For barren lands, wildfire is also the major driver of their moderately increasing trends.

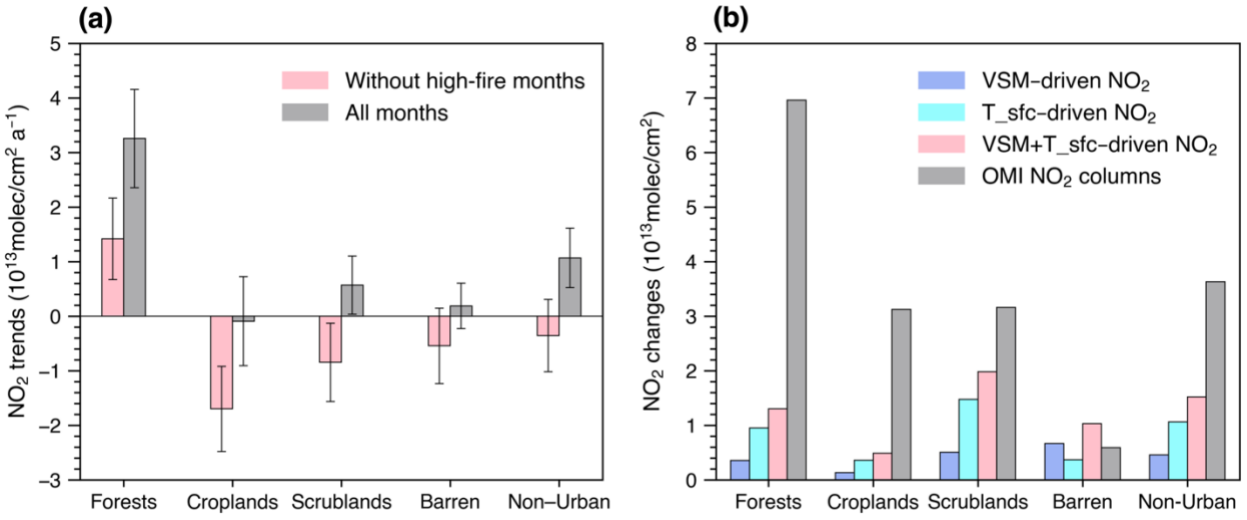

Figure 1.9. (a) *Trends of June–September average QA4ECV OMI NO_2 columns for all months and those without the high-fire (upper quartile) months during 2009–2020. The error bars show the standard deviation of the trends.* ***(b)*** *Changes in QA4ECV OMI NO_2 columns and temperature and soil moisture-driven NO_2 columns between all months and without high-fire months.*

3.5. Future Implications

Fig. 1.10a graphically demonstrates the alarming increase in California burned areas which can be represented by an exponential function since the 1970s (R^2=0.32) (Abatzoglou and Williams, 2016) with a doubling time scale of about a decade. Given the linear responses of NO_2 columns to burned areas (R^2 = 0.14, Fig. 10b) (Mebust et al., 2011), and the NO_2 trends driven by temperature and VSM as shown in Fig. 1.8, we crudely predict the approximate NO_2 changes in 2050 for the remote forests and barren regions by simply extrapolating these wildfire and soil emission effects (Table 1.2). Our results indicate that the NO_2 concentrations in the forests could

be more than four times larger than current levels in 2050 if the fire activities continue to increase in the coming decades as expected in California (Abatzoglou and Williams, 2016). Although our results reveal that NO_2 columns over barren land have minor responses to both wildfires and soil emissions, its NO_2 concentration is also predicted to increase by 22.5% in 2050. These results are intended only to serve as a coarse warning not to represent a precise forecast, because the exact controls on wildfires are manifold and complex. Moreover, there are many feedbacks that remain highly uncertain such as the accumulation of N in soils as wildfire emissions continue to rise leading to soil microbial changes and lag effects that may further influence future soil emissions. In any event, significant rises in background NO_2 will likely resist the continuation of gains from fossil fuel NO_x controls and represent a growing challenge for future air quality management across the state and potentially across the entire western US.

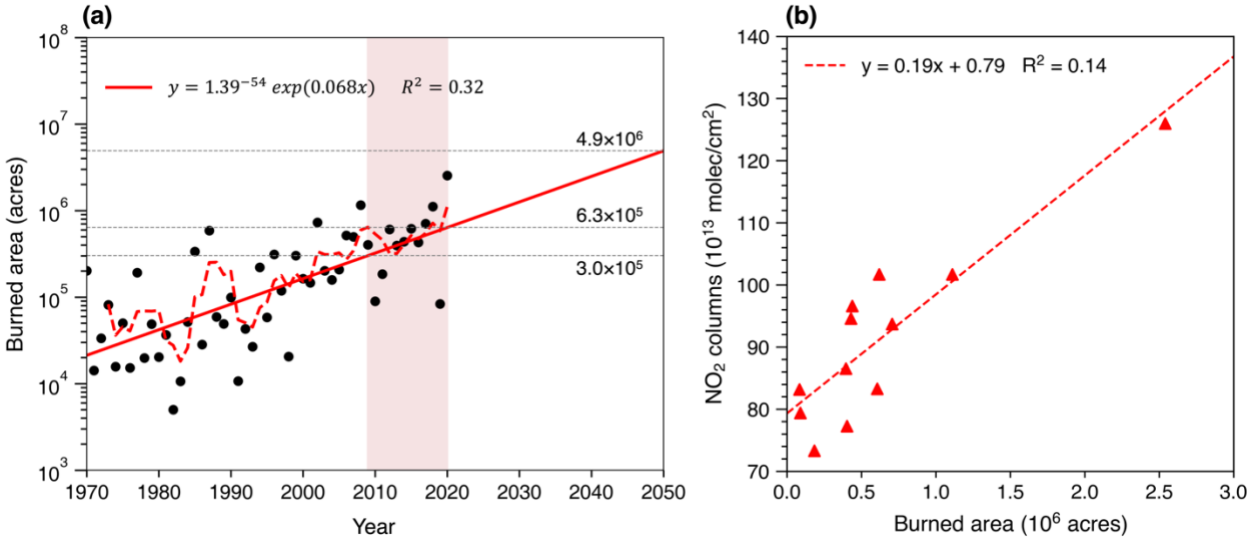

Figure 1.10. (a) *Observed June–September average wildfire burned area during 1970–2020. The red dashed line is moving averaged by 4 years. The red solid line is the fitted exponential curve of the burned area. The horizontal dashed lines represent the predicted burned areas in 2009, 2020, and 2050 from the fitted curve. R^2 represents the coefficient of determination.* ***(b)*** *The scatter plot and linear regression for the burned area compared to the QA4ECV OMI NO_2 columns in forests. The effects of temperature and VSM changes have been subtracted from the NO_2 columns.*

Table 1.2. *Predictions of June–September average NO_2 changes driven by soil moisture, temperature, and wildfires in California forests and barren lands during 2009–2020, and 2020–2050 (10^{13} molec/cm^2).*

Period	Soil moisture	Temperature	Wildfires	OMI/Total
		Forests		
2009–2020	+0.4 ± 0.4	+2.7 ± 0.9	+32.7 ± 9.3	+35.8 ± 9.9 (+46.3%)
2020–2050	+1.2	+7.3	+415.5	+424.0 (+329.6%)
		Barren		
2009–2020	–0.8 ± 3.1	+0.9 ± 0.8	+2.0 ± 5.6	+2.1 ± 4.6 (+2.7%)
2020–2050	–2.2	+2.3	+25.4	+25.5 (+22.5%)

4. Conclusions

Using long-term (2009–2020) observations from the OMI satellite measurements, this study depicts spatial patterns in summertime NO_2 trends across California. Our results reveal a significant NO_2 improvement within cities ($-3.7 \pm 0.3\%a^{-1}$), while the non-urban regions show either no detectable changes or steadily increasing NO_2 concentrations. We then quantitatively evaluate the impacts of the major NO_x sources, focusing on three main sources: fossil fuel emissions, soil emissions, and wildfire emissions. In general, the rising soil and wildfire emissions combined are mostly offsetting the anthropogenic NO_x decline over non-urban portions of the state, and the wildfires play a more important role in determining the NO_2 trends than the soil emissions, although the relative contributions of these two sources vary a lot in distinct land types. In particular, our results reveal that NO_2 concentrations in forest areas show the most pronounced enhancements ($+4.2 \pm 1.2\ \%a^{-1}$) and is mainly driven by wildfires, which is expected to increase further by ~330% by 2050 under the warming climate of California. With continued progress in regulating fossil fuel NO_x emissions, these less-understood NO_x sources will become increasingly important to air quality control strategies in California. Our results point to opportunities for different sets of policies and technologies to assist in reducing NO_2 concentrations in rural and

economically disadvantaged areas of California, but will require a concerted effort to better understand the exact environmental dependence of soil and wildfire emissions.

Supporting Information A

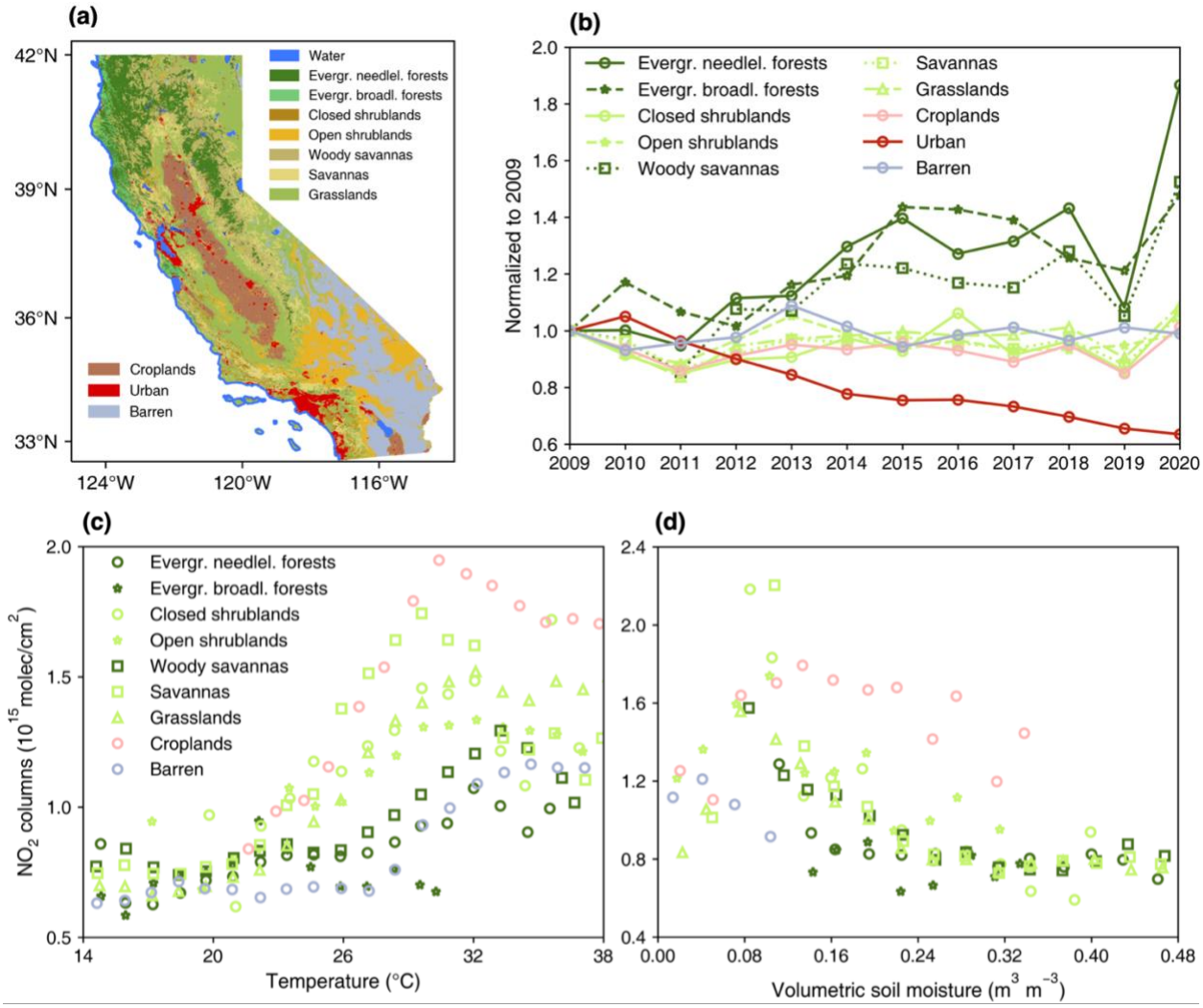

Figure A1. ***(a)*** *Map of the MODIS land covers across California.* ***(b)*** *Trends in June–September average QA4ECV OMI NO_2 columns at each land cover class that makes up at least 1.0% of the total area in California. The trends are normalized to a value of 1 in 2009. The relationship between NO_2 columns to* ***(c)*** *temperature and* ***(d)*** *soil moisture in each land cover type. The types belonging to the same category in Table A1 with similar relationships are marked with the same color.*

Table A1. *June–September average QA4ECV OMI NO_2 columns and their annual trends from 2009 to 2020 for each MODIS land cover type.*

Simplified land cover	MODIS land cover	Area percentage (%)	NO_2 columns (10^{15} molec/cm^2)	NO_2 trends (% a^{-1})
Forests	Evergreen needleleaf forests	11.4	0.89	+5.3 ± 1.5
	Evergreen broadleaf forests	1.6	0.81	+3.5 ± 1.0
	Woody savannas	9.8	0.97	+3.6 ± 1.0
Scrublands	Closed shrublands	2.0	1.33	+0.5 ± 0.6
	Open shrublands	11.5	1.30	+0.0 ± 0.4
	Savannas	9.6	1.38	+0.2 ± 0.4
	Grasslands	25.3	1.24	+0.8 ± 0.5
Croplands	Croplands	9.5	1.76	–0.0 ± 0.4
Barren	Barren	15.3	1.14	+0.2 ± 0.4
Urban	Urban	4.0	3.89	–3.7 ± 0.3

Table A2. *Summary of the meteorological datasets used in this study.*

Data source	Variables	Description	Spatial resolution	Temporal resolution
ERA5 (Hersbach et al., 2020)	T_sfc	2m air temperature (°C)	0.25°×0.25°	Hourly
	U_10m	10m U wind component (m/s)		
	V_10m	10m V wind component (m/s)		
	Precip.	Total precipitation (mm)		
	PBLH	Boundary layer height (m)		
	TCC	Total cloud cover		
	DSR	Downward shortwave radiation (J/m^2)		
	VSM	Volumetric soil moisture (m^3/m^3)		
ERA5-Land (Muñoz-Sabater et al., 2021)	T_sfc	2m air temperature (°C)	0.1°×0.1°	Hourly
	U_10m	10m U wind component (m/s)		
	V_10m	10m V wind component (m/s)		
	Precip.	Total precipitation (mm)		
	VSM	Volumetric soil moisture (m^3/m^3)		
NARR (Mesinger et al., 2004)	T_sfc	2m air temperature (°C)	32km×32km	Monthly
	U_10m	10m U wind component (m/s)		
	V_10m	10m V wind component (m/s)		
	Precip.	Total precipitation (kg/m^2)		
	PBLH	Boundary layer height (m)		
	TCC	Total cloud cover		
	Soilm.	Soil moisture content (kg/m^2)		
PRISM (Daly et al., 2008)	T_Mean	Daily mean temperature (°C)	4km×4km	Monthly
	T_Max	Daily maximum temperature (°C)		
	Precip.	Total precipitation (mm)		

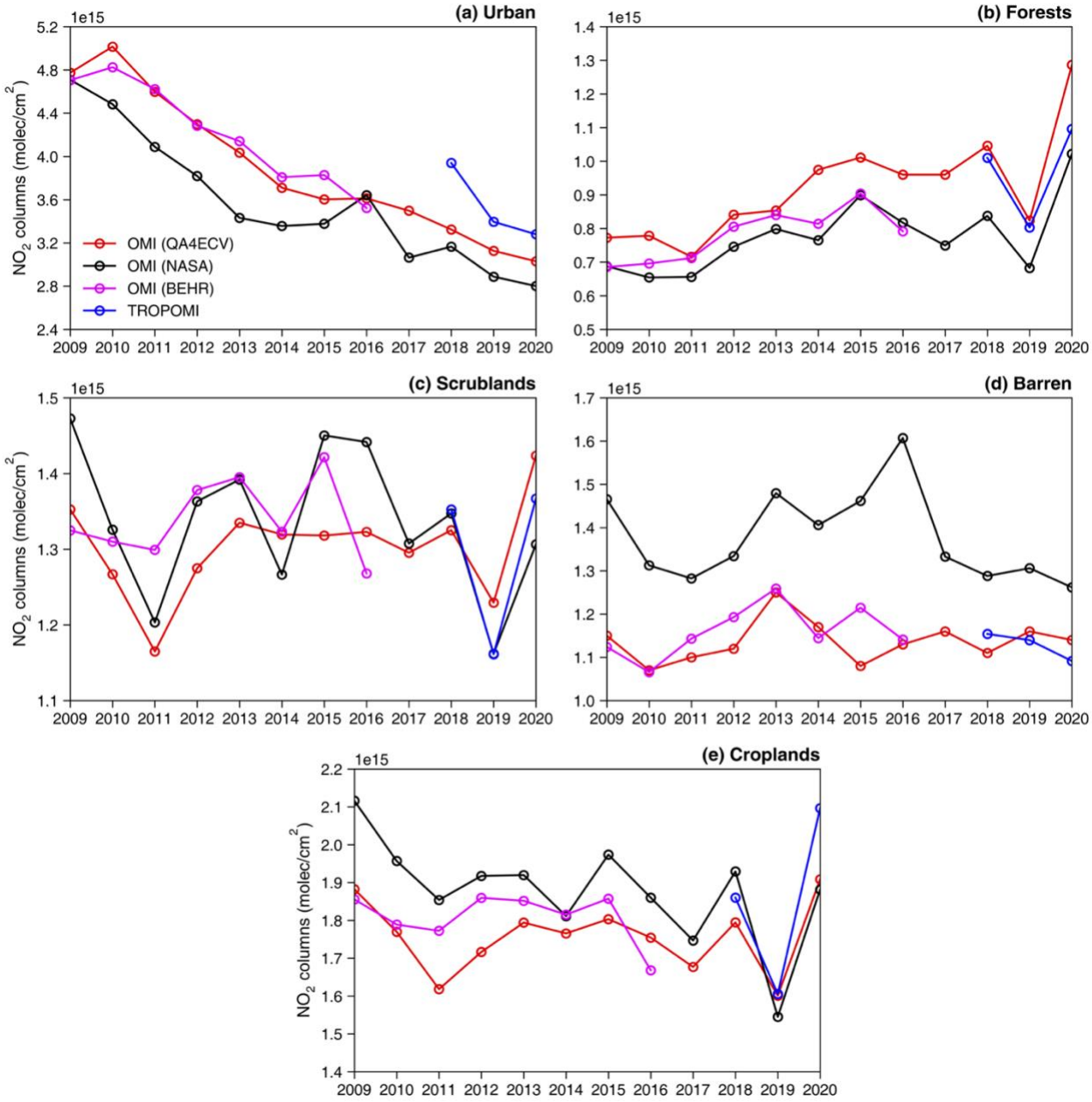

Figure A2. *Trends in June–September average NO_2 columns over* ***(a)*** *urban,* ***(b)*** *forests,* ***(c)*** *scrublands,* ***(d)*** *barren, and* ***(e)*** *croplands from QA4ECV (red), NASA (black), BEHR (purple), and TROPOMI (blue) retrievals.*

Table A3. *The weekly variations in wildfire burned area (acres) and the daily maximum temperature across all land cover types in California.*

Land types	Monday	Tuesday	Wednesday	Thursday	Friday	Saturday	Sunday
Wildfire burned area (acres)							
All types	5363.3	5605.8	5386.2	5078.0	5192.9	5183.2	5303.9
Temperature (°C)							
Urban	30.1	31.0	30.5	30.3	29.9	31.1	30.4
Forests	26.2	26.4	26.4	26.5	25.2	26.8	25.5
Croplands	34.5	34.4	34.6	34.4	34.1	35.0	34.0
Scrublands	29.3	29.6	29.9	29.6	28.9	30.2	29.1
Barren	35.8	35.7	36.7	35.9	35.6	36.8	35.3

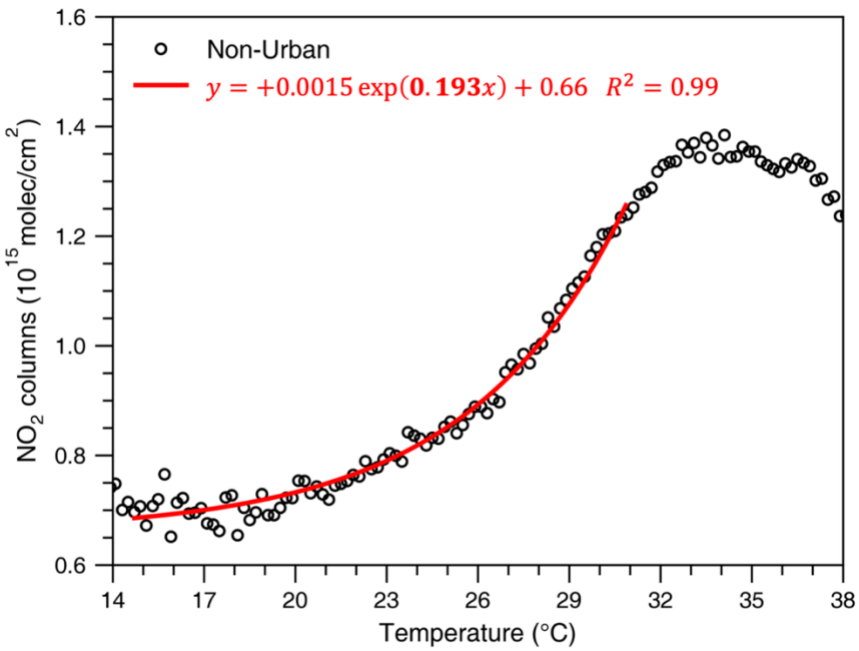

Figure A3. *Scatter plot of QA4ECV OMI NO_2 columns vs. daily maximum temperature over all non-urban regions. The temperature is binned by 0.2 °C. The solid line is the fitted exponential curve based on Eq. 1. R^2 represents the coefficient of determination.*

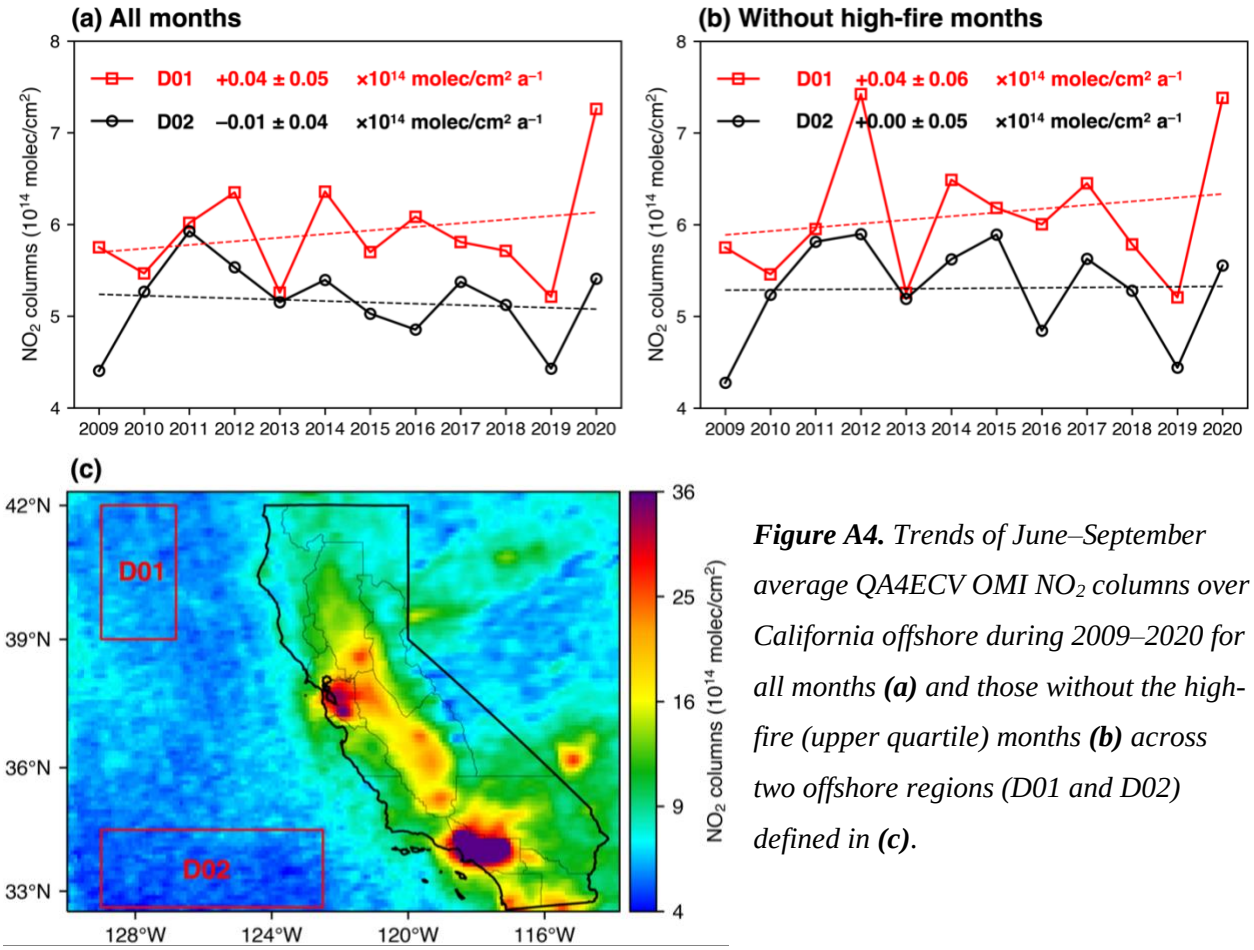

Figure A4. *Trends of June–September average QA4ECV OMI NO_2 columns over California offshore during 2009–2020 for all months* ***(a)*** *and those without the high-fire (upper quartile) months* ***(b)*** *across two offshore regions (D01 and D02) defined in* ***(c)***.

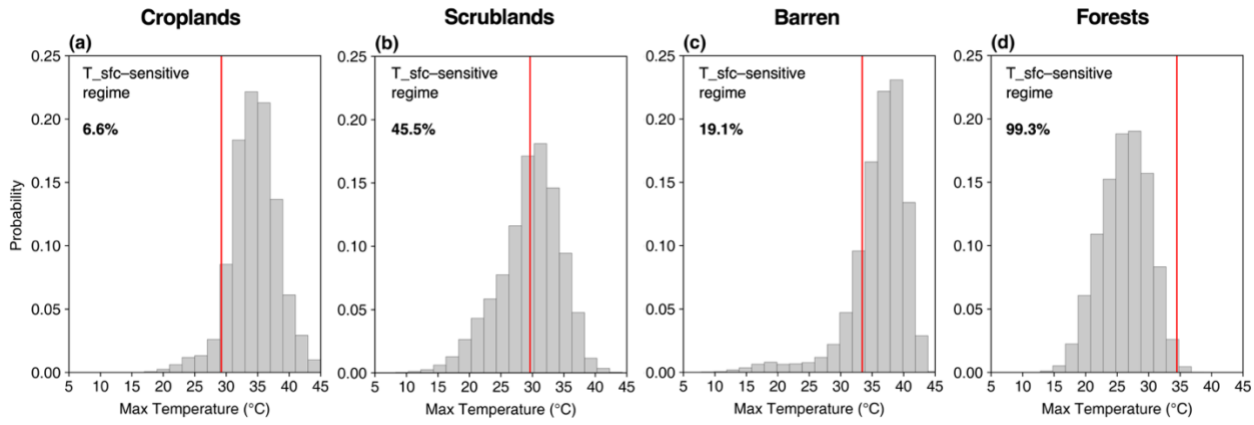

Figure A5. *Probability distributions of June–September monthly mean daily-maximum temperature in croplands, scrublands, barren, and forest land covers during 2009–2020. The red lines represent the maximum temperature of temperature-sensitive regimes.*

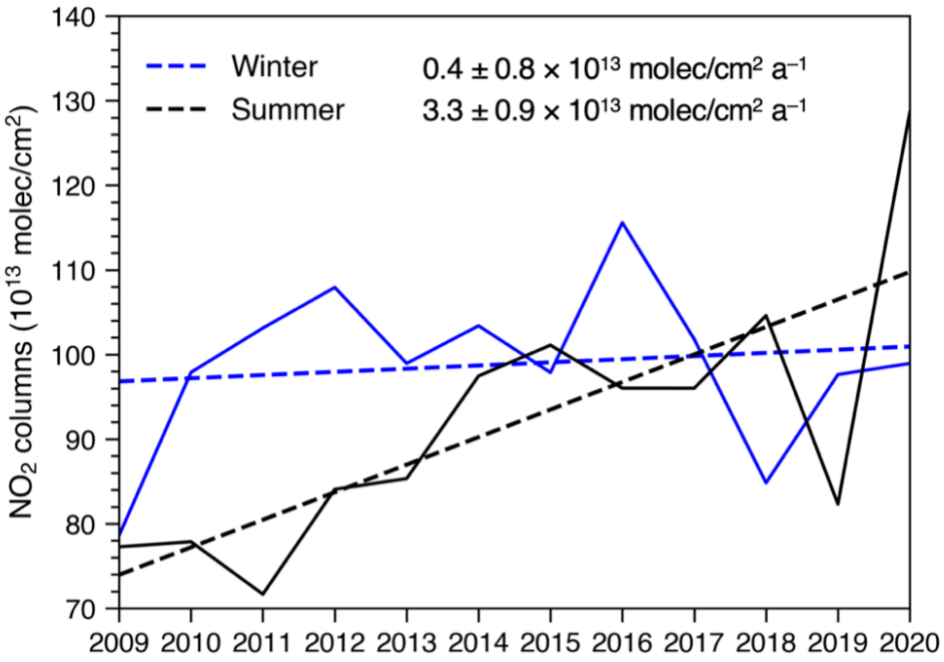

Figure A6. *Trends in June–September (summer) and December–March (winter) average QA4ECV OMI NO_2 columns in forests during 2009–2020.*

Chapter 2: Trends of ozone and precursors in a typical megacity (Chengdu) in China

Wang, Y., Yang, X., Wu, K., Mei, H., De Smedt, I., Wang, S., Fan, J., Lyu, S., and He, C. Long-term trends of ozone and precursors from 2013 to 2020 in a megacity (Chengdu), China: Evidence of changing emissions and chemistry, Atmos. Res., 278 106309, https://doi.org/10.1016/j.atmosres.2022.106309, 2022.

1. Introduction

Ground-level ozone (O_3) is a criteria air pollutant formed through photochemical reactions of precursors including volatile organic compounds (VOCs) and nitrogen oxides (NO_x = NO + NO_2) in the presence of sunlight (Trainer et al., 2000). As a pollutant with strong oxidizing properties, elevated O_3 levels are detrimental to human health, biodiversity, and ecosystems (Liu et al., 2018; Wang et al., 2020). Exposure to high levels of ambient O_3 caused over 0.25 million premature deaths and 4.1 million disability-adjusted life years (DALYs) globally per year (Cohen et al., 2017), and the global mortality burden attributed to tropospheric O_3 is projected to continuously increase under the changing climate (Orru et al., 2013; Stowell et al., 2017; Westervelt et al., 2019). Although the anthropogenic emissions of NO_x have been reduced substantially attributed to strict emission control strategies (Air Pollution Prevention and Control Action Plan, APPCAP) implemented by the Chinese government since 2013, the major city clusters in China including the North China Plain (NCP) (Lyu et al., 2019), Yangtze River Delta (YRD) (Gao et al., 2017; Zhan and Xie, 2022), Pearl River Delta (PRD) (He et al., 2019) and Sichuan Basin (SCB) (Yang et al., 2020) still frequently suffer from excessive regional O_3 episodes, which has become a prominent threat to public health (Liu and Wang, 2020a, 2020b).

The Sichuan Basin (SCB) is a region situated in southwest China. Owing to the intense anthropogenic activities and frequent stagnant conditions in combination with the complex basin landscape, elevated O_3 levels have been frequently observed throughout the SCB from 2013 to

2020 (Wu et al., 2022). As the capital city of Sichuan Province, Chengdu is a highly urbanized megacity with vehicle ownership over 5 million and 20.9 million residents at the end of 2020. The fossil-fuel-dependent industrial infrastructure and strong traffic mobility within the 14,335 km^2 Chengdu city emit substantial primary air pollutants (NO_x, VOCs, primary particle matter (PM), etc.), posing enormous challenges to air quality management and calling for more aggressive mitigation efforts (Zhou et al., 2019). In addition to anthropogenic emissions, strong biogenic VOC (BVOC) emissions emitted from urban green spaces and densely forested surrounding rural areas also contribute to the elevated O_3 levels over Chengdu (Wu et al., 2020; Ma et al., 2022). Epidemiologic studies reported that the probability of exposure to excessive O_3 pollution is even above 70% for the residents of Chengdu (Meng et al., 2021). There remains an urgent need for identifying the governing factors which contribute to the elevated O_3 levels to design effective O_3 control strategy over Chengdu.

Prior studies have examined the variations of O_3 levels and the formation mechanism of O_3 episodes over Chengdu based on ambient measurements and chemical transport models. In field studies, Wu et al. (2017) pointed out the deteriorated O_3 pollution in Chengdu from 2014 to 2016. Tan et al. (2018) utilized an observation-based box model (OBM) to investigate the O_3-VOC-NO_x sensitivity, and reported that alkenes contribute over 50% of the O_3 production in Chengdu. Deng et al. (2019) found that elevated alkenes and aromatics emissions at night are the dominant reasons for O_3 episodes over Chengdu. In terms of numerical modeling, Yang et al. (2020) used the Weather Research and Forecasting and Community Multiscale Air Quality (WRF-CMAQ) model to probe the causes of elevated O_3 concentrations in Chengdu and identified two typical O_3 episodes with dominant effects of regional transport and local emissions, respectively. By using the WRF-CMAQ model coupled with the Integrated Source Apportionment Method (ISAM)

module, Yang et al. (2021b) demonstrated that transportation and industrial sectors were governing contributors to O_3 formation in Chengdu, accounting for over 60% of the maximum daily 8h average (MDA8) O_3 concentration during spring O_3 episodes. Existing studies have identified the roles of elevated anthropogenic emissions and typical meteorological conditions on O_3 levels over Chengdu. However, these studies were mainly focused on examining the changes of O_3 levels in a short period or typical O_3 episodes while the long-term trend remains elusive. Furthermore, the dominant factors that influence the O_3 variability on a long-term basis are still lack of understanding, which crucially limits our ability to deploy systematic O_3 controls in Chengdu.

In this chapter, we investigate the long-term trends (2013–2020) of O_3 levels across Chengdu and infer the precursor emissions by satellite data derived from OMI and TROPOMI, as well as anthropogenic emission inventory. Furthermore, the WRF and the Model for Emissions of Gases and Aerosols from Nature (MEGAN) model are then adopted to probe the impacts of meteorology and BVOC emissions on O_3 air quality in Chengdu over 2013–2020.

2. Materials and Methods

2.1. Air Quality and Meteorological Observations

Hourly observations of air pollutants over Chengdu were collected from the China National Environmental Monitoring Center (CNEMC). There are 5 urban stations (JQLH, DSXL, JPJ, SHP and SWY), 2 traffic stations (LJX and SLD), and 1 rural station (LYS) throughout the Chengdu city. It should be noted that the O_3 measurements are reported in the unit of μg m^{-3} at the standard atmospheric conditions (273.15K, 1 atm) before September 2018, and at 298.15K conditions afterwards (MEE, 2012, 2018). To ensure the units of O_3 levels are consistent during 2013–2020, the O_3 concentrations after September 2018 were converted to the standard atmospheric condition.

Surface meteorological observations in Chengdu are provided by the China Meteorological Data Service Center (CMDSC) and Sichuan Provincial Weather Service with rigorous data accuracy checks. The hourly data of meteorological parameters including 2-m temperature (T2), 2-m relative humidity (RH2), 10-m wind speed (WS10), and 10-m wind direction (WD10) are used to evaluate the surface model performance of WRF.

The vertical profile of temperature (T), dewpoint temperature (Td), and wind speed (WS) are used to evaluate the simulation of the thermodynamic structure of the lower troposphere. Locations of the meteorological, air quality, and radiosonde sites are shown in Fig. 2.1b.

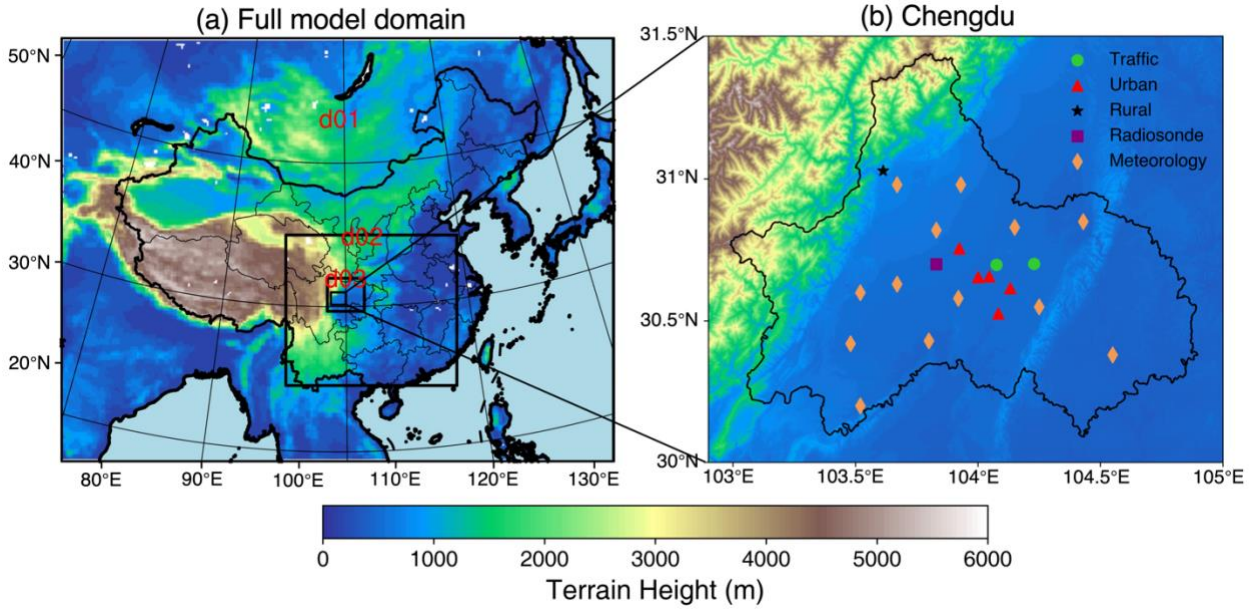

Figure 2.1. (a) *Map of triple nested WRF model domains and* ***(b)*** *locations of the sounding, surface meteorological and air quality observations over Chengdu.*

2.2. Anthropogenic Emission Inventory

The Multi-resolution Emission Inventory of China (MEIC) is a bottom-up emission model developed by Tsinghua University that tracks the variability of anthropogenic emissions in China (Zheng et al., 2018, 2021). The anthropogenic sources were aggregated into five sectors including

agriculture, industry, transportation, residential, and power with a spatial resolution of 0.25°×0.25°. Here, the MEIC emission inventory from 2013 to 2020 was used to probe the long–term changes of anthropogenic NO_x and VOC emissions over Chengdu.

2.3. NO_2 and HCHO columns

To explicitly investigate the trends of NO_x and VOCs emissions over Chengdu, we further adopt the OMI NO_2 and HCHO columns generated by the European Quality Assurance for Essential Climate Variables project (QA4ECV) to characterize spatial changes of NO_x and VOCs (Boersma et al., 2018). The OMI instrument on aboard the NASA's EOS Aura spacecraft measures backscattered solar radiation from the earth in the spectral range 270–500 nm, with a spatial resolution of 13×24 km^2 and a bandwidth of 2600 km. OMI provides daily global measurements of NO_2 and HCHO columns with good performance in inferring the trend of NO_x and VOC emissions (Shen et al., 2019; Shah et al., 2020). In addition, the ratio of HCHO and NO_2 columns (FNR) reflects the relative availability of NO_x and VOCs to peroxy radicals, which has been widely used as a metric of regional O_3-VOCs-NO_x sensitivity (Duncan et al., 2010).

The TROPOMI tropospheric NO_2 columns are retrieved with algorithms based on the OMI QA4ECV heritage (De Smedt et al., 2018; van Geffen et al., 2020). In addition, TROPOMI Level 2 NO_2 columns are oversampled to 0.01°×0.01° based on the algorithm developed by Sun et al. (2018), with cloud fraction lower than 30% and quality assurance value higher than 0.75.

2.4. WRF and MEGAN Model Configurations

Meteorological fields are simulated using the Weather Research and Forecasting (WRFv3.9.1) model. Fig. 2.1 shows the triple nested model domain with horizontal resolutions of 27, 9, 3km, respectively. The innermost domain covers the Chengdu Plain. There are 30 vertical layers from

the ground to 100 hPa, with a surface layer depth of nearly 20 m. The initial and boundary conditions for meteorological fields were obtained from the National Centers for Environmental Prediction (NCEP) Final (FNL) reanalysis data with a resolution of 1.0°×1.0°. To minimize the influence of initial conditions and cumulative error of the model, the simulations were initialized monthly, treating the 3 days before that month as spin-up. The Yonsei University (YSU) planetary boundary-layer scheme (Hong et al., 2006) is adopted in the WRF model because it shows a better performance in representing the surface and vertical meteorological conditions (Text B1-B2). The other physical parameterization schemes selected in the WRF model are listed in Table B1. The evaluation of WRF model performance is presented in Text B3 and Table B5.

MEGANv2.1 was driven by meteorological fields from WRF model to estimate the BVOC emissions for the innermost domain (Guenther et al., 2012). Plant function types (PFTs) are adopted from the MODIS MCD12Q1 product and emission factors are obtained from global database based on PFT-specific emission factors tabulated in MEGAN. The leaf area index (LAI) is derived from Moderate Resolution Imaging Spectroradiometer (MODIS) MOD15A2H LAI product (Wu et al., 2020). It should be noted that urban LAI is not considered in this work due to the limitation of MODIS LAI products.

2.5. Definition of Heatwave and Air Stagnation

Heat waves (HWs) refer to extremely hot periods that last for several consecutive days, which could lead to severe O_3 episodes by enhancing photochemical reactions and BVOC emissions (Zhao et al., 2019). In this study, the HWs is defined as a period of at least 3 consecutive days with the daily maximum temperature > 34 ℃ (Huang et al., 2021; H. Wang et al., 2021).

Air stagnation is characterized by meteorological conditions that impede the scavenging of air pollutants (Xie et al., 2021; Wang et al., 2022). Here, the air stagnation index (ASI) defined by

Horton et al. (2012) is used as an indicator of stagnant conditions. A grid cell is considered stagnant on a given day if three conditions are simultaneously met: the daily average wind speed at 10 m < 3.2 m/s, the wind speed at 500 hPa < 13 m/s, and daily total precipitation < 1.0 mm.

3. Results and Discussion

3.1. NO_2 and O_3 trends over Chengdu during 2013–2020

Fig. 2.2 presents the April–September averaged MDA8 O_3 and daytime NO_2 concentrations (09:00–18:00 LST) across Chengdu during 2013–2020 around a map of TROPOMI tropospheric NO_2 columns with ambient measurements in 2020. Spatially, both satellite NO_2 columns and ambient measurements observed elevated NO_2 levels (30.1 $\mu g/m^3$) over metropolitan area of Chengdu due to intense anthropogenic emissions, while NO_2 concentrations are comparatively low (11.2 $\mu g/m^3$) at the rural site. More pronounced negative trends in NO_2 levels (–2.8 $\mu g\ m^{-3}a^{-1}$) are detected at traffic stations than monitors in urban (–1.6 $\mu g\ m^{-3}a^{-1}$) and rural (–1.2 $\mu g\ m^{-3}a^{-1}$) areas over the period. It is important to note that average daytime NO_2 concentrations at traffic sites are even lower than at urban sites since 2018 (Fig. 2.3a), which provides direct evidence of regulations efforts on reducing traffic NO_x emissions over time.

Unlike continuous decreases in NO_2 levels, O_3 levels exhibit strong inter-annual variability given the non-linear dependence on precursor emissions. For urban and traffic sites, deteriorated trend (+14.0%a^{-1}) of average MDA8 O_3 is observed during 2013–2016 and O_3 levels endure weak reductions with notable interannual variability afterwards. In particular, O_3 concentration descended by –14.1% from 2016 to 2017 and increased by 6.8% during 2019–2020. In contrast, O_3 concentrations at the rural site generally show a downward trend (–2.9%a^{-1}) during 2014–2020. The reasons for these inconsistent O_3 trends between metropolitan and rural areas could be related

to the combined effects of emission changes and different O_3-VOC-NO_x sensitivity (discussed later). It is worth noting that O_3 level at the rural station is comparable or even higher than urban and traffic stations in the spring season, reflecting the effects of regional transport and contribution from background O_3. Furthermore, the monthly average MDA8 O_3 concentrations generally show bimodal distribution for the months between April and September, with peaks in May (Fig. 2.3b). This pattern could be linked to the O_3 subsidence from the upper troposphere governed by synoptic-scale force, which has been reported in Liu et al. (2019) and Yang et al. (2021a).

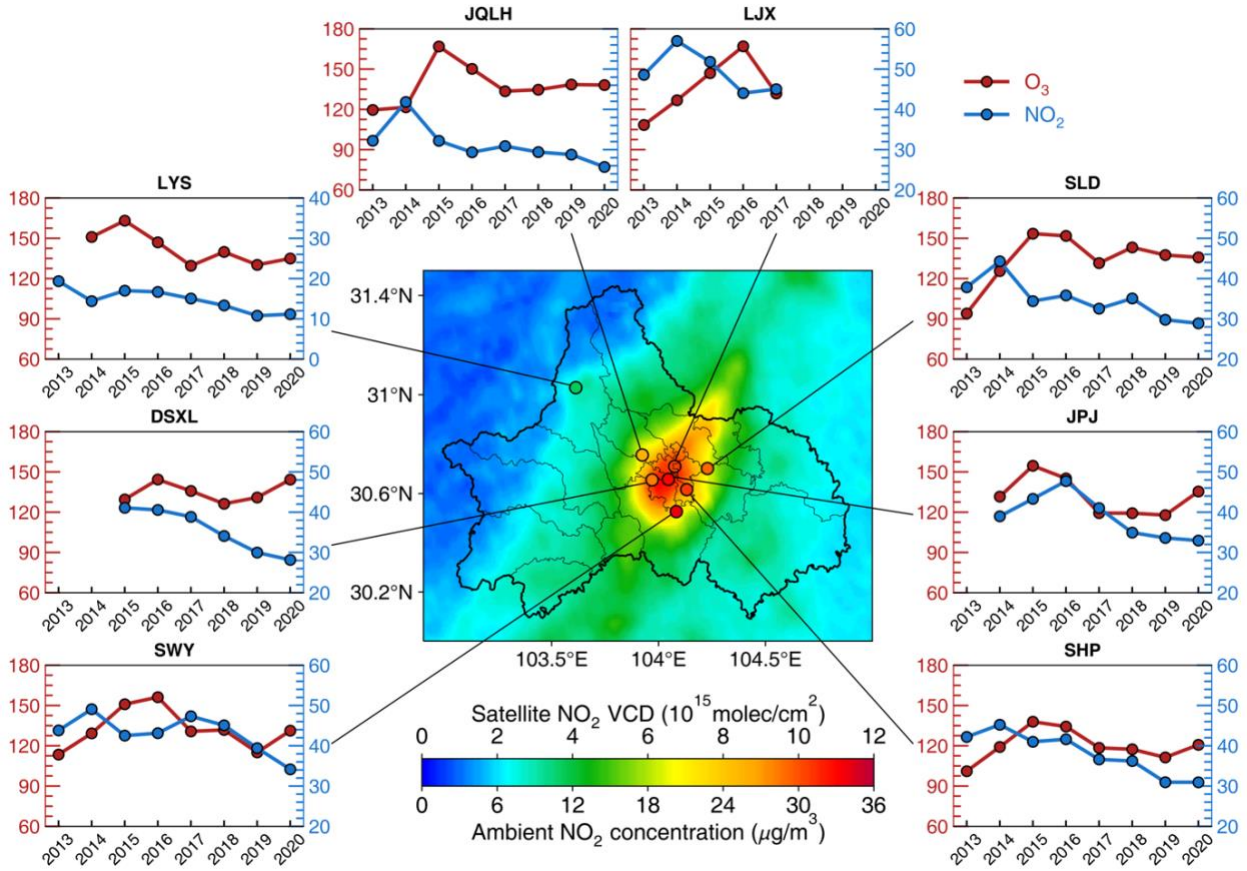

Figure 2.2. *(Middle panel) TROPOMI NO_2 column densities overlaid with averaged (April–September) ambient measured daytime NO_2 concentrations for 2020 in Chengdu. Time series of averaged (April–September) daytime NO_2 and MDA8 O_3 in $\mu g/m^3$ for each site over April–September in Chengdu from 2013 to 2020.*

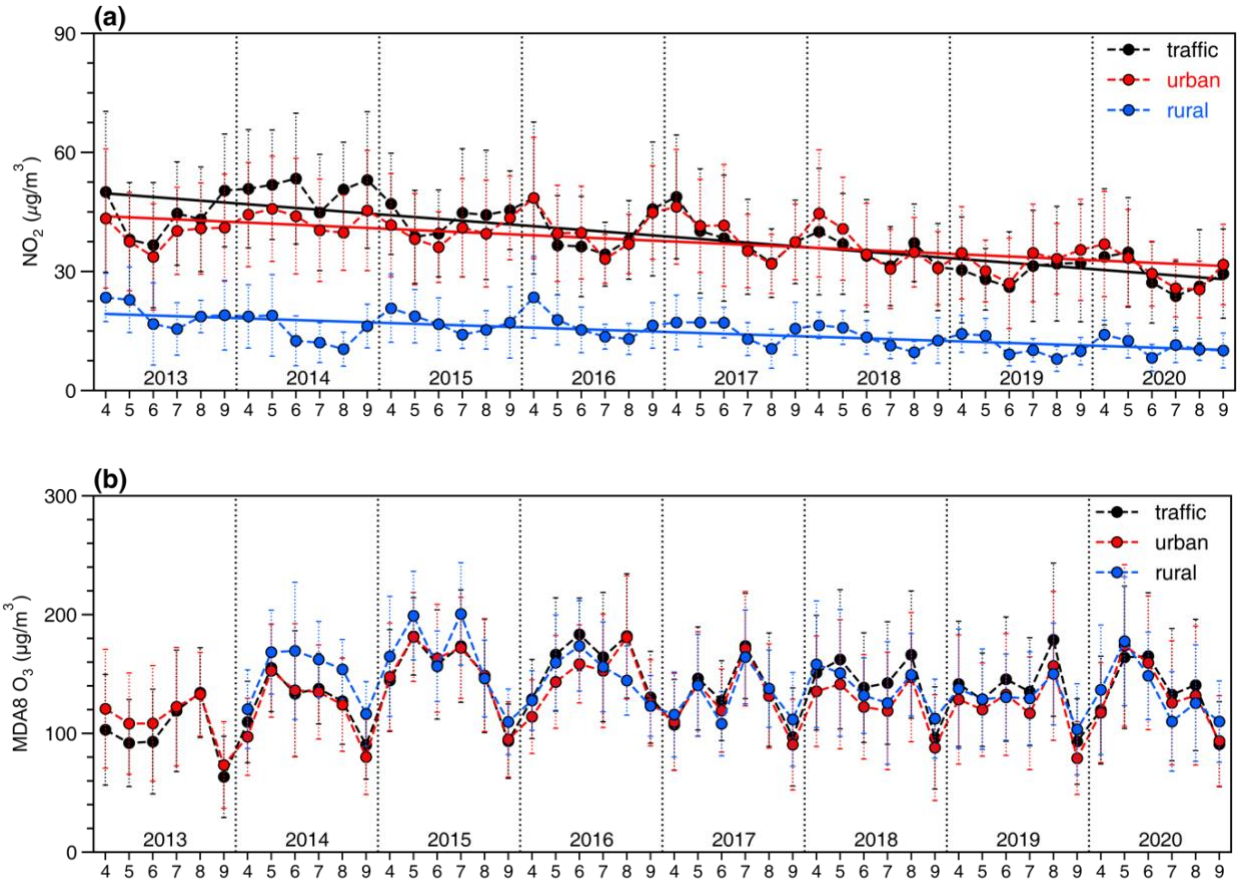

Figure 2.3. *Monthly averaged concentration of daytime NO_2 and MDA8 O_3 for traffic, urban and rural sites over April–September in Chengdu during 2013–2020.*

3.2. Trends of anthropogenic NO_x and VOC emissions over Chengdu

To further explore the variations of NO_x and VOC emissions in Chengdu, the sectoral trends of anthropogenic NO_x and VOC emissions from MEIC during 2013–2020 are presented in Fig. 2.4. In addition, emission changes of NO_x and VOCs attributed to each anthropogenic sector are shown in Fig. 2.5. For NO_x emissions, the MEIC inventory indicates a remarkable decreasing pattern from 283.2 to 206.5 kt, with a reduction ratio of –3.9% a^{-1} during 2013–2020, which is slightly higher than the reduction rate (–3.7% a^{-1}) over the SCB (Wu et al., 2022). This significant decreasing trend is in line with the national emission controls (APPCAP: standard GB 13223-2011) since 2013 (Zheng et al., 2018). Furthermore, the government of Chengdu has further developed

the local strategies to combat air pollution, and put great emphasis on controlling the emission of motor vehicles (Fig. 2.5) (Gao et al., 2020). Therefore, the contribution of transportation sector decreases from 48.4% to 45.2% during 2013–2019, and industrial sector has been the largest contributor to NO_x emissions since 2015. However, a sharp drop in industrial NO_x emissions was found in 2020 (Fig. 2.6a) due to the substantial suspend of industrial activities during the Covid-19 pandemic (Zheng et al., 2021), which leads to the contribution of transportation sector rebounded to 48.0% in 2020.

For anthropogenic VOC emissions, the trend shows a fluctuation pattern with a slight increase from 404.8 to 419.3 kt in 2014 and remains at high levels during 2014–2017. Since August 2017, a stringent VOC emissions standard (DB51/2377-2017) was adopted by the government of Sichuan to tackle the elevated anthropogenic VOCs emissions. As a result, the VOC emissions followed an evenly paced reduction with a prominently descending trend (–5.9% a^{-1}) throughout 2017-2020. More specifically, anthropogenic VOC emissions are dominated by industrial (228.3 kt), transportation (125.7 kt), and residential sectors (50.7 kt), which account for 56.4%, 31.1%, and 12.5% of total emissions in 2013, respectively. It is important to note that contributions of residential and transportation sectors continuously decreased from 2013 to 2017 (8.4% and 25.5%, respectively in 2017), while the contribution from industrial sector increased to 66.5% in 2017 and maintained as the largest source over 2018–2020. Indeed, the industrial sector is the major source of VOC emissions as well as the driver of total emissions changes (Fig. 2.5), which highlights the importance of controlling industrial VOC emissions over Chengdu.

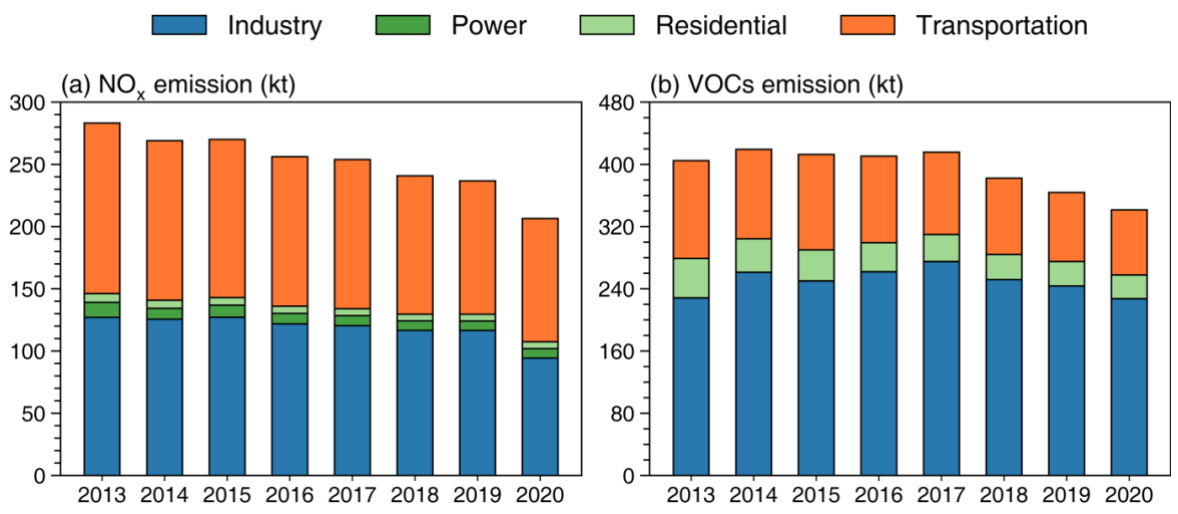

Figure 2.4. *Anthropogenic NO_x and VOCs emissions in Chengdu by source category for 2013–2020.*

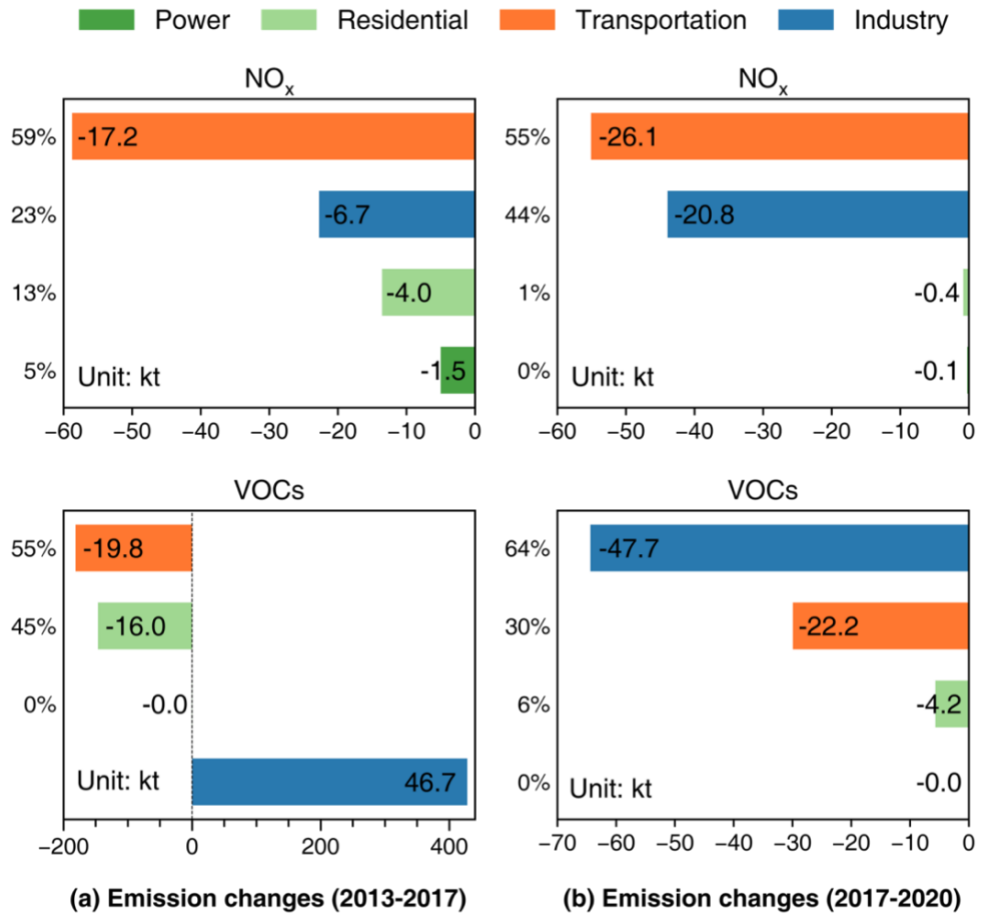

Figure 2.5. *Emission changes of NO_x and VOCs attributed to each anthropogenic sector for* ***(a)*** *2013–2017 and* ***(b)*** *2017–2020.*

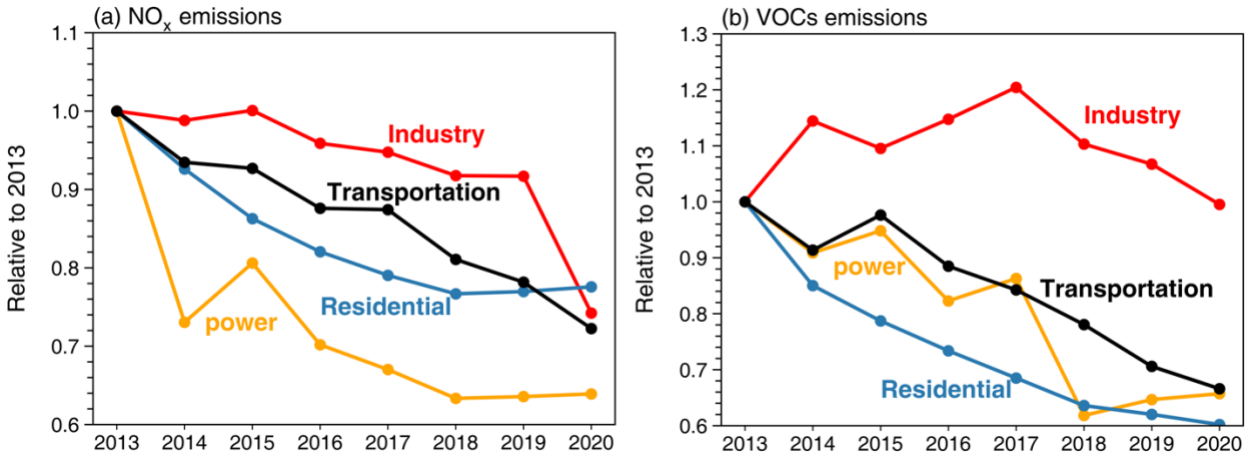

Figure 2.6. *Trends of NO_x and VOCs emissions for each anthropogenic sector during 2013–2020. The trends are normalized to a value of 1 in 2013.*

3.3. O_3-VOCs-NO_x sensitivity over Chengdu

3.3.1. Trend of NO_2 and HCHO columns

Uncertainties in bottom-up emission inventory limit the capability of probing accurate emission changes. Here, we further examine the changes of NO_x and VOCs emissions over time by using satellite-derived NO_2 and HCHO columns. The spatial distribution of NO_2 columns observed by OMI and TROPOMI are presented in Fig. 2.7 and Fig. 2.8, respectively. Despite the discrepancy in 2014, the trend in OMI NO_2 columns closely tracks the NO_x emissions from MEIC inventory and accurately captures the decrease of NO_x emissions (–3.7% a^{-1}) with a steeper trend (–4.5% a^{-1}) during 2013–2020. This steeper slope has also been found by Shah et al. (2020) over central-eastern China, which might be related to the changes of NO_x lifetime due to decrease in NO_x emissions and meteorological variabilities. The OMI NO_2 columns exhibited a steady decrease since 2014, especially for the metropolitan and suburban areas over Chengdu with a more pronounced trend than the SCB (–3.1% a^{-1}) (Wu et al., 2022), suggesting successful regulation efforts in reducing anthropogenic NO_x emissions in Chengdu. Interestingly, OMI NO_2 columns in

metropolitan Chengdu in 2020 are slightly higher than in 2019, which could be attributed to the economic rebound after COVID-19 lockdown. It is worth noting that the spatial variability and magnitude change of OMI NO_2 column is in excellent agreement with TROPOMI NO_2 columns, and both depict a notable decrease during 2018–2020.

Fig. 2.9 presents the comparison of anthropogenic and BVOC emissions and OMI HCHO columns during 2010-2020. Following Shen et al. (2019) and Bauwens et al. (2022), the impacts of temperature variabilities on HCHO columns were eliminated by regressing the HCHO columns onto monthly averaged daily maximum 2m-temperature from the WRF model in each model grid, then the fitted temperature dependency is subtracted from the original data. The temperature-correction algorithm is detailed in Zhu et al. (2017). A weaken correlation is depicted between HCHO columns and BVOC emissions by surmounting temperature dependence. The corrected OMI HCHO columns show a downward trend (–1.7% a^{-1}) with obvious fluctuations during 2010–2020. In the period from 2010 to 2017, despite the inconspicuous increase of anthropogenic VOC emissions (+1.7% a^{-1}), the HCHO columns illustrate a descending trend (–1.6% a^{-1}) with large interannual variability, which could be attributed to significant variations of BVOC emissions. In contrast, the reduction rate of HCHO columns (–6.0% a^{-1}) is coincident with the decline of anthropogenic VOC emissions (–5.4% a^{-1}) during 2018–2020, indicating that the reduction of anthropogenic VOC emissions may act as the major driver for the declining HCHO columns since 2018. Furthermore, it is worth noting that a field campaign with an intensive VOCs measurement network over Chengdu was carried out by Tan et al. (2020) in August 2017 to investigate the response of ambient O_3 and precursors levels to short-term strict emission control. It is found that OMI HCHO column decreased by –24.8% during the control period, which precisely depicted the reductions of ambient VOCs levels ranging from –18.1% to –33.9% based on ground

measurements, adding support to the feasibility of inferring trend of VOC emissions using OMI HCHO columns. Overall, both the regulation of anthropogenic VOCs since August 2017 and BVOC emissions modulated by meteorological conditions present essential roles in determining the trend of HCHO columns, which makes Chengdu a notable exception with a negative trend while the trends observed over China are mostly positive (Bauwens et al., 2022). Spatially, apart from the metropolitan area, the elevated HCHO columns were also observed at the northeastern Chengdu. This phenomenon could be attributed to the local oil refinery industry "China Petroleum Sichuan Petrochemical Corporation" which contributes approximately 8.9 kt VOC emissions each year. It should be noted that the changes between VOC emissions and HCHO columns are inconsistent during 2012–2013 and 2017–2018. Possible reasons for these discrepancies including uncertainty in emission inventory and satellite retrievals, as well as the potential impact of meteorological variability (Shah et al., 2020). However, detailed causes of this phenomenon warrant further investigation.

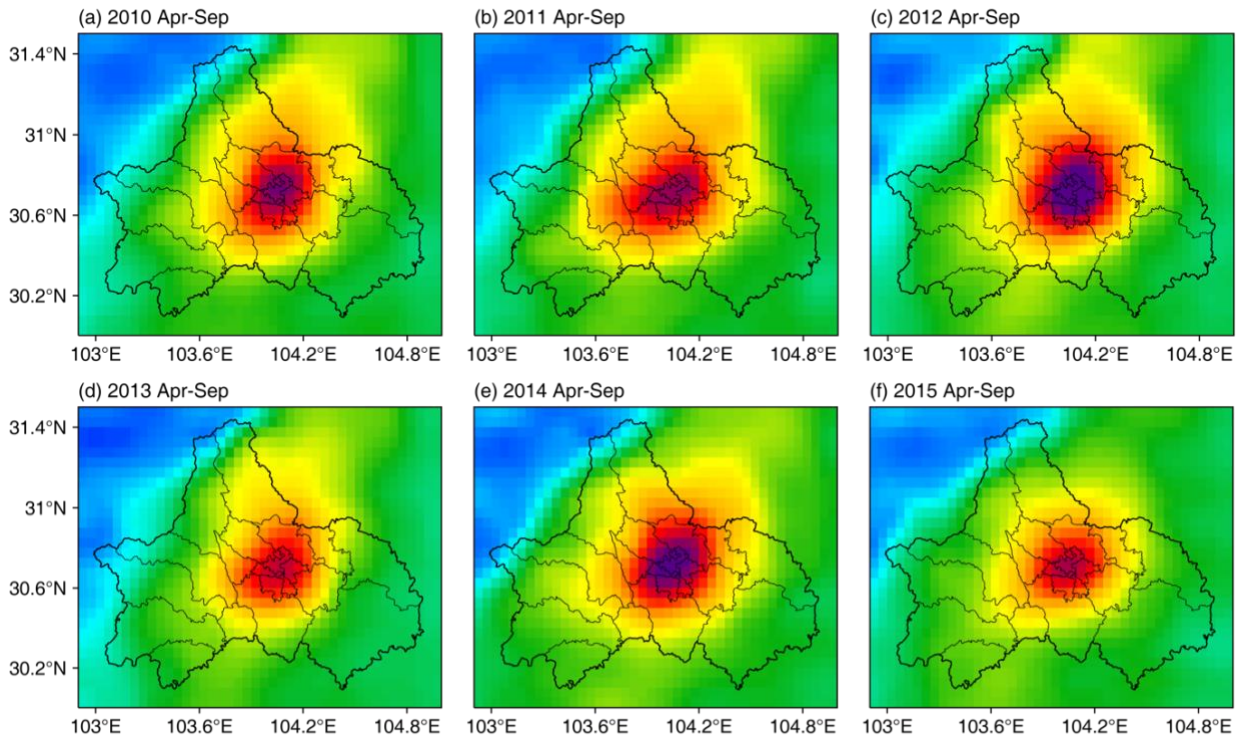

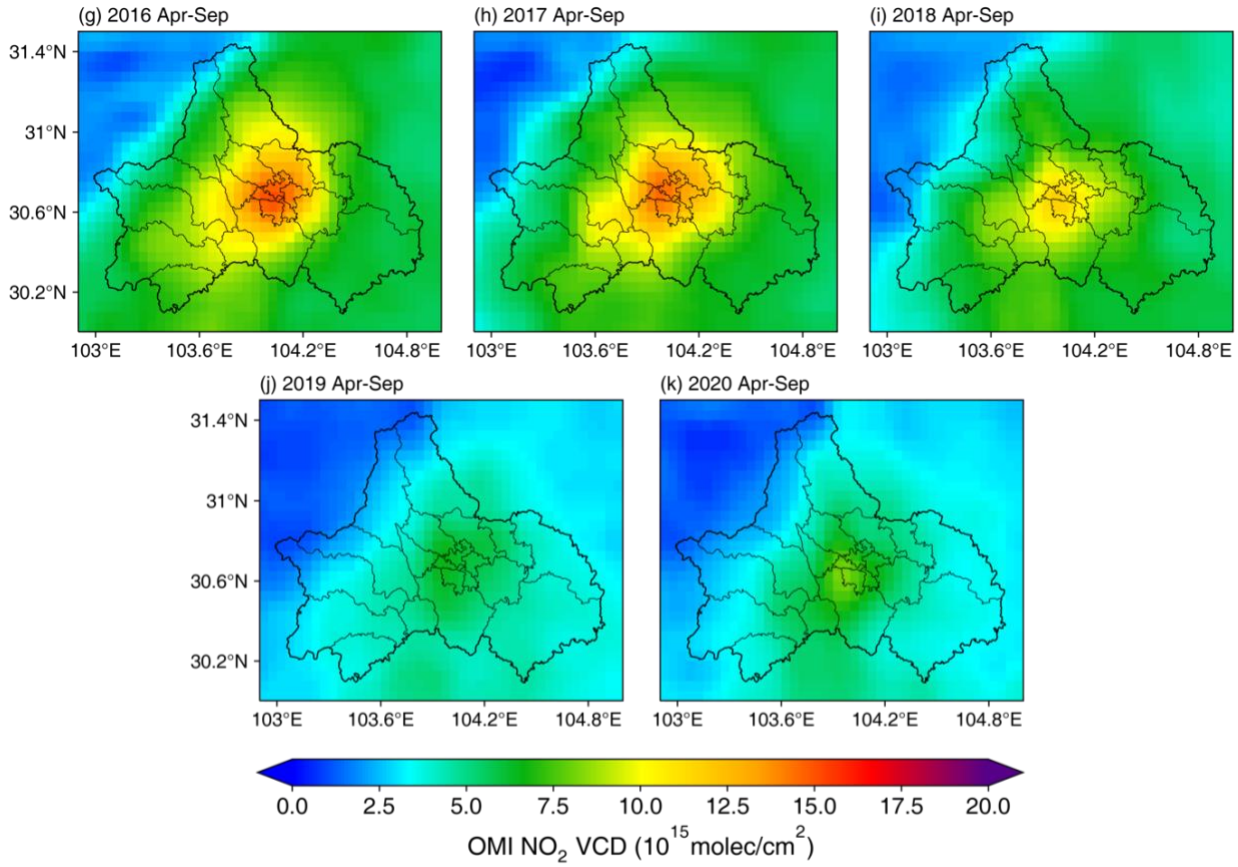

Figure 2.7. *OMI NO_2 vertical column densities averaged over a 6-month period April–September from 2010 to 2020 in Chengdu.*

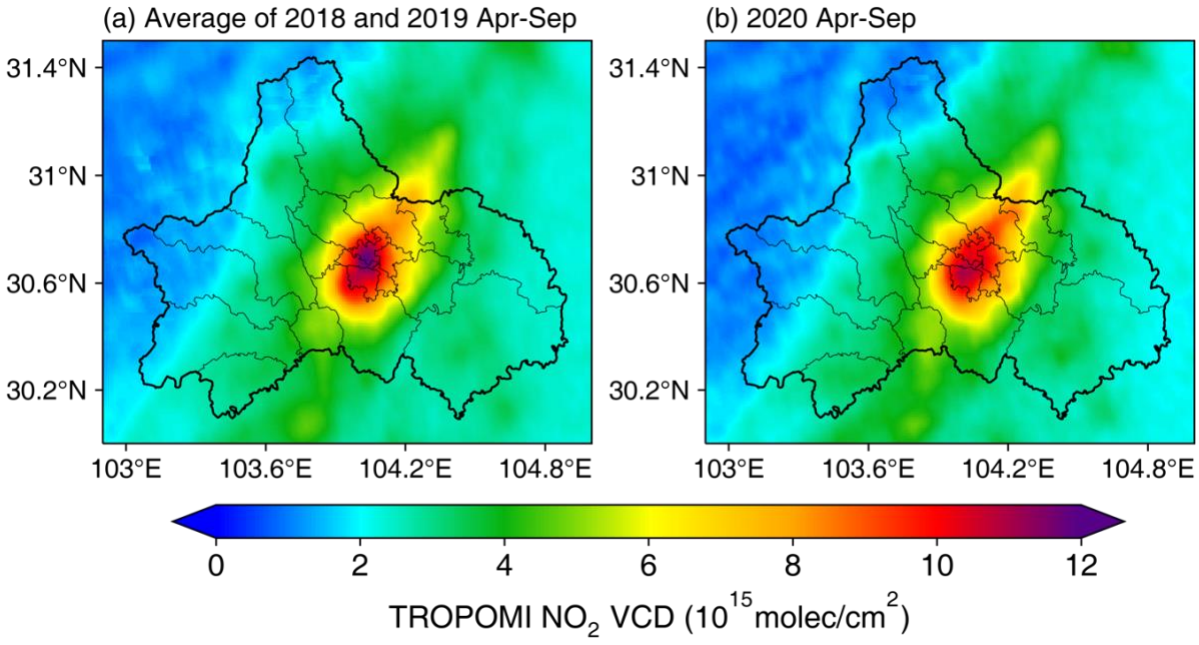

Figure 2.8. *TROPOMI NO_2 vertical column densities averaged over a 6-month period April–September from 2018 to 2020.*

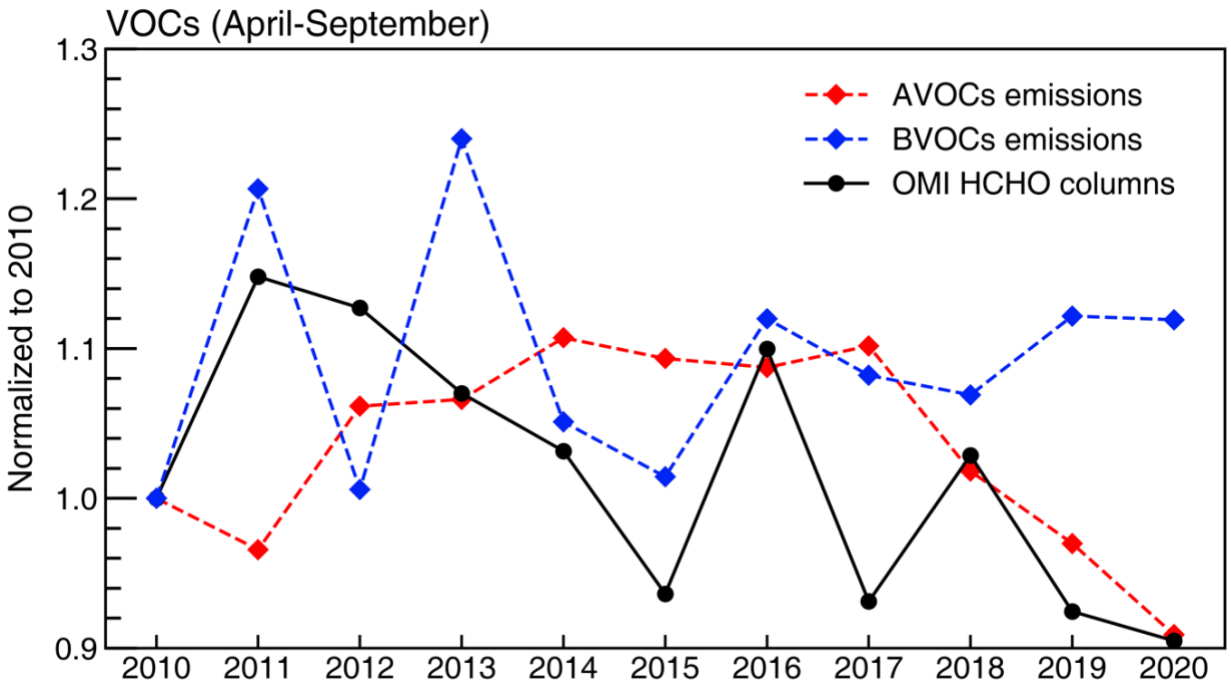

Figure 2.9. *The trends of anthropogenic VOCs (AVOCs) and biogenic VOCs (BVOCs) emissions and corrected OMI HCHO columns over April–September in Chengdu during 2010–2020. The trends are normalized to a value of 1 in 2010.*

3.3.2. FNR and O_3 concentrations

Fig. 2.10 presents monthly averaged MDA8 O_3 concentrations plotted against OMI HCHO/NO_2 (FNR) for all environmental monitoring sites during 2013–2020. Following the method developed by (Jin et al., 2020), a third-order polynomial model is used to fit the data with a high correlation coefficient (R = 0.75), and the transitional regime is defined as the top 20% of the fitted curve. This model clearly captures the nonlinearities in O_3 chemistry with MDA8 O_3 concentration peaks at FNR = 2.75, and the FNR of transitional regime is ranging from 2.27 to 3.26. As NO_2 columns decreased over time, the ratio of HCHO to NO_2 columns continuously increased from 2014 to 2016, indicating that the extent of VOCs-limited regime gradually shrunk in Chengdu (Fig. 2.11). In terms of MDA8 O_3 concentrations, the urban and traffic sites present steady increasing trends (+13.2% a^{-1}) during 2013–2016, while a sharp decrease of O_3

concentration (–10.0% a^{-1}) was observed at rural site in 2016. Furthermore, we also found a strong urban-rural gradients of FNR in 2016, indicating that the metropolitan area of Chengdu remains VOCs-limited regime, while the rural area has shifted from VOCs-limited to transitional or NO_x-limited in 2016 (Fig. 2.12). Interestingly, the average O_3 concentration decreased by 14.0% from 2016 to 2017, and then rebounded in 2018. The reason for this drop could be inferred from the consistent decreasing trends of BVOC emissions and HCHO columns combined with the expansion of VOCs-limited regime in 2017, indicating that the reductions of BVOC emissions which are modulated by meteorological variability play a crucial role in the decrease of O_3 levels. After 2017, the anthropogenic NO_x and VOC emissions are jointly regulated, and the decreasing trends of NO_2 and HCHO columns are identified over 2018–2020. These emission regulations resulted in the decrease of O_3 concentrations at all monitoring sites from 2018 to 2019, while the O_3 levels were observed to slightly increase in 2020, which should be linked to the unfavorable meteorological conditions in 2020 (discussed in Section 3.4).

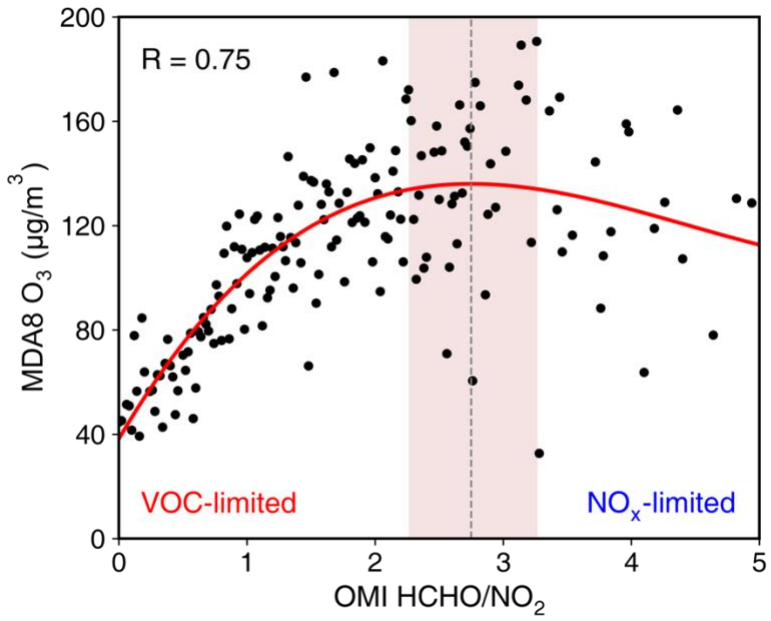

Figure 2.10. *Monthly averaged MDA8 O_3 concentrations are plotted against OMI HCHO/NO_2 for all environmental monitoring sites during 2013–2020. The solid lines are fitted third-order polynomial curve. The shaded area represents the range over the top 20% of the fitted curve (transitional regime).*

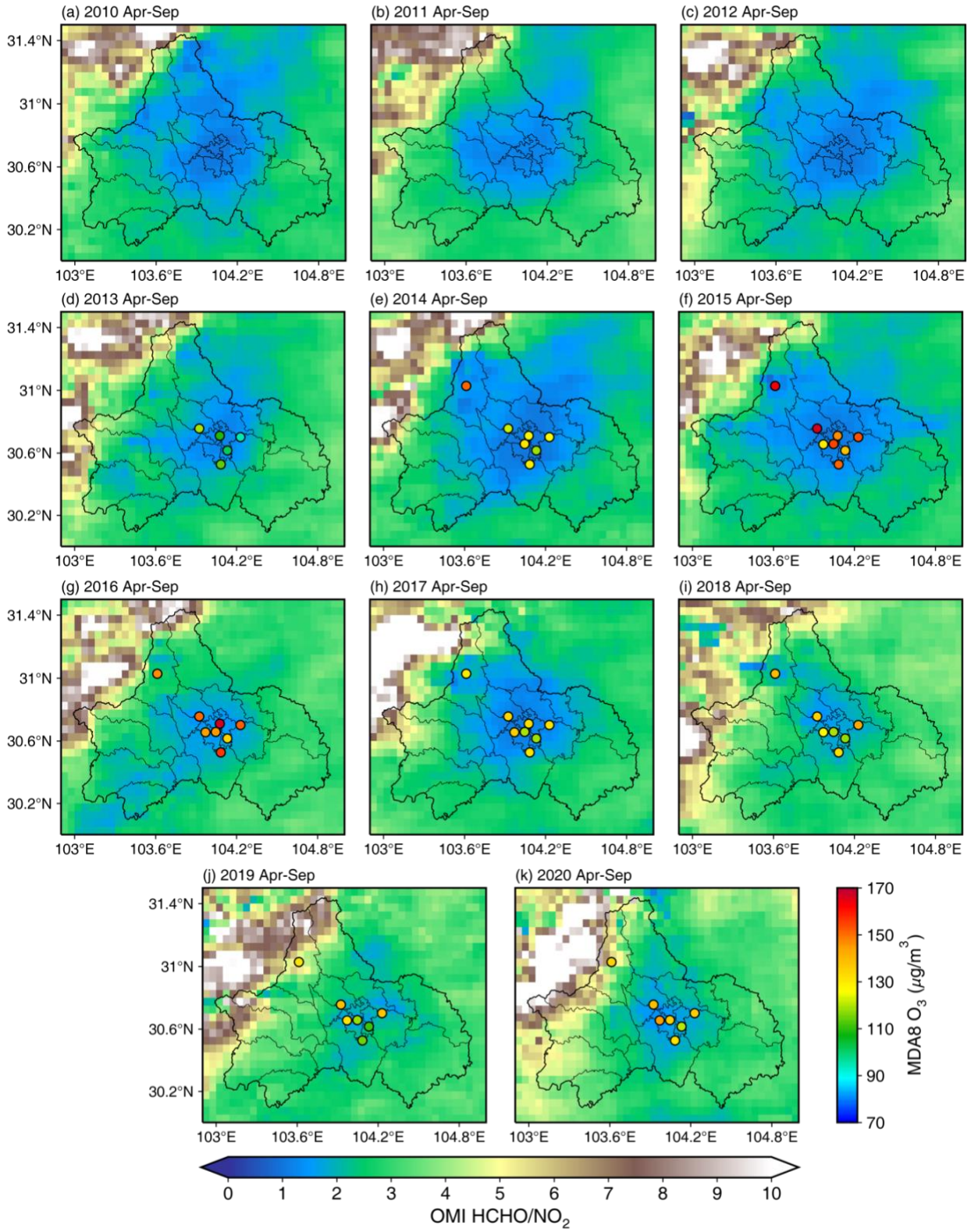

Figure 2.11. *Map of HCHO/NO_2 (FNR) and O_3 levels averaged over a 6-month period April–September from 2010–2020 over Chengdu.*

3.3.3. Trend of O_3-VOCs-NO_x sensitivity

Compared with the O_3-VOCs-NO_x sensitivity of Chengdu reported in previous studies (Table 2.1), our results are generally consistent with them. Before the implementation of emission controls, the extent of transitional and VOC-limited regime continuously extended due to the rapid increase of NO_x emissions from 2005, and most areas of Chengdu have been characterized as VOC-limited in 2013 (Jin and Holloway, 2015). During 2013–2020, we found the urban area remains at VOC-limited regime, which is further verified by existing evidence from field measurement and chemical transport models (CTMs). For instance, Tan et al. (2018) found the negative effect of NO_x reduction on O_3 control by conducting field measurements combined with a box model (OBM) in 2016. Based on the O_3 isopleth derived from the CMAQ model, Shen et al. (2021) reported that Chengdu city metropolitan area shows a NO_x-saturated O_3 regime, where the O_3 production was sensitive to VOC emissions in 2017. Han et al. (2020) also revealed that O_3 formation had negative sensitivity to NO_x over urban Chengdu in 2019. For suburban areas, Deng et al. (2019) carried out the field measurement at the central north suburb of Chengdu (Pixian district: black circle in Fig. 2.12b), and reported that the sampling site is under VOC-limited in 2016, while the north suburb of Chengdu (Pengzhou district: pentagram in Fig. 2.12b) is identified as transitional regime (Tan et al., 2018). The discrepancy between these two studies is linked to the elevated VOC emissions from local petroleum industry in Pengzhou. In particular, when compared to a recent study by Du et al. (2022), which also explored the spatial distribution of O_3-VOCs-NO_x sensitivity from June to September in 2019 over Chengdu by using the comprehensive air quality model with extensions (CAMx)-high-order decoupled direct method (HDDM). The O_3 formation sensitivity inferred by OMI $HCHO/NO_2$ is consistent with their results, both clearly present the shift of VOC-limited to transitional or NO_x-limited between urban and suburban areas.

These studies illustrate the complex variabilities of O_3-VOCs-NO_x sensitivity over the Chengdu city. Therefore, future work should consider using more comprehensive field measurements and numerical models to quantitatively identify the most effective reduction magnitude for jointly controlling of NO_x and VOC emissions to improve O_3 pollution over Chengdu.

Table 2.1. *Comparisons of previous O_3-VOCs-NO_x sensitivity over Chengdu.*

Area	Period	O3-VOCs-NOx sensitivity	Method	Reference
Urban	2005	transitional or NO_x-limited	FNR from OMI	Jin and Holloway (2015)
	Mar, 2010	transitional or VOC-limited	WRF-CALGRID	Xie et al. (2014)
	2013	transitional or VOC-limited	FNR from OMI	Jin and Holloway (2015)
	Sep, 2016	VOC-limited	box model (OBM)	Tan et al. (2018)
	Aug-Sep, 2017	VOC-limited	field measurement	Tan et al. (2020)
	2017	VOC-limited	CMAQ model	Shen et al. (2021)
	Apr-Aug, 2019	VOC-limited	OBM	Han et al. (2020)
	Jun-Sep, 2019	VOC-limited	CAMx-HDDM model	Du et al. (2022)
	2013-2020	VOC-limited	FNR and field measurement	This study
Suburban	Aug-Oct, 2016	VOC-limited	field measurement	Deng et al. (2019)
	Sep, 2016	transitional	OBM	Tan et al. (2018)
	Jun-Sep, 2019	transitional or NO_x-limited	CAMx-HDDM model	Du et al. (2022)
Rural	2013-2015	VOC-limited	FNR and field measurement	This study
	2016-2020	transitional or NO_x-limited	FNR and field measurement	This study

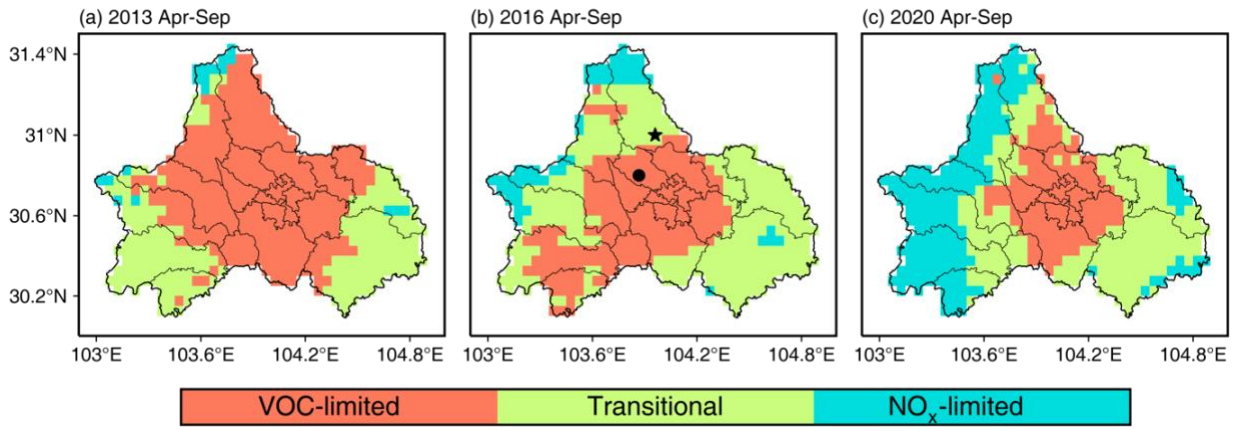

Figure 2.12. *O_3-VOCs-NO_x sensitivity inferred by OMI HCHO/NO_2 over a 6-month period April–September in 2013, 2016 and 2020 in Chengdu. In 2016, the black circle site is reported in VOC-limited regime Deng et al. (2019), while the pentagram is in transitional regime Tan et al. (2018).*

3.4. Relationship between O_3 variability and meteorological conditions

Heatwaves (HWs) and stagnant events are the most critical meteorological phenomenon that governs variations in O_3 levels (Yang and Shao, 2021). Thus, we further investigate the occurrence frequencies of HWs and stagnation derived from the WRF model, as well as their co-occurrence over 2013–2020. There is a high probability of HWs occurrence in summer, with peak frequency in July. The similar feature was also found in the earlier work by Huang et al. (2021) for SCB. In terms of the air stagnation, our result shows relatively less occurrence in July and August, which could be attributed to the frequent rainfalls over the SCB in summer (Qian et al., 2015). Over the warm season, the co-occurrence frequencies of stagnant conditions and HWs ranging from 1.2% to 4.6% for the whole city during 2013–2020, and Chengdu is most susceptible to HWs and stagnant in 2019 and 2020, with co-occurrence frequencies higher than 8.0% at the metropolitan area, indicating that the HWs and stagnant conditions might become more frequent under the changing climate.

By comparing the trends of extreme meteorological events and O_3 levels, we find a high degree of correlation between monthly O_3 variations and the occurrence of HWs and stagnation over Chengdu. Fig. 2.13 depicts several periods that abovementioned meteorological phenomenon could well explain anomalous high or low O_3 levels over time. Specifically, enhanced rural O_3 levels in July 2015 are closely associated with frequent stagnations over rural areas (frequency in excess of 30%). Similarly, elevated O_3 levels in June and August in 2016 are clearly linked to profound HWs (frequency higher than 30%) occurrence during the period which triggered intense photochemical reactions. Furthermore, severe O_3 pollution in August 2019 is largely determined by the co-occurrence of stagnant conditions and HWs (Fig. 2.13f). It is worth noting that the most prominent period that O_3 was affected by meteorological fields is May 2020. Fig. B3 presents the changes of simulated daytime 2-m temperature and precipitation in May 2020 relative to May 2019. The temperature increase (more than 4℃) was also coincident with a sharp drop in precipitation (up to 60 mm or 35% reduction) over Chengdu in May 2020 compared with May 2019, while anthropogenic emissions of NO_x and VOCs reduced by 11.3% and 6.3% in Chengdu due to Covid-19 lockdown, respectively. Such a strong warming magnitude combined with droughty condition caused Chengdu endures profound heatwaves and air stagnations in May 2020, subsequently leading to numerous O_3 exceedances (as reflected by the spike in O_3 levels). This opposed phenomenon demonstrates the considerable contribution of persistent unfavorable meteorological fields on elevating O_3 concentrations which could even fully offset the effects of emission reductions. This is in agreement with Sun et al. (2021) and Wu et al. (2022), who use chemical transport models to quantitively identify the role of unprecedented meteorological phenomenon on high levels of O_3 in May 2020.

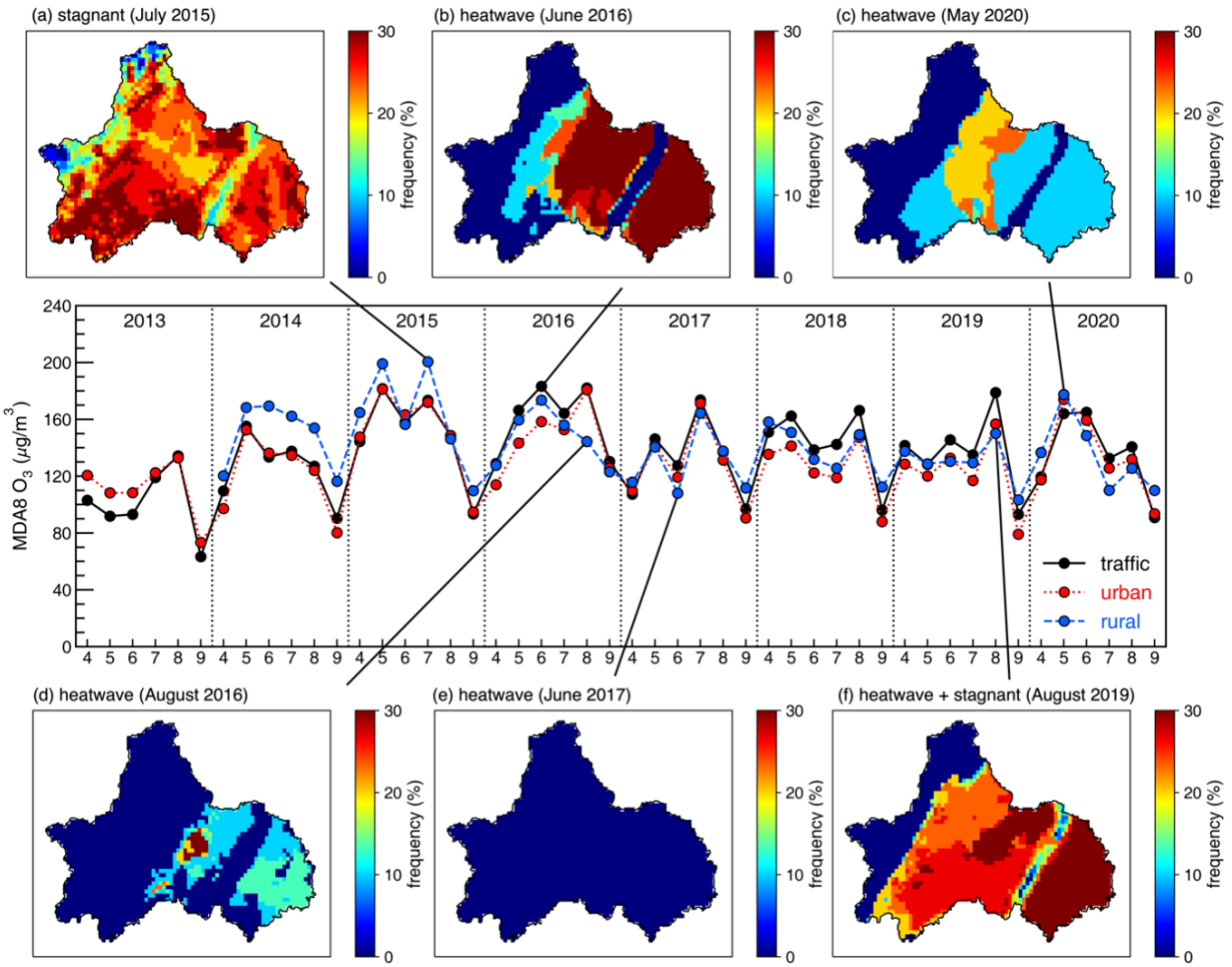

Figure 2.13. *(Middle panel) Monthly average concentration of MDA8 O_3 for traffic, urban and rural stations for April–September from 2013–2020, and occurrence frequency maps of heatwave and stagnant of extreme meteorological events over Chengdu.*

4. Conclusions

Long-term O_3 and precursor observations from 2013 to 2020 in Chengdu, a megacity located in southwestern China, have provided insight into the changes of ambient O_3 and precursors levels in response to regulation efforts. We depicted deteriorated O_3 trends (+14.0% a^{-1}) at urban and traffic sites during 2013–2016 followed by a weak reduction with notable interannual variability afterwards. In contrast, O_3 concentration at rural areas generally shows a downward trend (–2.9% a^{-1}) during 2014–2020. Further analysis based on MEIC inventory (–3.7% a^{-1}) and OMI NO_2

columns (–4.5% a^{-1}) reported strong evidence on the continuous reductions in NO_x emission from 2013 to 2020. However, OMI HCHO columns exhibit a weaker declining trend over time, with the most notable decrease in 2018–2020 (–6.0% a^{-1}), implying the effectiveness of targeted legislature concerning VOC emissions in Chengdu. Noticing the discrepancies between the trends of NO_x and VOC emissions, which could lead to dramatic changes in O_3-VOCs-NO_x sensitivity, we further analyze the relationship between FNR and field measurements to probe the transition of O_3-VOCs-NO_x sensitivity over Chengdu. The results indicate that metropolitan Chengdu remains VOCs-limited regime during 2013–2020, while the rural area has shifted from VOCs-limited to transitional or NO_x-limited regime since 2016. Given the well-supported identification of O_3-VOCs-NO_x sensitivity, it is expected that the emission regulation framework involves joint control of NO_x and VOC emissions would lead to evident O_3 improvements in near future. Nevertheless, the variabilities of meteorological phenomenon and biogenic emissions should not be neglected, as modeling results indicate that extreme unfavorable meteorological conditions accompanied by enhanced BVOC emissions in a short period (May 2020) could even fully offset O_3 benefits over warm season. Thus, the potential perturbation induced by meteorological phenomenon and BVOC emissions under warming climate deserves further study for ensuring the effectiveness of O_3 abatement strategy not overestimated.

Recent studies have noted the steady reductions of NO_x emissions from 2013 throughout China attributed to regulation efforts introduced by APPCAP, but changes in anthropogenic VOCs emissions remain uncertain, particularly in highly urbanized megacities. Our analysis provides robust evidence derived from both emission inventory and satellite data which points to the success in reducing NO_x emissions since 2013 and cutting VOCs emissions after 2017 in Chengdu. However, the response of ambient O_3 levels is relatively weak due to the gradual transition of O_3-

VOCs-NO_x regime and increased emissions of biogenic precursors under a warming climate. Furthermore, the projected expansion in urban green spaces attributed to the implementation of urban greening strategies could result in substantial BVOC emissions in urban areas, thus posing challenges to O_3 regulation (Gu et al., 2021). While meteorological phenomena and enhanced BVOC emissions likely obscured the expected decline in O_3 concentrations, ongoing control strategies involving joint regulation of NO_x and VOCs would be increasingly effective in controlling O_3 pollution in Chengdu. This work may also be compelling to megacities in East Asia where anthropogenic emissions undergo similar pathways as Chengdu. Although the abundance of precursor emissions may differ slightly among megacities, this work provides an improved scientific basis for diagnosing O_3 variability and associated driving factors over time, thus showing important implications in developing reliable emission control strategies toward compliance of O_3 air quality standards.

Supporting Information B

Text B1. Planetary boundary-layer schemes in WRF models.

In the WRFv3.9.1 model, the planetary boundary-layer schemes are used to depict the unresolved turbulent vertical fluxes of momentum, heat, and other parameters including moisture, wind field, etc. in the boundary layer as well as the entire atmosphere (Hu et al., 2010), which play an essential role in simulating the meteorological conditions and the structures of the PBL, especially for our study region where is characterized by a complex basin landform near the Tibetan Plateau. There are two types (local and non-local) of closure schemes were used to estimate the turbulent fluxes from mean quantities. For the local closure schemes, the fluxes are only dependent on the variables of vertical layers symmetrically adjacent to a specific simulated

cell, while the non-local closure schemes also consider the non-local effects of multiple vertical levels by introducing a non-local term (Noh et al., 2003) or treated explicitly (Pleim and Chang, 1992). In addition, the PBL height is calculated as the layer where the bulk Richardson number (Ri_b) exceeds a certain threshold for non-local closure schemes, while the local closure schemes identify the PBL height as the level where the turbulent kinetic energy (TKE) profile decreases to the threshold values. The bulk Richardson number (Ri_b) is a dimensionless number that describes the ratio of buoyancy term to the flow shear term, which is defined by equation (B1), where g is the gravity, $\theta_v(z)$ is the virtual potential temperature at height z, θ_s is the potential temperature near the surface, θ_{va} is the virtual potential temperature at the lowest level and $U(z)$ is the horizontal wind speed at height z. In addition, the boundary layer height is determined by equation (B2), where Ri_{bcr} is the critical bulk Richardson number. In this study, three different PBL parameterizations including two non-local (YSU, ACM2), and one local (MYJ) closure schemes were adopted, with their associated surface layer schemes to evaluate the sensitivity of the model to different schemes in simulating the atmospheric parameters in the boundary layer.

$$Ri_b(z) = \frac{g[\theta_v(z) - \theta_s]z}{\theta_{va}U(z)^2} \qquad \text{(B1)}$$

$$h = Ri_{bcr}\frac{\theta_{va}U(h)^2}{g[\theta_v(h) - \theta_s]} \qquad \text{(B2)}$$

the Yonsei University (YSU) PBL scheme (Hong et al., 2006) is a first-order non-local scheme. Based on the Medium Range Forecast (MRF) scheme, an explicit treatment of entrainment processes at the top of the PBL is introduced in the YSU PBL. The PBL height is calculated as the lowest level, located above a certain pre-determined minimum height, at which the bulk Richardson number (Ri_b) exceeds a certain threshold (Ri_{bcr}). In the WRFv3.9.1 model, the YSU

scheme is modified by increasing the Ri_b from 0 to 0.25 over land to enhance mixing in the stable boundary layer.

The ACM2 PBL scheme (Pleim, 2007) is a first-order non-local scheme, which is a modified version of the original asymmetrical convective model (ACM1; Pleim and Chang, 1992) that adds an eddy diffusion component to the nonlocal transport to improve the shape of vertical profiles, especially the gradually decreasing gradient near the surface. In the ACM2 PBL scheme, the PBL height is defined as the layer at which Ri_b exceeds a threshold of 0.25. It should be noted that the ACM2 PBL scheme uses local closure for stable conditions and non-local closure for unstable conditions.

The Mellor-Yamada-Janjic (MYJ) scheme (Janjić, 2002) is a 1.5 order prognostic TKE scheme with local formulation to determine the eddy diffusion coefficients and the vertical mixing. The PBL height in the MYJ scheme is determined as the layer where the TKE profile decreases to the value of 0.2 $m^2\ s^{-2}$. This scheme is generally appropriate for all stable and slightly unstable flows. The details of YSU, ACM2, and MYJ schemes as well as their associated surface layer schemes are presented in Table B1.

Table B1. *The PBL schemes of the WRF model.*

PBL schemes	Closure order	Surface layer schemes	Method	Threshold
YSU	1.0 non-local	Monin-Obukhov	Richardson number	0.0/0.25
ACM2	1.0 non-local	Monin-Obukhov	Richardson number	0.25
MYJ	1.5 local	Eta similarity	TKE	0.2 $m^2\ s^{-2}$

Text B2. Evaluation of surface meteorological conditions and vertical PBL structure simulated by WRF model with different PBL schemes.

To explore the most suitable PBL scheme for the WRF simulations over Chengdu, three sensitivity modeling tests coupled with YSU, ACM2, and MYJ scheme respectively are conducted

during August 2019 with the 3 days before this month is treated as spin-up time. Other selected WRF configuration options used in this study are shown in Table B2. The meteorological parameters including temperature at 2 m (T2), relative humidity at 2 m (RH2), wind speed at 10 m (WS10), and wind direction at 10 m (WD10), which are simulated by the WRF model are evaluated against the observations of meteorological sites over Chengdu. The statistical evaluation metrics include mean bias (MB), root mean square error (RMSE), and index of agreement (IOA). Their calculations are defined by equations (B3) – (B5), respectively. P_i and O_i denote the model simulated values and observation values, respectively, and N represents the number of samples.

Table B2. *The selected configuration of WRF physical parameterization schemes.*

Physical process	Parameterization scheme
Microphysics	Lin scheme (Lin et al., 1983)
Longwave Radiation	RRTMG scheme (Mlawer et al., 1997)
Shortwave Radiation	Goddard scheme (Chou and Suarez, 1999)
Cumulus Parameterization	Grell 3-D scheme (Grell and Dévényi, 2002)
Land Surface	Noah land surface model scheme (Chen and Dudhia, 2001)

$$MB = \frac{1}{N}\sum_{i=1}^{N}(P_i - O_i) \tag{B3}$$

$$RMSE = \left[\frac{1}{N}\sum_{i=1}^{N}(P_i - O_i)^2\right]^{\frac{1}{2}} \tag{B4}$$

$$IOA = 1 - \frac{\sum_{i=1}^{N}(P_i - O_i)^2}{\sum_{i=1}^{N}\left(|P_i - \overline{O}| + |O_i - \overline{O}|\right)^2} \tag{B5}$$

Fig. B1 presents the comparison of simulated meteorological parameters and surface observations. In addition, the statistical evaluations of simulated meteorological parameters over Chengdu are shown in Table B3. The simulated T2 is in good agreement with observations for all

PBL schemes with slightly overestimated (0.67–1.23°C, especially during the nighttime) and the IOA values are ranging from 0.90–0.92. The simulation with the ACM2 PBL scheme (MB = 0.67, RMSE = 2.13, IOA = 0.92) gives less bias than with the MYJ and YSU scheme, which might be attributed to the best performance in simulating the cloud cover and incoming solar radiation. In addition, by adjusting the value of f_{conv}, the ACM2 scheme can diminish the non-local effects during stable conditions, while the YSU scheme would overestimate the T2 due to its excessive turbulent mixing effect.

In terms of relative humidity, the simulated RH2 has been underestimated with IOA values higher than 0.80 with each PBL scheme. Specifically, the simulated values of the non-local schemes (ACM2 and YSU) are lower. This is mainly due to the fact that the non-local schemes considered the non-local transport and the entrainment process that transports water vapor from the surface to the upper layers, resulting in a lower simulated relative humidity than the ACM2 with slightly higher errors. However, the correlations between simulated RH2 and observations for ACM2 (IOA = 0.83) and YSU schemes (IOA = 0.81) are higher than the MYJ scheme (IOA = 0.80).

For the simulations of the wind field, all WRF PBL schemes have overestimated the 10m wind speed, ranging from 0.47 to 0.81 m/s. The best performances belong to non-local schemes, in particular YSU (MB = 0.47, RMSE = 1.68, IOA = 0.42), followed by ACM2 (MB = 0.48, RMSE = 1.72, IOA = 0.40). The overestimation of simulated wind speed has been reported in existing studies (Hariprasad et al., 2014), which could be linked to the challenge of simulating the sub-grid surface roughness and the related induced turbulence in the lower layers (Jiménez and Dudhia, 2012). The performances of simulating wind directions are in agreement with wind speed, with the non-local schemes being superior to the local scheme.

Overall, the ACM2 scheme presents less bias than the YSU and MYJ schemes in simulating the surface temperature and relative humidity, while the YSU is the scheme with the best performance in representing the wind field near the surface, indicating that the performances of the WRF model coupled with non-local schemes (YSU and ACM2) are more accurate than with the local scheme (MYJ) in simulating the surface meteorological conditions. The reason for this phenomenon is that the non-local schemes considered the effects of larger eddies on the dispersion of heat, moisture, and momentum throughout the PBL depth, so they are able to simulate the diurnal-driven turbulence associated with the surface heating (Avolio et al., 2017).

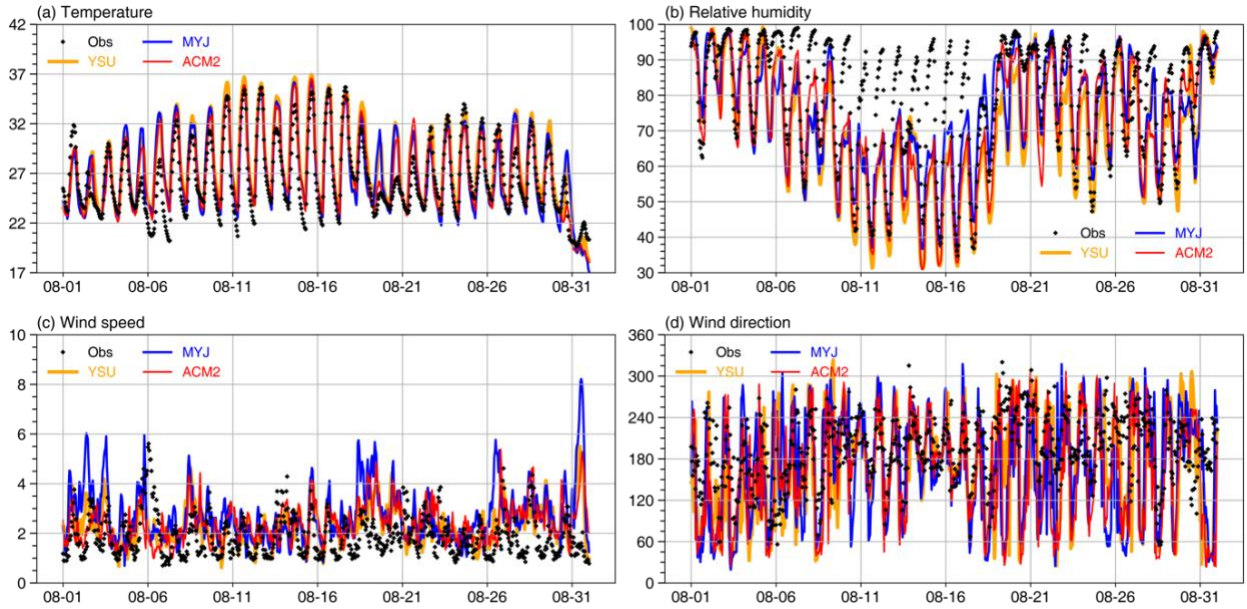

Figure B1. *Comparison of simulated 2-m temperature (T2), 2-m relative humidity (RH2), 10-m wind speed (WS10), and 10-m wind direction (WD10) with observations.*

Table B3. *Evaluation of meteorological parameters simulated by the WRF model with different PBL schemes.*

	PBL schemes	Sample (N)	Mean Obs.	Mean Sim.	MB	RMSE	IOA
T2	YSU	10422	26.50	27.73	1.23	2.47	0.90
(°C)	MYJ	10422	26.50	27.18	0.68	2.44	0.90
	ACM2	10422	26.50	27.17	0.67	2.13	0.92

RH2	YSU	10422	79.83	70.08	-9.75	16.20	0.81
(%)	MYJ	10422	79.83	74.47	-5.36	15.08	0.80
	ACM2	10422	79.83	72.50	-7.33	14.78	0.83
WS10	YSU	9931	1.90	2.37	0.47	1.68	0.42
(m/s)	MYJ	9931	1.90	2.71	0.81	2.05	0.38
	ACM2	9931	1.90	2.38	0.48	1.72	0.40
WD10	YSU	9931	192.62	167.02	-25.60	153.35	0.53
(°)	MYJ	9931	192.62	167.05	-25.57	156.97	0.51
	ACM2	9931	192.62	159.37	-33.25	154.46	0.52

The monthly-averaged vertical profiles of simulated and observed temperature (T), dewpoint temperature (Td), and wind speed (WS) at 08:00 LST and 20:00 LST corresponding to morning and evening, respectively for the Wenjiang radiosonde station (location is shown in Fig. 1b) are presented in Fig. B2. Furthermore, the evaluations of simulated vertical profiles of these meteorological parameters are shown in Table B4. The temperature profiles indicate slight overestimations in the temperature near the surface, and both the local and non-local PBL schemes perfectly simulated the stable layer below 200m with temperature inversion reaching 1K/100m at 08:00 LST. It is worth noting that the nonlocal transport is shut down in ACM2 and vertical mixing is purely due to local eddy diffusion as in MYJ for stable conditions at 08:00 LST. As a result, the temperature profiles simulated by MYJ and ACM2 schemes have similar patterns at 08:00 LST and both are closer to observed temperatures near the surface. However, the YSU scheme has a stronger downward thermal flux and upward moisture flux in the lower atmosphere (Hong and Kim, 2008) by increasing the critical bulk Richardson number, which has led to a warmer and drier PBL at both 08:00 LST and 20:00 LST near the surface. This phenomenon has been further verified by the dewpoint temperature profiles, with lower Td for the YSU scheme.

Regarding the vertical profile of the wind field, the wind speed is also underestimated by the WRF model, especially at 20:00 LST with higher wind speed, which is linked to the difficulties in simulating the wind field at complex mountain-basin terrain, as well as the small innermost domain of the simulations. Interestingly, the MYJ scheme simulates even higher wind speed than observations near the ground (0 – 200m) at 08:00 LST, which leads to the wind speed simulated by MYJ scheme (RMSE = 5.50, IOA = 0.33) has larger bias than ACM2 (RMSE = 4.92, IOA = 0.36) and YSU (RMSE = 4.92, IOA = 0.40) scheme. The similar feature was also found in the earlier work by Hu et al. (2010).

The statistical evaluation shows that the non-local schemes (ACM2 and YSU) perform better than the local scheme (MYJ) in representing parameters in the boundary layer, which highlights the importance of considering the non-local effects in simulating the vertical structures of PBL, especially under unstable conditions. However, the explicit treatment of entrainment processes in the YSU scheme could result in stronger downward thermal flux and upward moisture flux with a slightly higher bias in predicting the temperature and dew point temperature profiles near the surface. Overall, the ACM scheme has the best performance in simulating the vertical profiles of meteorological conditions near the ground, while the YSU scheme performs more accurately in representing the vertical profiles over the PBL.

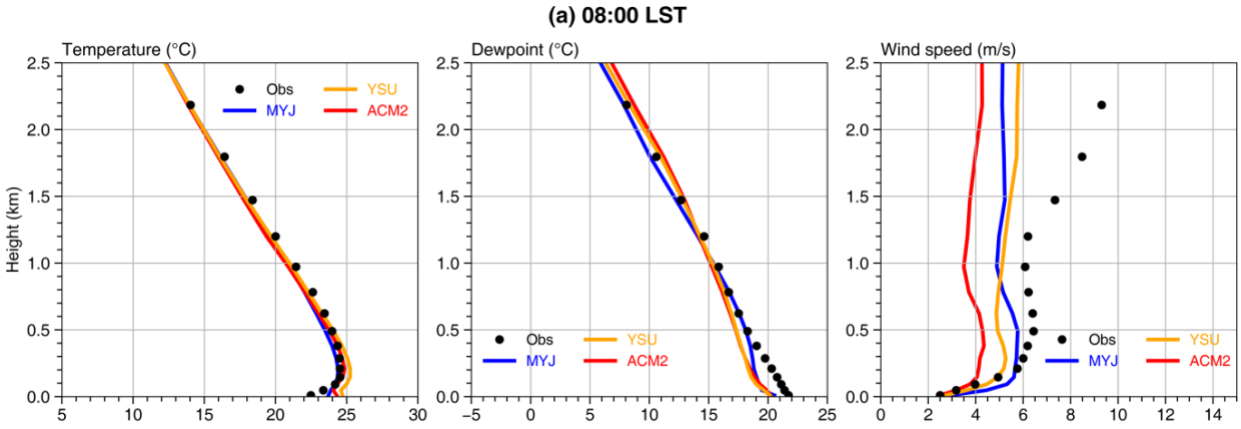

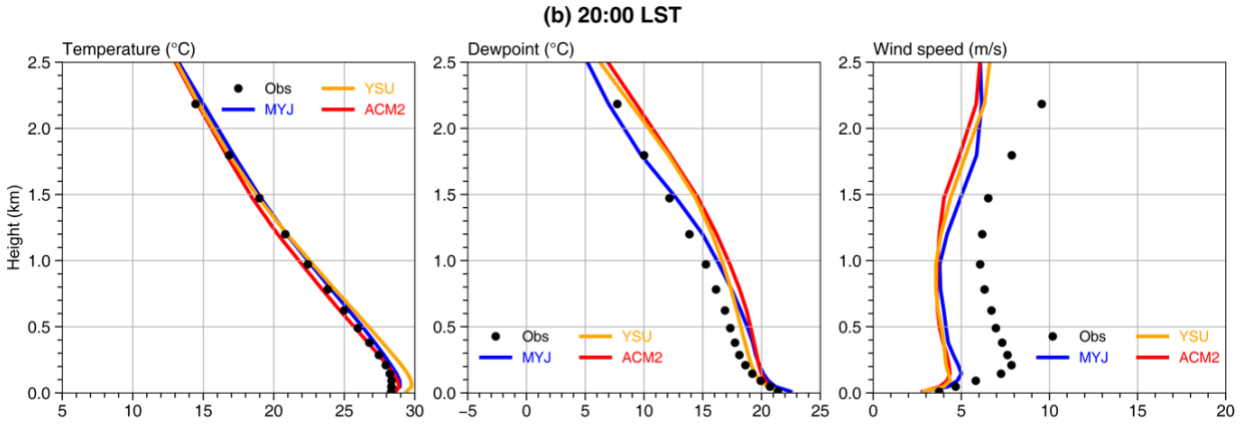

Figure B2. *Comparison of the simulated vertical profile of temperature (T), dewpoint temperature (Td), and wind speed (WS) with radiosonde measurements at (a) 08:00 LST and (b) 20:00 LST.*

Table B4. *Evaluation of vertical profile of meteorological parameters simulated by the WRF model with different PBL schemes.*

	Time	PBL schemes	MB	RMSE	IOA
T	08:00 LST	YSU	0.31	1.78	0.95
(°C)	08:00 LST	MYJ	-0.14	1.75	0.95
	08:00 LST	ACM2	0.00	1.76	0.95
	20:00 LST	YSU	0.72	1.54	0.97
	20:00 LST	MYJ	0.35	1.60	0.97
	20:00 LST	ACM2	-0.03	1.41	0.97
Td	08:00 LST	YSU	-0.95	2.78	0.90
(°C)	08:00 LST	MYJ	-0.82	2.93	0.89
	08:00 LST	ACM2	-0.84	2.62	0.91
	20:00 LST	YSU	0.88	2.98	0.89
	20:00 LST	MYJ	0.76	3.30	0.89
	20:00 LST	ACM2	1.38	2.93	0.88
WS	08:00 LST	YSU	-1.25	4.92	0.40
(m/s)	08:00 LST	MYJ	-1.05	5.50	0.33
	08:00 LST	ACM2	-2.35	4.92	0.36
	20:00 LST	YSU	-2.59	4.29	0.37

20:00 LST	MYJ	-2.31	4.32	0.39
20:00 LST	ACM2	-2.71	4.49	0.41

Text B3. Evaluation of meteorological parameters simulated by WRF model for April–September during 2010–2020.

Table B5 presents the statistical evaluation of simulated meteorological parameters over Chengdu from 2010 to 2020. The simulated T2 are in good agreement with observations, with slightly overestimated and IOA values higher than 0.85, while the RH2 has been underestimated with IOA values higher than 0.74 in each year. Although the WS10 over Chengdu was also overestimated by the WRF model, which might be attributed to the bias in atmospheric dynamics induced by planetary boundary layer (PBL) scheme, the simulations of wind fields are still achieved good performance with IOA values range from 0.43-0.53 and 0.49-0.53 for WS10 and WD10, respectively during 2010-2020.

Table B5. *Evaluation of meteorological parameters simulated by the WRF model over Chengdu from 2010 to 2020.*

	Year	Sample (N)	Mean Obs.	Mean Sim.	MB	RMSE	IOA
T2	2010	57616	22.15	24.17	1.95	3.43	0.90
(℃)	2011	60949	23.07	25.22	2.16	3.79	0.88
	2012	61017	22.91	24.35	1.43	3.00	0.89
	2013	61323	23.43	25.34	1.91	3.33	0.89
	2014	61027	22.89	25.05	2.18	3.39	0.85
	2015	59616	23.21	24.52	1.32	2.99	0.90
	2016	60978	23.40	24.77	1.35	3.00	0.90
	2017	59016	23.33	24.90	1.45	3.00	0.90
	2018	61351	23.53	24.94	1.40	3.00	0.89
	2019	61311	22.87	24.91	2.05	3.28	0.88
	2020	61358	23.04	24.92	1.89	3.27	0.91

RH2	2010	57680	79.26	71.53	-7.57	17.03	0.74
(%)	2011	61040	73.04	64.39	-8.62	19.39	0.75
	2012	61038	74.43	71.94	-2.57	15.25	0.81
	2013	61324	72.97	69.11	-3.86	15.35	0.82
	2014	61025	73.91	69.07	-4.70	15.83	0.79
	2015	59613	72.41	68.33	-4.21	16.65	0.80
	2016	60977	79.98	71.10	-8.86	17.24	0.77
	2017	59015	78.56	68.38	-9.90	19.32	0.75
	2018	61348	79.69	70.28	-9.41	18.19	0.78
	2019	61312	81.53	69.09	-12.44	19.13	0.75
	2020	61360	76.85	67.69	-9.15	18.72	0.79
WS10	2010	56769	1.21	2.83	1.61	2.33	0.46
(m/s)	2011	60029	1.28	2.83	1.56	2.38	0.47
	2012	53089	1.31	2.73	1.47	2.21	0.44
	2013	52692	1.38	2.88	1.57	2.36	0.45
	2014	53042	1.31	2.76	1.49	2.22	0.43
	2015	52777	1.50	2.77	1.32	2.24	0.45
	2016	58623	1.88	2.73	0.88	2.00	0.50
	2017	52360	1.93	2.85	0.95	2.05	0.50
	2018	58242	1.95	2.89	0.97	2.07	0.50
	2019	58438	1.89	2.65	0.77	1.88	0.52
	2020	59443	1.96	2.85	0.90	2.00	0.53
WD10	2010	56769	177.37	147.17	-30.11	157.80	0.50
(°)	2011	60029	176.58	154.34	-22.22	152.48	0.51
	2012	53089	176.13	152.14	-27.29	154.33	0.51
	2013	52692	173.37	149.67	-27.36	156.26	0.50
	2014	53042	181.70	155.79	-29.05	154.36	0.49
	2015	52777	178.37	151.34	-29.58	149.01	0.51
	2016	58623	175.34	155.35	-21.61	152.36	0.50
	2017	52360	182.01	155.02	-28.33	155.06	0.51
	2018	58242	176.60	150.95	-27.53	156.39	0.51

2019	58438	179.39	161.91	-19.04	152.38	0.52
2020	59443	184.28	155.77	-29.65	153.53	0.53

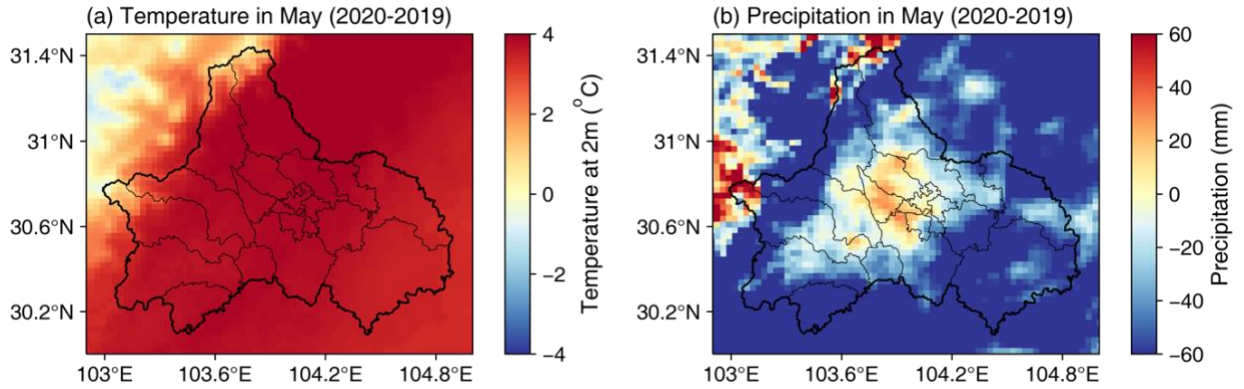

Figure B3. *The changes of simulated temperature at 2 m in the daytime* ***(a)*** *and precipitation* ***(b)*** *in May 2020 relative to May 2019 over April-September in Chengdu.*

Data Availability

All surface measurements, satellite, reanalysis, and wildfire datasets used in this study are publicly available. MODIS land cover type data are available at https://doi.org/10.5067/MODIS/MCD12Q1.006. Surface NO_2 concentrations are downloaded from the CARB (www.arb.ca.gov/aqmis2/aqmis2.php). OMI NO_2 columns are derived from QA4ECV (www.qa4ecv.eu), NASA (https://doi.org/10.5067/Aura/OMI/DATA2017), and BEHR (http://behr.cchem.berkeley.edu) retrievals. The TROPOMI NO_2 columns are downloaded from NASA GES DISC (disc.gsfc.nasa.gov). The monthly climate data are extracted from PRISM (prism.oregonstate.edu) and NARR (psl.noaa.gov/data/gridded/data.narr.html). The ERA5 and ERA5-Land hourly reanalysis data are available from the Copernicus Climate Service (C3S) Climate Data Store (climate.copernicus.eu). The wildfire records are obtained from FRAP (frap.fire.ca.gov/frap-projects/fire-perimeters/). The hourly observations of air pollutants over Chengdu were collected from the China National Environmental Monitoring Center (http://www.cnemc.cn/). Meteorological observations in Chengdu are provided by the China Meteorological Data Service Center (CMDSC, http://data.cma.cn/) and Sichuan Provincial Weather Service. The anthropogenic

emissions in China are derived from the Multi-resolution Emission Inventory of China (MEIC, http://meicmodel.org/) developed by Tsinghua University.

References

Abatzoglou, J.T., Williams, A.P., 2016. Impact of anthropogenic climate change on wildfire across western US forests. Proc. Natl. Acad. Sci. U.S.A. 113, 11770–11775. https://doi.org/10.1073/pnas.1607171113

Almaraz, M., Bai, E., Wang, C., Trousdell, J., Conley, S., Faloona, I., Houlton, B.Z., 2018. Agriculture is a major source of NOx pollution in California. Sci. Adv. 4, eaao3477. https://doi.org/10.1126/sciadv.aao3477

Avolio, E., Federico, S., Miglietta, M.M., Lo Feudo, T., Calidonna, C.R., Sempreviva, A.M., 2017. Sensitivity analysis of WRF model PBL schemes in simulating boundary-layer variables in southern Italy: An experimental campaign. Atmospheric Research 192, 58–71. https://doi.org/10.1016/j.atmosres.2017.04.003

Bauwens, M., Verreyken, B., Stavrakou, T., Müller, J.-F., Smedt, I.D., 2022. Spaceborne evidence for significant anthropogenic VOC trends in Asian cities over 2005–2019. Environ. Res. Lett. 17, 015008. https://doi.org/10.1088/1748-9326/ac46eb

Beirle, S., Boersma, K.F., Platt, U., Lawrence, M.G., Wagner, T., 2011. Megacity Emissions and Lifetimes of Nitrogen Oxides Probed from Space. Science 333, 1737–1739. https://doi.org/10.1126/science.1207824

Boersma, K.F., Eskes, H., Richter, A., De Smedt, I., Lorente, A., Beirle, S., Van Geffen, J., Peters, E., Van Roozendael, M., Wagner, T., 2017. QA4ECV NO2 tropospheric and stratospheric column data from OMI. https://doi.org/10.21944/QA4ECV-NO2-OMI-V1.1

Boersma, K.F., Eskes, H.J., Richter, A., De Smedt, I., Lorente, A., Beirle, S., van Geffen, J.H.G.M., Zara, M., Peters, E., Van Roozendael, M., Wagner, T., Maasakkers, J.D., van der A, R.J., Nightingale, J., De Rudder, A., Irie, H., Pinardi, G., Lambert, J.-C., Compernolle, S.C., 2018. Improving algorithms and uncertainty estimates for satellite NO2 retrievals: results from the quality assurance for the essential climate variables (QA4ECV) project. Atmos. Meas. Tech. 11, 6651–6678. https://doi.org/10.5194/amt-11-6651-2018

Bovensmann, H., Burrows, J.P., Buchwitz, M., Frerick, J., Noël, S., Rozanov, V.V., Chance, K.V., Goede, A.P.H., 1999. SCIAMACHY: Mission Objectives and Measurement Modes. J. Atmos. Sci. 56, 127–150. https://doi.org/10.1175/1520-0469(1999)056<0127:SMOAMM>2.0.CO;2

Burley, J.D., Bytnerowicz, A., Buhler, M., Zielinska, B., Schweizer, D., Cisneros, R., Schilling, S., Varela, J.C., McDaniel, M., Horn, M., Dulen, D., 2016. Air Quality at Devils Postpile National Monument, Sierra Nevada Mountains, California, USA. Aerosol Air Qual. Res. 16, 2315–2332. https://doi.org/10.4209/aaqr.2016.02.0069

Burrows, J.P., Weber, M., Buchwitz, M., Rozanov, V., Ladstätter-Weißenmayer, A., Richter, A., DeBeek, R., Hoogen, R., Bramstedt, K., Eichmann, K.-U., Eisinger, M., Perner, D., 1999. The Global Ozone Monitoring Experiment (GOME): Mission Concept and First Scientific Results. J. Atmos. Sci. 56, 151–175. https://doi.org/10.1175/1520-0469(1999)056<0151:TGOMEG>2.0.CO;2

Buysse, C.E., Munyan, J.A., Bailey, C.A., Kotsakis, A., Sagona, J.A., Esperanza, A., Pusede, S.E., 2018. On the effect of upwind emission controls on ozone in Sequoia National Park. Atmos. Chem. Phys. 18, 17061–17076. https://doi.org/10.5194/acp-18-17061-2018

Byrnes, D.K., Van Meter, K.J., Basu, N.B., 2020. Long-Term Shifts in U.S. Nitrogen Sources and Sinks Revealed by the New TREND-Nitrogen Data Set (1930–2017). Global Biogeochemical Cycles 34. https://doi.org/10.1029/2020GB006626

Caiazzo, F., Ashok, A., Waitz, I.A., Yim, S.H.L., Barrett, S.R.H., 2013. Air pollution and early deaths in the United States. Part I: Quantifying the impact of major sectors in 2005. Atmospheric Environment 79, 198–208. https://doi.org/10.1016/j.atmosenv.2013.05.081

Callies, J., Corpaccioli, E., Eisinger, M., Hahne, A., Lefebvre, A., 2000. GOME-2-Metop's second-generation sensor for operational ozone monitoring. ESA Bull. 102, 28–36.

Campbell, P.C., Tong, D., Saylor, R., Li, Y., Ma, S., Zhang, X., Kondragunta, S., Li, F., 2022. Pronounced increases in nitrogen emissions and deposition due to the historic 2020 wildfires in the western U.S. Science of The Total Environment 839, 156130. https://doi.org/10.1016/j.scitotenv.2022.156130

Chen, F., Dudhia, J., 2001. Coupling an Advanced Land Surface–Hydrology Model with the Penn State–NCAR MM5 Modeling System. Part I: Model Implementation and

Sensitivity. Monthly Weather Review 129, 569–585. https://doi.org/10.1175/1520-0493(2001)129<0569:CAALSH>2.0.CO;2

Chou, M.-D., Suarez, M.J., 1999. A solar radiation parameterization for atmospheric studies. National Aeronautics and Space Administration, Goddard Space Flight Center.

Cohen, A.J., Brauer, M., Burnett, R., Anderson, H.R., Frostad, J., Estep, K., Balakrishnan, K., Brunekreef, B., Dandona, L., Dandona, R., Feigin, V., Freedman, G., Hubbell, B., Jobling, A., Kan, H., Knibbs, L., Liu, Y., Martin, R., Morawska, L., Pope, C.A., Shin, H., Straif, K., Shaddick, G., Thomas, M., van Dingenen, R., van Donkelaar, A., Vos, T., Murray, C.J.L., Forouzanfar, M.H., 2017. Estimates and 25-year trends of the global burden of disease attributable to ambient air pollution: an analysis of data from the Global Burden of Diseases Study 2015. The Lancet 389, 1907–1918. https://doi.org/10.1016/S0140-6736(17)30505-6

Cooper, M.J., Martin, R.V., McLinden, C.A., Brook, J.R., 2020. Inferring ground-level nitrogen dioxide concentrations at fine spatial resolution applied to the TROPOMI satellite instrument. Environ. Res. Lett. 15, 104013. https://doi.org/10.1088/1748-9326/aba3a5

Daly, C., Halbleib, M., Smith, J.I., Gibson, W.P., Doggett, M.K., Taylor, G.H., Curtis, J., Pasteris, P.P., 2008. Physiographically sensitive mapping of climatological temperature and precipitation across the conterminous United States. Int. J. Climatol. 28, 2031–2064. https://doi.org/10.1002/joc.1688

de Foy, B., Brune, W.H., Schauer, J.J., 2020. Changes in ozone photochemical regime in Fresno, California from 1994 to 2018 deduced from changes in the weekend effect. Environmental Pollution 263, 114380. https://doi.org/10.1016/j.envpol.2020.114380

de Foy, B., Lu, Z., Streets, D.G., 2016. Impacts of control strategies, the Great Recession and weekday variations on NO2 columns above North American cities. Atmospheric Environment 138, 74–86. https://doi.org/10.1016/j.atmosenv.2016.04.038

de Foy, B., Lu, Z., Streets, D.G., Lamsal, L.N., Duncan, B.N., 2015. Estimates of power plant NOx emissions and lifetimes from OMI NO2 satellite retrievals. Atmospheric Environment 116, 1–11. https://doi.org/10.1016/j.atmosenv.2015.05.056

De Smedt, I., Theys, N., Yu, H., Danckaert, T., Lerot, C., Compernolle, S., Van Roozendael, M., Richter, A., Hilboll, A., Peters, E., Pedergnana, M., Loyola, D., Beirle, S., Wagner, T., Eskes, H., van Geffen, J., Boersma, K.F., Veefkind, P., 2018. Algorithm theoretical

baseline for formaldehyde retrievals from S5P TROPOMI and from the QA4ECV project. Atmos. Meas. Tech. 11, 2395–2426. https://doi.org/10.5194/amt-11-2395-2018

Deng, Y., Li, J., Li, Y., Wu, R., Xie, S., 2019. Characteristics of volatile organic compounds, NO2, and effects on ozone formation at a site with high ozone level in Chengdu. Journal of Environmental Sciences 75, 334–345. https://doi.org/10.1016/j.jes.2018.05.004

Du, X., Tang, W., Zhang, Z., Li, Y., Yu, Y., Xiao, Z., Meng, F., 2022. Sensitivity modeling of ozone and its precursors over the Chengdu metropolitan area. Atmospheric Environment 277, 119071. https://doi.org/10.1016/j.atmosenv.2022.119071

Duncan, B.N., Yoshida, Y., Olson, J.R., Sillman, S., Martin, R.V., Lamsal, L., Hu, Y., Pickering, K.E., Retscher, C., Allen, D.J., Crawford, J.H., 2010. Application of OMI observations to a space-based indicator of NOx and VOC controls on surface ozone formation. Atmospheric Environment 44, 2213–2223. https://doi.org/10.1016/j.atmosenv.2010.03.010

Friedl, Mark, Sulla-Menashe, Damien, 2019. MCD12Q1 MODIS/Terra+Aqua Land Cover Type Yearly L3 Global 500m SIN Grid V006. https://doi.org/10.5067/MODIS/MCD12Q1.006

Gao, H., Yang, W., Wang, J., Zheng, X., 2020. Analysis of the Effectiveness of Air Pollution Control Policies Based on Historical Evaluation and Deep Learning Forecast: A Case Study of Chengdu-Chongqing Region in China. Sustainability 13, 206. https://doi.org/10.3390/su13010206

Gao, W., Tie, X., Xu, J., Huang, R., Mao, X., Zhou, G., Chang, L., 2017. Long-term trend of O3 in a mega City (Shanghai), China: Characteristics, causes, and interactions with precursors. Science of The Total Environment 603–604, 425–433. https://doi.org/10.1016/j.scitotenv.2017.06.099

Geddes, J.A., Pusede, S.E., Wong, A.Y.H., 2022. Changes in the Relative Importance of Biogenic Isoprene and Soil NOx Emissions on Ozone Concentrations in Nonattainment Areas of the United States. JGR Atmospheres 127, e2021JD036361. https://doi.org/10.1029/2021JD036361

Goldberg, D.L., Anenberg, S.C., Kerr, G.H., Mohegh, A., Lu, Z., Streets, D.G., 2021. TROPOMI NO2 in the United States: A Detailed Look at the Annual Averages, Weekly Cycles,

Effects of Temperature, and Correlation With Surface NO2 Concentrations. Earth's Future 9. https://doi.org/10.1029/2020EF001665

Grell, G.A., Dévényi, D., 2002. A generalized approach to parameterizing convection combining ensemble and data assimilation techniques. Geophys. Res. Lett. 29, 38-1-38–4. https://doi.org/10.1029/2002GL015311

Gu, S., Guenther, A., Faiola, C., 2021. Effects of Anthropogenic and Biogenic Volatile Organic Compounds on Los Angeles Air Quality. Environ. Sci. Technol. 55, 12191–12201. https://doi.org/10.1021/acs.est.1c01481

Guenther, A.B., Jiang, X., Heald, C.L., Sakulyanontvittaya, T., Duhl, T., Emmons, L.K., Wang, X., 2012. The Model of Emissions of Gases and Aerosols from Nature version 2.1 (MEGAN2.1): an extended and updated framework for modeling biogenic emissions. Geosci. Model Dev. 5, 1471–1492. https://doi.org/10.5194/gmd-5-1471-2012

He, Z., Wang, X., Ling, Z., Zhao, J., Guo, H., Shao, M., Wang, Z., 2019. Contributions of different anthropogenic volatile organic compound sources to ozone formation at a receptor site in the Pearl River Delta region and its policy implications. Atmos. Chem. Phys. 19, 8801–8816. https://doi.org/10.5194/acp-19-8801-2019

Hersbach, H., Bell, B., Berrisford, P., Hirahara, S., Horányi, A., Muñoz-Sabater, J., Nicolas, J., Peubey, C., Radu, R., Schepers, D., Simmons, A., Soci, C., Abdalla, S., Abellan, X., Balsamo, G., Bechtold, P., Biavati, G., Bidlot, J., Bonavita, M., Chiara, G., Dahlgren, P., Dee, D., Diamantakis, M., Dragani, R., Flemming, J., Forbes, R., Fuentes, M., Geer, A., Haimberger, L., Healy, S., Hogan, R.J., Hólm, E., Janisková, M., Keeley, S., Laloyaux, P., Lopez, P., Lupu, C., Radnoti, G., Rosnay, P., Rozum, I., Vamborg, F., Villaume, S., Thépaut, J., 2020. The ERA5 global reanalysis. Q.J.R. Meteorol. Soc. 146, 1999–2049. https://doi.org/10.1002/qj.3803

Hong, S.-Y., Kim, S.-W., 2008. Stable Boundary Layer Mixing in a Vertical Diffusion Scheme 2.

Hong, S.-Y., Noh, Y., Dudhia, J., 2006. A New Vertical Diffusion Package with an Explicit Treatment of Entrainment Processes. Monthly Weather Review 134, 2318–2341. https://doi.org/10.1175/MWR3199.1

Horton, D.E., Harshvardhan, Diffenbaugh, N.S., 2012. Response of air stagnation frequency to anthropogenically enhanced radiative forcing. Environ. Res. Lett. 7, 044034. https://doi.org/10.1088/1748-9326/7/4/044034

Hu, X.-M., Nielsen-Gammon, J.W., Zhang, F., 2010. Evaluation of Three Planetary Boundary Layer Schemes in the WRF Model. Journal of Applied Meteorology and Climatology 49, 1831–1844. https://doi.org/10.1175/2010JAMC2432.1

Huang, X., Zhang, T., Jiang, X., Liu, S., Xiao, D., 2021. Interannual variability of mid-summer heat wave frequency over the Sichuan Basin. Int J Climatol 41, 5036–5050. https://doi.org/10.1002/joc.7115

Hudman, R.C., Moore, N.E., Mebust, A.K., Martin, R.V., Russell, A.R., Valin, L.C., Cohen, R.C., 2012. Steps towards a mechanistic model of global soil nitric oxide emissions: implementation and space based-constraints. Atmos. Chem. Phys. 12, 7779–7795. https://doi.org/10.5194/acp-12-7779-2012

Janjić, Z.I., 2002. Nonsingular Implementation of the Mellor-Yamada Level 2.5 Scheme in the NCEP Meso model 61.

Jiang, Z., McDonald, B.C., Worden, H., Worden, J.R., Miyazaki, K., Qu, Z., Henze, D.K., Jones, D.B.A., Arellano, A.F., Fischer, E.V., Zhu, L., Boersma, K.F., 2018. Unexpected slowdown of US pollutant emission reduction in the past decade. Proc. Natl. Acad. Sci. U.S.A. 115, 5099–5104. https://doi.org/10.1073/pnas.1801191115

Jiménez, P.A., Dudhia, J., 2012. Improving the Representation of Resolved and Unresolved Topographic Effects on Surface Wind in the WRF Model. Journal of Applied Meteorology and Climatology 51, 300–316. https://doi.org/10.1175/JAMC-D-11-084.1

Jin, X., Fiore, A., Boersma, K.F., Smedt, I.D., Valin, L., 2020. Inferring Changes in Summertime Surface Ozone–NOx–VOC Chemistry over U.S. Urban Areas from Two Decades of Satellite and Ground-Based Observations. Environ. Sci. Technol. 54, 6518–6529. https://doi.org/10.1021/acs.est.9b07785

Jin, X., Holloway, T., 2015. Spatial and temporal variability of ozone sensitivity over China observed from the Ozone Monitoring Instrument. J. Geophys. Res. Atmos. 120, 7229–7246. https://doi.org/10.1002/2015JD023250

Krotkov, Nickolay A., Veefkind, Pepijn, 2012. OMI/Aura Nitrogen Dioxide (NO2) Total and Tropospheric Column 1-orbit L2 Swath 13x24 km. https://doi.org/10.5067/AURA/OMI/DATA2017

Lamsal, L.N., Duncan, B.N., Yoshida, Y., Krotkov, N.A., Pickering, K.E., Streets, D.G., Lu, Z., 2015. U.S. NO2 trends (2005–2013): EPA Air Quality System (AQS) data versus improved observations from the Ozone Monitoring Instrument (OMI). Atmospheric Environment 110, 130–143. https://doi.org/10.1016/j.atmosenv.2015.03.055

Laughner, J.L., Cohen, R.C., 2019. Direct observation of changing NOx lifetime in North American cities. Science 366, 723–727. https://doi.org/10.1126/science.aax6832

Levelt, P.F., Hilsenrath, E., Leppelmeier, G.W., van den Oord, G.H.J., Bhartia, P.K., Tamminen, J., de Haan, J.F., Veefkind, J.P., 2006. Science objectives of the ozone monitoring instrument. IEEE Trans. Geosci. Remote Sensing 44, 1199–1208. https://doi.org/10.1109/TGRS.2006.872336

Levelt, P.F., Joiner, J., Tamminen, J., Veefkind, J.P., Bhartia, P.K., Stein Zweers, D.C., Duncan, B.N., Streets, D.G., Eskes, H., van der A, R., McLinden, C., Fioletov, V., Carn, S., de Laat, J., DeLand, M., Marchenko, S., McPeters, R., Ziemke, J., Fu, D., Liu, X., Pickering, K., Apituley, A., González Abad, G., Arola, A., Boersma, F., Chan Miller, C., Chance, K., de Graaf, M., Hakkarainen, J., Hassinen, S., Ialongo, I., Kleipool, Q., Krotkov, N., Li, C., Lamsal, L., Newman, P., Nowlan, C., Suleiman, R., Tilstra, L.G., Torres, O., Wang, H., Wargan, K., 2018. The Ozone Monitoring Instrument: overview of 14 years in space. Atmos. Chem. Phys. 18, 5699–5745. https://doi.org/10.5194/acp-18-5699-2018

Li, S., Banerjee, T., 2021. Spatial and temporal pattern of wildfires in California from 2000 to 2019. Sci Rep 11, 8779. https://doi.org/10.1038/s41598-021-88131-9

Lin, Y.-L., Farley, R.D., Orville, H.D., 1983. Bulk Parameterization of the Snow Field in a Cloud Model. Journal of Applied Meteorology and Climatology 22, 1065–1092. https://doi.org/10.1175/1520-0450(1983)022<1065:BPOTSF>2.0.CO;2

Liu, H., Liu, S., Xue, B., Lv, Z., Meng, Z., Yang, X., Xue, T., Yu, Q., He, K., 2018. Ground-level ozone pollution and its health impacts in China. Atmospheric Environment 173, 223–230. https://doi.org/10.1016/j.atmosenv.2017.11.014

Liu, J., Wang, L., Li, M., Liao, Z., Sun, Y., Song, T., Gao, W., Wang, Yonghong, Li, Y., Ji, D., Hu, B., Kerminen, V.-M., Wang, Yuesi, Kulmala, M., 2019. Quantifying the impact of

synoptic circulation patterns on ozone variability in northern China from April to October 2013–2017. Atmos. Chem. Phys. 19, 14477–14492. https://doi.org/10.5194/acp-19-14477-2019

Liu, Y., Wang, T., 2020a. Worsening urban ozone pollution in China from 2013 to 2017 – Part 1: The complex and varying roles of meteorology. Atmos. Chem. Phys. 20, 6305–6321. https://doi.org/10.5194/acp-20-6305-2020

Liu, Y., Wang, T., 2020b. Worsening urban ozone pollution in China from 2013 to 2017 – Part 2: The effects of emission changes and implications for multi-pollutant control. Atmos. Chem. Phys. 20, 6323–6337. https://doi.org/10.5194/acp-20-6323-2020

Lu, Z., Streets, D.G., de Foy, B., Lamsal, L.N., Duncan, B.N., Xing, J., 2015. Emissions of nitrogen oxides from US urban areas: estimation from Ozone Monitoring Instrument retrievals for 2005–2014. Atmos. Chem. Phys. 15, 10367–10383. https://doi.org/10.5194/acp-15-10367-2015

Lyu, X., Wang, N., Guo, H., Xue, L., Jiang, F., Zeren, Y., Cheng, H., Cai, Z., Han, L., Zhou, Y., 2019. Causes of a continuous summertime O3 pollution event in Jinan, a central city in the North China Plain. Atmos. Chem. Phys. 19, 3025–3042. https://doi.org/10.5194/acp-19-3025-2019

Ma, M., Gao, Y., Ding, A., Su, H., Liao, H., Wang, S., Wang, X., Zhao, B., Zhang, S., Fu, P., Guenther, A.B., Wang, M., Li, S., Chu, B., Yao, X., Gao, H., 2022. Development and Assessment of a High-Resolution Biogenic Emission Inventory from Urban Green Spaces in China. Environ. Sci. Technol. 56, 175–184. https://doi.org/10.1021/acs.est.1c06170

Mebust, A.K., Russell, A.R., Hudman, R.C., Valin, L.C., Cohen, R.C., 2011. Characterization of wildfire NOx emissions using MODIS fire radiative power and OMI tropospheric NO2 columns. Atmos. Chem. Phys. 11, 5839–5851. https://doi.org/10.5194/acp-11-5839-2011

Meng, X., Pang, K., Yin, Z., Xiang, X., 2021. Grid-based spatiotemporal modeling of ambient ozone to assess human exposure using environmental big data. Atmospheric Pollution Research 12, 101216. https://doi.org/10.1016/j.apr.2021.101216

Meng, Y.-Y., Rull, R.P., Wilhelm, M., Lombardi, C., Balmes, J., Ritz, B., 2010. Outdoor air pollution and uncontrolled asthma in the San Joaquin Valley, California. J Epidemiol Community Health 64, 142. https://doi.org/10.1136/jech.2009.083576

Mesinger, F., DiMego, G., Kalnay, E., Mitchell, K., Shafran, P.C., Ebisuzaki, W., Jović, D., Woollen, J., Rogers, E., Berbery, E.H., Ek, M.B., Fan, Y., Grumbine, R., Higgins, W., Li, H., Lin, Y., Manikin, G., Parrish, D., Shi, W., 2004. North American Regional Reanalysis. Bull. Amer. Meteor. Soc. 87, 343–360. https://doi.org/10.1175/BAMS-87-3-343

Mlawer, E.J., Taubman, S.J., Brown, P.D., Iacono, M.J., Clough, S.A., 1997. Radiative transfer for inhomogeneous atmospheres: RRTM, a validated correlated-k model for the longwave. J. Geophys. Res. 102, 16663–16682. https://doi.org/10.1029/97JD00237

Muñoz-Sabater, J., Dutra, E., Agustí-Panareda, A., Albergel, C., Arduini, G., Balsamo, G., Boussetta, S., Choulga, M., Harrigan, S., Hersbach, H., Martens, B., Miralles, D.G., Piles, M., Rodríguez-Fernández, N.J., Zsoter, E., Buontempo, C., Thépaut, J.-N., 2021. ERA5-Land: a state-of-the-art global reanalysis dataset for land applications. Earth Syst. Sci. Data 13, 4349–4383. https://doi.org/10.5194/essd-13-4349-2021

Ninneman, M., Jaffe, D.A., 2021. The impact of wildfire smoke on ozone production in an urban area: Insights from field observations and photochemical box modeling. Atmospheric Environment 267, 118764. https://doi.org/10.1016/j.atmosenv.2021.118764

Noh, Y., Cheon, W.G., Hong, S.Y., Raasch, S., 2003. Improvement of the K-profile Model for the Planetary Boundary Layer based on Large Eddy Simulation Data. Boundary-Layer Meteorology 107, 401–427. https://doi.org/10.1023/A:1022146015946

Oikawa, P.Y., Ge, C., Wang, J., Eberwein, J.R., Liang, L.L., Allsman, L.A., Grantz, D.A., Jenerette, G.D., 2015. Unusually high soil nitrogen oxide emissions influence air quality in a high-temperature agricultural region. Nat Commun 6, 8753. https://doi.org/10.1038/ncomms9753

Orru, H., Andersson, C., Ebi, K.L., Langner, J., Åström, C., Forsberg, B., 2013. Impact of climate change on ozone-related mortality and morbidity in Europe. Eur Respir J 41, 285–294. https://doi.org/10.1183/09031936.00210411

Pan, K., Faloona, I.C., 2022. The impacts of wildfires on ozone production and boundary layer dynamics in California's Central Valley. Atmos. Chem. Phys. 22, 9681–9702. https://doi.org/10.5194/acp-22-9681-2022

Parrish, D.D., Faloona, I.C., Derwent, R.G., 2022. Observational-based assessment of contributions to maximum ozone concentrations in the western United States. Journal of

the Air & Waste Management Association 72, 434–454. https://doi.org/10.1080/10962247.2022.2050962

Parrish, D.D., Young, L.M., Newman, M.H., Aikin, K.C., Ryerson, T.B., 2017. Ozone Design Values in Southern California's Air Basins: Temporal Evolution and U.S. Background Contribution. J. Geophys. Res. Atmos. 122, 11,166-11,182. https://doi.org/10.1002/2016JD026329

Peirce, J.J., Aneja, V.P., 2000. Nitric Oxide Emissions from Engineered Soil Systems. J. Environ. Eng. 126, 225–232. https://doi.org/10.1061/(ASCE)0733-9372(2000)126:3(225)

Pilegaard, K., 2013. Processes regulating nitric oxide emissions from soils. Phil. Trans. R. Soc. B 368, 20130126. https://doi.org/10.1098/rstb.2013.0126

Pleim, J.E., 2007. A Combined Local and Nonlocal Closure Model for the Atmospheric Boundary Layer. Part I: Model Description and Testing. Journal of Applied Meteorology and Climatology 46, 1383–1395. https://doi.org/10.1175/JAM2539.1

Pleim, J.E., Chang, J.S., 1992. A non-local closure model for vertical mixing in the convective boundary layer. Atmospheric Environment. Part A. General Topics 26, 965–981. https://doi.org/10.1016/0960-1686(92)90028-J

Qian, T., Zhao, P., Zhang, F., Bao, X., 2015. Rainy-Season Precipitation over the Sichuan Basin and Adjacent Regions in Southwestern China. Monthly Weather Review 143, 383–394. https://doi.org/10.1175/MWR-D-13-00158.1

Qu, Z., Jacob, D.J., Silvern, R.F., Shah, V., Campbell, P.C., Valin, L.C., Murray, L.T., 2021. US COVID-19 Shutdown Demonstrates Importance of Background NO2 in Inferring NOx Emissions From Satellite NO2 Observations. Geophysical Research Letters 48, e2021GL092783. https://doi.org/10.1029/2021GL092783

Russell, A.R., Perring, A.E., Valin, L.C., Bucsela, E.J., Browne, E.C., Wooldridge, P.J., Cohen, R.C., 2011. A high spatial resolution retrieval of NO2 column densities from OMI: method and evaluation. Atmos. Chem. Phys. 11, 8543–8554. https://doi.org/10.5194/acp-11-8543-2011

Russell, A.R., Valin, L.C., Bucsela, E.J., Wenig, M.O., Cohen, R.C., 2010. Space-based Constraints on Spatial and Temporal Patterns of NOx Emissions in California, 2005-2008. Environ. Sci. Technol. 44, 3608–3615. https://doi.org/10.1021/es903451j

Russell, A.R., Valin, L.C., Cohen, R.C., 2012. Trends in OMI NO2 observations over the United States: effects of emission control technology and the economic recession. Atmos. Chem. Phys. 12, 12197–12209. https://doi.org/10.5194/acp-12-12197-2012

Sampedro, J., Waldhoff, S.T., Van de Ven, D.-J., Pardo, G., Van Dingenen, R., Arto, I., del Prado, A., Sanz, M.J., 2020. Future impacts of ozone driven damages on agricultural systems. Atmospheric Environment 231, 117538. https://doi.org/10.1016/j.atmosenv.2020.117538

Schenkeveld, V.M.E., Jaross, G., Marchenko, S., Haffner, D., Kleipool, Q.L., Rozemeijer, N.C., Veefkind, J.P., Levelt, P.F., 2017. In-flight performance of the Ozone Monitoring Instrument. Atmos. Meas. Tech. 10, 1957–1986. https://doi.org/10.5194/amt-10-1957-2017

Schumann, U., Huntrieser, H., 2007. The global lightning-induced nitrogen oxides source. Atmos. Chem. Phys.

Sha, T., Ma, X., Zhang, H., Janechek, N., Wang, Yanyu, Wang, Yi, Castro García, L., Jenerette, G.D., Wang, J., 2021. Impacts of Soil NOx Emission on O3 Air Quality in Rural California. Environ. Sci. Technol. 55, 7113–7122. https://doi.org/10.1021/acs.est.0c06834

Shah, V., Jacob, D.J., Li, K., Silvern, R.F., Zhai, S., Liu, M., Lin, J., Zhang, Q., 2020. Effect of changing NOx lifetime on the seasonality and long-term trends of satellite-observed tropospheric NO2 columns over China. Atmos. Chem. Phys. 20, 1483–1495. https://doi.org/10.5194/acp-20-1483-2020

Shen, H., Sun, Z., Chen, Y., Russell, A.G., Hu, Y., Odman, M.T., Qian, Y., Archibald, A.T., Tao, S., 2021. Novel Method for Ozone Isopleth Construction and Diagnosis for the Ozone Control Strategy of Chinese Cities. Environ. Sci. Technol. acs.est.1c01567. https://doi.org/10.1021/acs.est.1c01567

Shen, L., Jacob, D.J., Zhu, L., Zhang, Q., Zheng, B., Sulprizio, M.P., Li, K., De Smedt, I., González Abad, G., Cao, H., Fu, T., Liao, H., 2019. The 2005–2016 Trends of Formaldehyde Columns Over China Observed by Satellites: Increasing Anthropogenic Emissions of Volatile Organic Compounds and Decreasing Agricultural Fire Emissions. Geophys. Res. Lett. 46, 4468–4475. https://doi.org/10.1029/2019GL082172

Silvern, R.F., Jacob, D.J., Mickley, L.J., Sulprizio, M.P., Travis, K.R., Marais, E.A., Cohen, R.C., Laughner, J.L., Choi, S., Joiner, J., Lamsal, L.N., 2019. Using satellite observations of tropospheric NO2 columns to infer long-term trends in US NOx emissions: the importance of accounting for the free tropospheric NO2 background. Atmos. Chem. Phys. 19, 8863–8878. https://doi.org/10.5194/acp-19-8863-2019

Steinkamp, J., Lawrence, M.G., 2011. Improvement and evaluation of simulated global biogenic soil NO emissions in an AC-GCM. Atmos. Chem. Phys. 11, 6063–6082. https://doi.org/10.5194/acp-11-6063-2011

Stowell, J.D., Kim, Y., Gao, Y., Fu, J.S., Chang, H.H., Liu, Y., 2017. The impact of climate change and emissions control on future ozone levels: Implications for human health. Environment International 108, 41–50. https://doi.org/10.1016/j.envint.2017.08.001

Sun, K., Zhu, L., Cady-Pereira, K., Chan Miller, C., Chance, K., Clarisse, L., Coheur, P.-F., González Abad, G., Huang, G., Liu, X., Van Damme, M., Yang, K., Zondlo, M., 2018. A physics-based approach to oversample multi-satellite, multispecies observations to a common grid. Atmos. Meas. Tech. 11, 6679–6701. https://doi.org/10.5194/amt-11-6679-2018

Sun, Y., Yin, H., Lu, X., Notholt, J., Palm, M., Liu, C., Tian, Y., Zheng, B., 2021. The drivers and health risks of unexpected surface ozone enhancements over the Sichuan Basin, China, in 2020. Atmos. Chem. Phys. 21, 18589–18608. https://doi.org/10.5194/acp-21-18589-2021

Tan, Q., Zhou, L., Liu, H., Feng, M., Qiu, Y., Yang, F., Jiang, W., Wei, F., 2020. Observation-Based Summer O3 Control Effect Evaluation: A Case Study in Chengdu, a Megacity in Sichuan Basin, China. Atmosphere 11, 1278. https://doi.org/10.3390/atmos11121278

Tan, Y., Henderick, P., Yoon, S., Herner, J., Montes, T., Boriboonsomsin, K., Johnson, K., Scora, G., Sandez, D., Durbin, T.D., 2019. On-Board Sensor-Based NOx Emissions from Heavy-Duty Diesel Vehicles. Environ. Sci. Technol. 53, 5504–5511. https://doi.org/10.1021/acs.est.8b07048

Tan, Z., Lu, K., Jiang, M., Su, R., Dong, H., Zeng, L., Xie, S., Tan, Q., Zhang, Y., 2018. Exploring ozone pollution in Chengdu, southwestern China: A case study from radical chemistry to O3-VOC-NOx sensitivity. Science of The Total Environment 636, 775–786. https://doi.org/10.1016/j.scitotenv.2018.04.286

Tong, D.Q., Lamsal, L., Pan, L., Ding, C., Kim, H., Lee, P., Chai, T., Pickering, K.E., Stajner, I., 2015. Long-term NOx trends over large cities in the United States during the great recession: Comparison of satellite retrievals, ground observations, and emission inventories. Atmospheric Environment 107, 70–84. https://doi.org/10.1016/j.atmosenv.2015.01.035

Trainer, M., Parrish, D.D., Goldan, P.D., Roberts, J., Fehsenfeld, F.C., 2000. Review of observation-based analysis of the regional factors influencing ozone concentrations. Atmospheric Environment 17.

US EPA, O., 2016. Nitrogen Dioxide (NO2) Primary Air Quality Standards [WWW Document]. URL https://www.epa.gov/naaqs/nitrogen-dioxide-no2-primary-air-quality-standards (accessed 2.12.23).

van Dijk, S.M., 2002. Biogenic NO emissions from forest and pasture soils: Relating laboratory studies to field measurements. J. Geophys. Res. 107, 8058. https://doi.org/10.1029/2001JD000358

van Geffen, J., Boersma, K.F., Eskes, H., Sneep, M., ter Linden, M., Zara, M., Veefkind, J.P., 2020. S5P TROPOMI NO2 slant column retrieval: method, stability, uncertainties and comparisons with OMI. Atmos. Meas. Tech. 13, 1315–1335. https://doi.org/10.5194/amt-13-1315-2020

van Geffen, J.H.G.M., Eskes, H.J., Boersma, K.F., Maasakkers, J.D., Veefkind, J.P., 2019. TROPOMI ATBD of the total and tropospheric NO2 data products. Royal Netherlands Meteorological Institute.

Vandaele, A.C., Hermans, C., Simon, P.C., Carleer, M., Colin, R., Fally, S., Mérienne, M.F., Jenouvrier, A., Coquart, B., 1998. Measurements of the NO2 absorption cross-section from 42 000 cm−1 to 10 000 cm−1 (238–1000 nm) at 220 K and 294 K. Journal of Quantitative Spectroscopy and Radiative Transfer 59, 171–184. https://doi.org/10.1016/S0022-4073(97)00168-4

Veefkind, J.P., Aben, I., McMullan, K., Förster, H., de Vries, J., Otter, G., Claas, J., Eskes, H.J., de Haan, J.F., Kleipool, Q., van Weele, M., Hasekamp, O., Hoogeveen, R., Landgraf, J., Snel, R., Tol, P., Ingmann, P., Voors, R., Kruizinga, B., Vink, R., Visser, H., Levelt, P.F., 2012. TROPOMI on the ESA Sentinel-5 Precursor: A GMES mission for global observations of the atmospheric composition for climate, air quality and ozone layer

applications. Remote Sensing of Environment 120, 70–83. https://doi.org/10.1016/j.rse.2011.09.027

Vinken, G.C.M., Boersma, K.F., Maasakkers, J.D., Adon, M., Martin, R.V., 2014. Worldwide biogenic soil NOx emissions inferred from OMI NO2 observations. Atmos. Chem. Phys. 14, 10363–10381. https://doi.org/10.5194/acp-14-10363-2014

Wang, H., Wu, K., Liu, Y., Sheng, B., Lu, X., He, Y., Xie, J., Wang, Haichao, Fan, S., 2021. Role of Heat Wave-Induced Biogenic VOC Enhancements in Persistent Ozone Episodes Formation in Pearl River Delta. Geophys Res Atmos 126. https://doi.org/10.1029/2020JD034317

Wang, L., Li, M., Wang, Q., Li, Y., Xin, J., Tang, X., Du, W., Song, T., Li, T., Sun, Y., Gao, W., Hu, B., Wang, Y., 2022. Air stagnation in China: Spatiotemporal variability and differing impact on PM2.5 and O3 during 2013–2018. Science of The Total Environment 819, 152778. https://doi.org/10.1016/j.scitotenv.2021.152778

Wang, Y., Ge, C., Castro Garcia, L., Jenerette, G.D., Oikawa, P.Y., Wang, J., 2021. Improved modelling of soil NOx emissions in a high temperature agricultural region: role of background emissions on NO2 trend over the US. Environ. Res. Lett. 16, 084061. https://doi.org/10.1088/1748-9326/ac16a3

Wang, Y., Wild, O., Chen, X., Wu, Q., Gao, M., Chen, H., Qi, Y., Wang, Z., 2020. Health impacts of long-term ozone exposure in China over 2013–2017. Environment International 144, 106030. https://doi.org/10.1016/j.envint.2020.106030

Westervelt, D.M., Ma, C.T., He, M.Z., Fiore, A.M., Kinney, P.L., Kioumourtzoglou, M.-A., Wang, S., Xing, J., Ding, D., Correa, G., 2019. Mid-21st century ozone air quality and health burden in China under emissions scenarios and climate change. Environ. Res. Lett. 14, 074030. https://doi.org/10.1088/1748-9326/ab260b

Williams, A.P., Abatzoglou, J.T., Gershunov, A., Guzman-Morales, J., Bishop, D.A., Balch, J.K., Lettenmaier, D.P., 2019. Observed Impacts of Anthropogenic Climate Change on Wildfire in California. Earth's Future 7, 892–910. https://doi.org/10.1029/2019EF001210

Wu, K., Kang, P., Wang, Z., Gu, S., Tie, X., Zhang, Y., Wen, X., Wang, S., Chen, Y., Wang, Y., Chen, D., 2017. Ozone temporal variation and its meteorological factors over Chengdu City. Acta Scientiae Circumstantiae 37, 4241–4252.

Wu, K., Wang, Y., Qiao, Y., Liu, Y., Wang, S., Yang, X., Wang, H., Lu, Y., Zhang, X., Lei, Y., 2022. Drivers of 2013–2020 ozone trends in the Sichuan Basin, China: Impacts of meteorology and precursor emission changes. Environmental Pollution 300, 118914. https://doi.org/10.1016/j.envpol.2022.118914

Wu, K., Yang, X., Chen, D., Gu, S., Lu, Y., Jiang, Q., Wang, K., Ou, Y., Qian, Y., Shao, P., Lu, S., 2020. Estimation of biogenic VOC emissions and their corresponding impact on ozone and secondary organic aerosol formation in China. Atmospheric Research 231, 104656. https://doi.org/10.1016/j.atmosres.2019.104656

Xie, M., Zhan, C., Zhan, Y., Shi, J., Luo, Y., Zhang, M., Liu, Q., Shen, F., 2021. Spatiotemporal Variability of Air Stagnation and its Relation to Summertime Ozone in the Yangtze River Delta of China. Front. Environ. Sci. 9, 783524. https://doi.org/10.3389/fenvs.2021.783524

Xie, M., Zhu, K., Wang, T., Yang, H., Zhuang, B., Li, S., Li, M., Zhu, X., Ouyang, Y., 2014. Application of photochemical indicators to evaluate ozone nonlinear chemistry and pollution control countermeasure in China. Atmospheric Environment 99, 466–473. https://doi.org/10.1016/j.atmosenv.2014.10.013

Yang, J., Shao, M., 2021. Impacts of Extreme Air Pollution Meteorology on Air Quality in China. Geophys Res Atmos 126. https://doi.org/10.1029/2020JD033210

Yang, X., Lu, Y., Wang, Y., Qiao, Y., Zhang, G., Wang, S., Zhang, X., Liu, Z., Liu, Y., Zhu, X., 2021a. Impact of synoptic patterns on regional ozone pollution in Sichuan Basin. China Environmental Science 41, 2526~2539.

Yang, X., Wu, K., Lu, Y., Wang, S., Qiao, Y., Zhang, X., Wang, Y., Wang, H., Liu, Z., Liu, Y., Lei, Y., 2021b. Origin of regional springtime ozone episodes in the Sichuan Basin, China: Role of synoptic forcing and regional transport. Environmental Pollution 278, 116845. https://doi.org/10.1016/j.envpol.2021.116845

Yang, X., Wu, K., Wang, H., Liu, Y., Gu, S., Lu, Y., Zhang, X., Hu, Y., Ou, Y., Wang, S., Wang, Z., 2020. Summertime ozone pollution in Sichuan Basin, China: Meteorological conditions, sources and process analysis. Atmospheric Environment 226, 117392. https://doi.org/10.1016/j.atmosenv.2020.117392

Yienger, J.J., Levy, H., 1995. Empirical model of global soil-biogenic NOx emission. J. Geophys. Res. 100, 11447. https://doi.org/10.1029/95JD00370

Zhan, C., Xie, M., 2022. Land use and anthropogenic heat modulate ozone by meteorology: a perspective from the Yangtze River Delta region. Atmospheric Chemistry and Physics 22, 1351–1371. https://doi.org/10.5194/acp-22-1351-2022

Zhao, K., Bao, Y., Huang, J., Wu, Y., Moshary, F., Arend, M., Wang, Y., Lee, X., 2019. A high-resolution modeling study of a heat wave-driven ozone exceedance event in New York City and surrounding regions. Atmospheric Environment 199, 368–379. https://doi.org/10.1016/j.atmosenv.2018.10.059

Zheng, B., Tong, D., Li, M., Liu, F., Hong, C., Geng, G., Li, H., Li, X., Peng, L., Qi, J., Yan, L., Zhang, Y., Zhao, H., Zheng, Y., He, K., Zhang, Q., 2018. Trends in China's anthropogenic emissions since 2010 as the consequence of clean air actions. Atmos. Chem. Phys. 18, 14095–14111. https://doi.org/10.5194/acp-18-14095-2018

Zheng, B., Zhang, Q., Geng, G., Chen, C., Shi, Q., Cui, M., Lei, Y., He, K., 2021. Changes in China's anthropogenic emissions and air quality during the COVID-19 pandemic in 2020. Earth Syst. Sci. Data 13, 2895–2907. https://doi.org/10.5194/essd-13-2895-2021

Zhou, Z., Tan, Q., Deng, Y., Wu, K., Yang, X., Zhou, X., 2019. Emission inventory of anthropogenic air pollutant sources and characteristics of VOCs species in Sichuan Province, China. Journal of Atmospheric Chemistry 76, 21–58. https://doi.org/10.1007/s10874-019-9386-7

Zhu, L., Mickley, L.J., Jacob, D.J., Marais, E.A., Sheng, J., Hu, L., Abad, G.G., Chance, K., 2017. Long-term (2005-2014) trends in formaldehyde (HCHO) columns across North America as seen by the OMI satellite instrument: Evidence of changing emissions of volatile organic compounds: HCHO Trend Across North America. Geophys. Res. Lett. 44, 7079–7086. https://doi.org/10.1002/2017GL073859

Zoogman, P., Liu, X., Suleiman, R.M., Pennington, W.F., Flittner, D.E., Al-Saadi, J.A., Hilton, B.B., Nicks, D.K., Newchurch, M.J., Carr, J.L., Janz, S.J., Andraschko, M.R., Arola, A., Baker, B.D., Canova, B.P., Chan Miller, C., Cohen, R.C., Davis, J.E., Dussault, M.E., Edwards, D.P., Fishman, J., Ghulam, A., González Abad, G., Grutter, M., Herman, J.R., Houck, J., Jacob, D.J., Joiner, J., Kerridge, B.J., Kim, J., Krotkov, N.A., Lamsal, L., Li, C., Lindfors, A., Martin, R.V., McElroy, C.T., McLinden, C., Natraj, V., Neil, D.O., Nowlan, C.R., O′Sullivan, E.J., Palmer, P.I., Pierce, R.B., Pippin, M.R., Saiz-Lopez, A., Spurr, R.J.D., Szykman, J.J., Torres, O., Veefkind, J.P., Veihelmann, B., Wang, H.,

Wang, J., Chance, K., 2017. Tropospheric emissions: Monitoring of pollution (TEMPO). Journal of Quantitative Spectroscopy and Radiative Transfer 186, 17–39. https://doi.org/10.1016/j.jqsrt.2016.05.008

Han, L., Chen, J., Jiang, T., et al., 2020. Sensitivity analysis of atmospheric ozone formation to its precursors in Chengdu with an observation based model [J]. Acta Sci. Circumst. 40 (11), 4092–4104.